SCHOOL OF PHYSICAL SCIENCES

MULTIPLE ATTENUATION VIA WAVEFIELD TRANSFORMATIONS

MATTHEW GORDON LAMONT

This thesis is presented as part of the requirements for the award of the

Degree of Doctor of Philosophy of the Curtin University of Technology

December 1998

X

"Multiples provide one of the most fascinating and frustrating

problem areas in geophysical exploration."

(Taner, 1980)

Dedication

To my wife Sheila and son Daniel Albert

Abstract

Seismic multiples are a serious hindrance to hydrocarbon exploration in Australia. In particular, water bottom multiples can be very difficult to attenuate. This is because there often exists a strongly reflective sea floor which gives multiples large amplitudes when compared with the primary events they overlay, and secondly, because of a widely occurring velocity inversion, which seriously reduces the effectiveness of a very important class of multiple attenuation techniques.

Multiple attenuation techniques can be classified according to the characteristic of the data which is used to discriminate against the multiples in conjunction with the operation behind the demultiple process. Common multiple attenuation processes include FK demultiple, Radon Demultiple, predictive deconvolution, wave equation based demultiple procedures and the family of techniques which come under the umbrella of Surface Multiple Attenuation (SMA). All of these techniques, given the right conditions, can be very effective. They also vary in price from very cheap (FK demultiple) through to expensive (wave equation based demultiple procedures).

However, despite these procedures, and fifty odd years of research, there is no effective general solution to multiple problems off the coast of Western Australia and indeed in many regions around the world.

Two new wavefield transformations, Multiple MoveOut (MMO) and IsoStretch Radial Trace (ISR), have been developed in this research to precondition data prior to the removal of surface related multiples by existing techniques. These form the basis of a new multiple attenuating procedure.

MMO shifts the data so that the water bottom primary event is flattened and the simple water bottom multiples are also flat and periodic. Water bottom peg leg multiples are made approximately periodic.

To solve the stretch problem introduced by the MMO transform, ISR interpolates oblique traces of constant stretch, which also map constant shot emergence angles. The water bottom primary and multiple events form a stationary time series after MMO and ISR. They are then amenable to removal by autoconvolution and predictive deconvolution.

The results of the new procedure are demonstrated on two case studies from offshore Western Australia. It is shown to be more effective at removing both simple and peg leg water bottom multiples than traditional techniques. Finally, it is an inexpensive procedure, which does not require velocity analysis prior to its application.

Acknowledgements

I would firstly like to thank Norm Uren for his guidance, accessibility, tolerance, friendship and encouragement throughout this research. I am also very indebted to Bruce Hartley for his technical assistance and comradeship.

I am also grateful for the financial assistance of the Australian Petroleum Cooperative Research Centre (APCRC) and to Woodside Offshore Petroleum for allowing me to use their facilities for this research. I would also like to acknowledge the financial support of the Australian Petroleum Production and Exploration Association (APPEA) through the K. A. Richards Scholarship.

Finally, this research would not have been completed without the support of my family.

Table of Contents

Table of Figures

Table of tables

Foreword

The quality of life in Australia is dependent on hydrocarbons in many ways. Broad-acre farming and mineral production produce the vast bulk of our exports. Both of these activities rely heavily on hydrocarbons. Australia's vast distances and sparse population underline our obsession with the car and our reliance on the transport industry. The defence of the nation is extremely reliant on hydrocarbons, as has been shown in the past when the outcomes of wars have been heavily influenced by the availability of hydrocarbons (Yergin, 1996).

In 1995/1996 the total hydrocarbon production in Australia is estimated to have been 4495 petajoules, valued at 2.1×10^{10} Australian dollars. Domestic production of hydrocarbons is essential to the Australian economy. In order to meet expected future production demands in Australia, 840 million dollars was spent on exploration during the 1996/1997 financial year.

It is therefore obvious that even a small percentage improvement in exploration success would lead to an enormous saving. This has been the driver in the strong focus on hydrocarbon related research in Australia.

The Australian Petroleum Cooperative Research Centre (APCRC) is a joint Commonwealth Government/Industry/University initiative. In essence, it is a mechanism for directing and funding research across a number of Australian Universities and the Commonwealth Scientific Investigation Research Organisation (CSIRO) in many petroleum related disciples, with the aim of enhancing hydrocarbon exploration and production in Australia. The research presented in this thesis has been sponsored by the APCRC.

The priorities of the APCRC are set by a Technical Directions Committee. This committee is comprised of representatives of the major oil companies in Australia, and a representative from the Australian Petroleum Production and Exploration Association (APPEA). The first research priority of the APCRC is multiple attenuation.

In offshore areas where there is a hard sea floor, reverberations of seismic waves within the water layer obscure the recording of weaker reflections from deeper key geological boundaries. These reverberations are known as multiples. The efficiency of Australian exploration would be greatly improved if more effective ways could be found to attenuate these multiples, and enhance the image of deeper, weaker events.

It is therefore for sound economic reasons that the oil industry rates the existence of seismic multiples as its greatest impediment to the discovery and production of hydrocarbon reserves. These are the hydrocarbon reserves which will underpin the nation's security and prosperity into the 21st Century.

Chapter 1
Introduction

The main tool of hydrocarbon explorationists, is the seismic reflection technique. A seismic reflection survey consists of creating seismic waves with artificial sources and observing the arrival time of the waves reflected from acoustic impedance contrasts (Sheriff, 1991).

Due to its status as the principal tool in hydrocarbon exploration, the quality of seismic data has a profound influence on exploration success. The information deduced from seismic data includes:

- position and geometry of possible hydrocarbon bearing structures,
- sedimentary basin structure,
- lithologies,
- tectonic activity over time,
- fluid migration pathways,
- rock fluid fills.

Ultimately this information is used to propose drilling targets. Drilling a hydrocarbon exploration well is very expensive (between 5 and 50 million dollars), and so it is important to maximise information and the value of survey data.

Ideally the seismic data would contain primary reflections only, with the amplitudes of events reflecting rock properties. Unfortunately, along with the primary

information, a multitude of reverberations is recorded between all reflectors. These echoes, reverberations or multiples, as they are called, are recorded at the same time as the primary reflection signals.

Troublesome multiples are often reflected from strong seismic reflectors. These reflectors can not only result in high amplitude multiples but also reduce the energy propagating deeper into the earth to illuminate more significant reflectors.

There are two ways to view seismic multiples. The first is to view them as seismic noise. Embree et al. (1963) defined noise as undesired seismic energy. The second is to view them as redundant information about the geology (Berkhout, 1987). In this thesis multiples are defined as noise and are treated in that context.

Seismic noise can be classified into two broad categories (Mayne, 1967); systematic (coherent) noise and random noise. Coherent noise is any unwanted phenomenon, which consistently exhibits characteristics that can be recognised and defined. Random noise is either unique to the position in space or time, or cannot be identified. Coherent noise therefore includes phenomena such as ground roll, cable jerk and multiple reflections.

Multiple reflections can be classified into two different categories; long and short period multiples. Short period multiples are those where the repeat interval or reverberation time of the multiple is of the same order as the duration of the initiating pulse often known as the source wavelet. The ringing energy of short period multiples can be attenuated successfully using standard deconvolution (Backus, 1959) and will not be addressed in this thesis. Therefore, the term

"multiple", in this thesis, will be restricted to long period multiples where the reverberation time (period) is many times longer than the source wavelet. Figure (1.1) illustrates the basic types of long period multiples.

"Free surface" multiples are those multiples which include the air interface in the reverberation path. The largest amplitude multiple reflections we record are due to the presence of the free surface (Riley and Claerbout, 1976). Free surface multiples can be further divided into multiples involving the water bottom (such as multiple types a and b in Figure (1.1)) and those not involving the water bottom (type c). The surface of the ocean in marine surveys is a near perfect reflector, and when combined with a strong water bottom reflector an energy trap results (Backus, 1959). The energy from the source therefore reverberates in the water layer and is recorded at each arrival at the free surface, with little energy penetrating deeper into the section. On the North West Shelf of Western Australia, this mechanism often accounts for the majority of recorded multiple energy and, indeed, often almost the total energy recorded in marine seismic surveys (Lamont and Uren, 1995).

Seismic multiples often mask and confuse the mapping of true reflecting horizons and, indirectly introduce spurious events in the analysis of subsurface velocities (Riley and Claerbout, 1976). In this way they tend to impede the task of even the experienced seismic interpreter in deducing information from the reflection data.
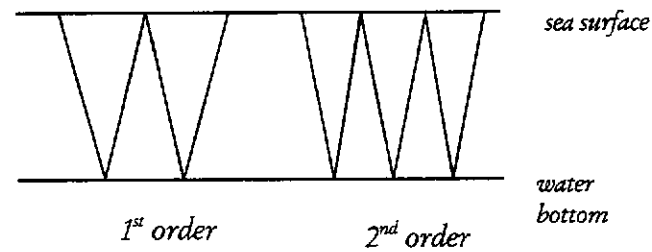
a. Water Bottom Multiples
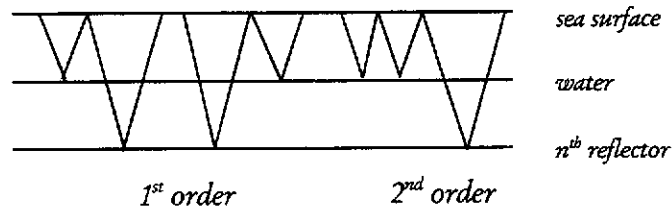
b.   Water Bottom Peg-leg Multiples
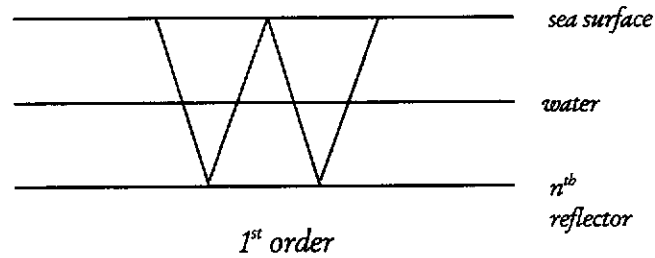
c.   Free   Surface   Related
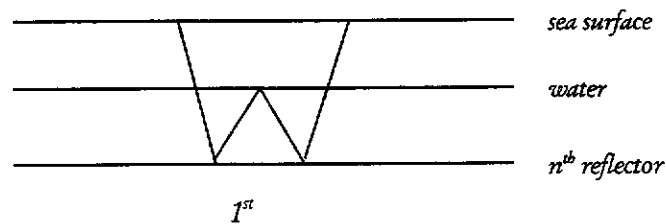
d.   Interbed Multiple

Figure (1.1) The four simple multiple reflection mechanisms.
Naturally any or all of these can also be combined. Diagrams a, b and c show free surface related multiples.

It is important that the multiples are effectively removed from the recorded data without harming the amplitudes of the primary reflections that they obscure. Figure (1.2) shows 2 seismic sections. The first has not received multiple attenuation while the second has. Below 1.2 seconds, before multiple attenuation, the seismic section displays a confused mixture of multiple and primary reflections with conflicting dips making the geology difficult to discern. After multiple attenuation the primary events are clearly visible.

Because of the importance of the multiple phenomenon, much research into multiple attenuation has been carried out. The first dedicated "symposium" on multiples was held in Los Angeles in September 1946. The papers from this conference were published in the January 1948 issue of Geophysics, which was entirely dedicated to multiple reflections. These early papers make fascinating reading and highlight the fact that multiple research spans fifty odd years and yet problems still remain.

Over the years many techniques have been offered for both modelling and attenuating multiples. Some have been adopted in commercial practice.

In order to attenuate the multiples, the seismic data must have a characteristic that can be used to discriminate between primary and multiple events. Often a second dataset is produced which contains the modelled multiples. Generally, an adaptive scheme is used to subtract these modelled multiples from the dataset, as the model is always an approximation only (Berryhill and Kim, 1986).
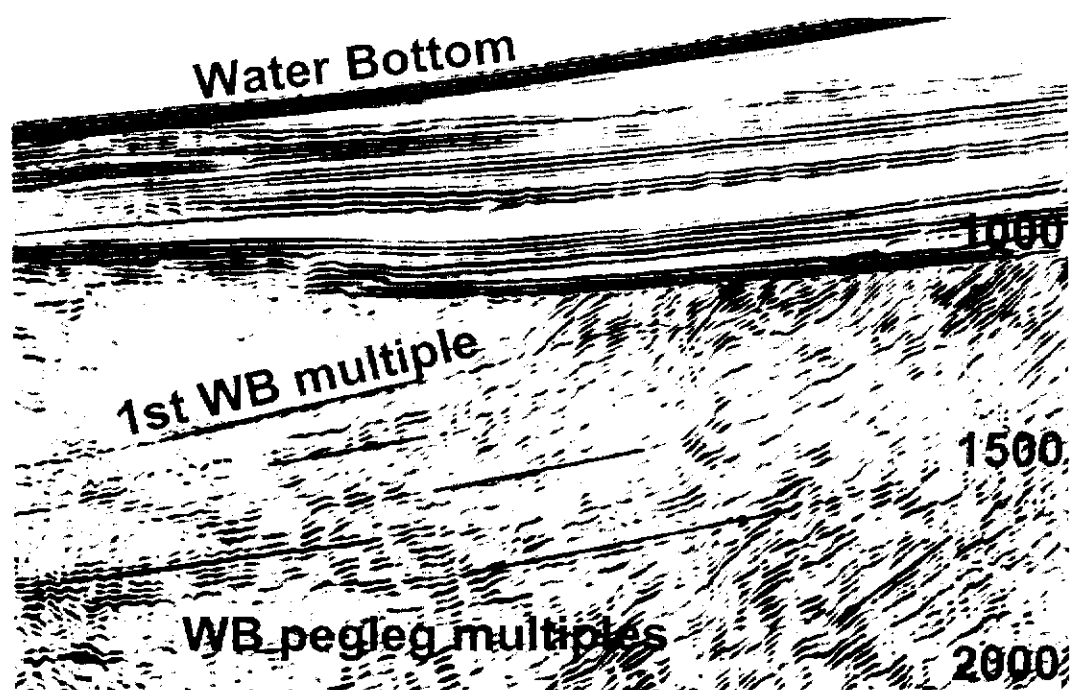
Figure (1.2a)
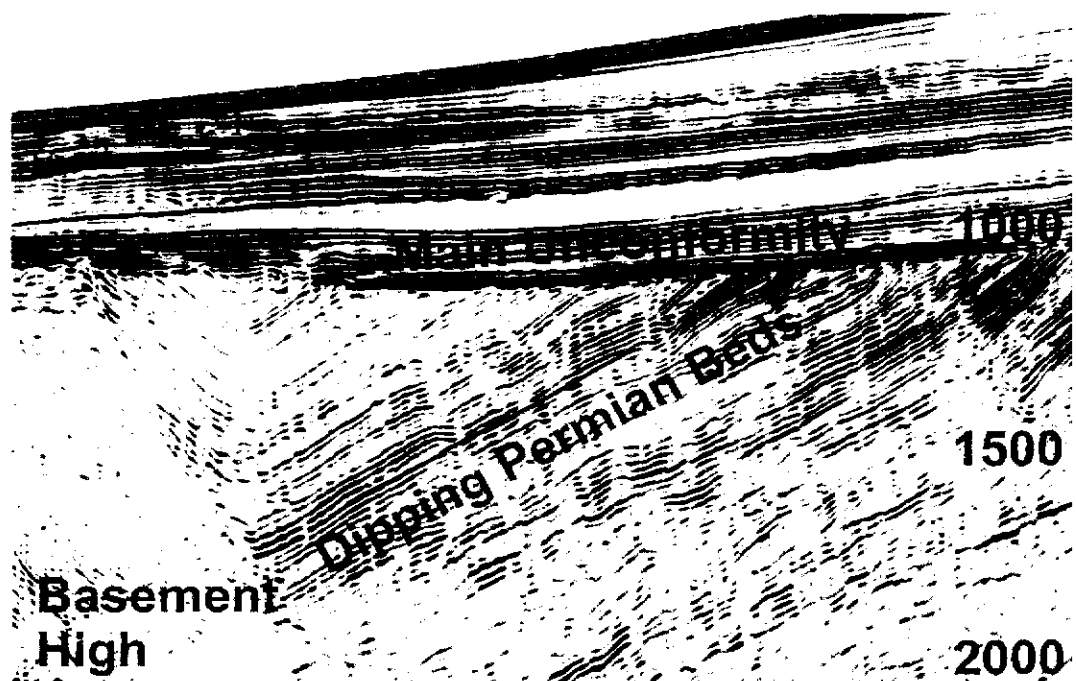
Figure (1.2b)

Figure (1.2) A portion of a seismic line before (a) and after (b) multiple attenuation.
On Section (a) shallow multiples appear as primary reflections from fictitious deeper reflectors. After multiple attenuation the primary events (hence the true geology) are clearly visible.

The most common characteristic used for discrimination is based on the difference in stacking velocity between primary and multiple events. If an event has had multiple reflections in shallow layers, such as the water layer, it will generally arrive at similar overall times as deeper primary reflections, but in doing so will also have traveled at slower acoustic velocities. It should therefore be possible to discriminate between the primary and the multiple reflections based on velocity. This argument assumes that the stacking velocities increase with depth. This is not always the case. For example shallow high velocity carbonates may cause an interval velocity inversion which usually manifests itself as a decrease in the difference in stacking velocities, at depth, between primary and multiple reflections. However, it may result in no velocity difference or possibly in multiples having higher stacking velocities than the primary events they overlay. Naturally, methods based on velocity discrimination fail when there is insufficient difference between primary and multiple velocities (Kneib and Bardan, 1997).

Also the velocities of the primary events need to be known. However, given the ambiguity of picking velocities on multiple affected data, the seismic processor runs the very real risk of either removing primary energy or incompletely removing the multiple energy. Finally, these techniques are often unable to preserve the amplitude of the primary reflections.

Another common characteristic often used to identify and remove multiples, is periodicity. If energy has reverberated between two reflectors, it will manifest itself in the recorded data as a pattern repeated down the shot record. If the assumption is made that the geology does not contain events which are "periodic" then removing

the periodic energy from the shot record amounts to removing multiple energy (Peacock and Treitel, 1969).

Other techniques are based on the fact that the multiples are predictable through modeling using the acoustic wave equation. These methods come in many different forms, and can be very successful. However, they are expensive to use, have their own particular problems and hence do not always produce results of a high standard (Kneib and Bardan, 1997).

The water depths and geology of offshore Australia often lead to seismic data that is heavily contaminated with seismic multiples that are not amenable to attenuation using the available demultiple techniques. Ideally a demultiple technique would:

- require no velocity model (apart from water velocity),
- remove the multiples early on in the processing sequence (so that later processes can be more finely tuned),
- work in shallow and deep water depths,
- preserve primary reflection amplitudes,
- be affordable.

This research is aimed at producing a multiple attenuation method that is effective under these constraints. It is proposed to investigate the application of wavefield transformations to precondition the seismic data prior to the application of existing techniques, and thereby make them more effective.

A more thorough classification of demultiple techniques and a description of how they work together with their particular strengths and weaknesses is given in Chapter 2.

Review Of Existing Techniques

This chapter describes the common multiple attenuation procedures. Emphasis is placed on techniques that are of topical interest, as well as those which are used later as part of attenuation schemes developed in Chapter 3. To begin this chapter, a classification scheme for multiple attenuation methods is described.

Several methods of classifying multiple attenuation procedures have been suggested. Russell et al. (1990) suggests 3 categories: i) those based on stacking, ii) methods relying on muting and, iii) filtering based techniques. This classification scheme is based on the operations that are used to remove the multiples.

The attribute of the seismic data being used to attenuate the multiples is the basis of a classification scheme proposed by Lamont and Uren (1997). They suggested three categories; i) methods which rely on velocity discrimination, ii) methods which rely on the natural periodicity of the multiples or use a transform to introduce periodicity into the multiple trains and, iii) methods which predict the occurrence of the multiples.

This scheme has been extended here to now consist of five categories:

I.   Velocity discrimination based techniques

  - CMP stack

  - FK demultiple

  - Radon Demultiple

II. Periodicity based techniques

  - Predictive deconvolution

  - Radial trace transform

  - τP transforms

III. Model-based prediction techniques

  - Wave equation demultiple

  - Ray tracing based multiple attenuation

IV. Convolution techniques

V.   Eigenvector based techniques

Multiple attenuation will now be discussed under the categories of this extended scheme.

2.1 Methods which rely on velocity discrimination (Category I)

The first category includes processes such as CMP Stack, FK demultiple and Radon Demultiple. While these processes can be very effective and are used routinely in marine seismic processing, there remain a number of problems. All these methods lose effectiveness when the velocity difference between primary and multiple events is reduced.

The velocity field on which the discrimination is based must of course be determined before the demultiple process is applied. The velocity field, or stacking velocity field, is based on the notion of "flattening" the primary events, on the common mid-point (CMP) gather, by the removal of normal moveout. If the multiple contamination is moderate to severe, accurate determination of the velocity field before multiple attenuation is difficult to impossible.

The premise of FK demultiple and Radon Demultiple techniques is to transform the data to a domain where the primary and multiple events separate, mute the multiples and then transform back (or mute the primary energy, transform the multiples back, and then remove them from the original data).

2.1.1 CMP stack

"Stacking" or *"the common reflection point technique"*, (Mayne, 1962; Schneider et al. 1965), is probably the most powerful noise attenuating technique that geophysicists possess. After applying normal moveout with the appropriate velocities, the primary events line up coherently while random noise, multiples and possibly other coherent noise tend not to do so. Therefore, in the stacking process the aligned energy is reinforced while the other energy, is hopefully, stacked out. Stacking is therefore a statistical technique. Harry Mayne understood this in 1962 when he wrote:

> *"the common reflection point technique can be an excellent tool*
>
> *in reducing multiple reflections even though their source in*
>
> *many cases cannot be precisely determined."*

The stacking process can give up to 20 decibels attenuation (Tsai, 1985). It acts as a low pass multiple filter, rejecting to some extent, frequencies greater than the reciprocal of the multiples' residual moveout on the farthest offset trace (Schoenberger, 1996). The effectiveness of stacking can be improved by applying a weighting scheme to the offsets before stacking. The weights are chosen so that the offsets where maximum multiple cancellation will occur are emphasized. The multiple frequency content, the primary velocity field and the water depth determine the choice of weights (Schoenberger, 1996). The weighting schemes lessen the influence of the near offset traces, where the hyperbolic moveout curves of the multiples are nearly flat and reduce the influence of the far offsets where aliasing of

the multiples can be a problem (Yang, 1989). Unfortunately they can reduce the signal to noise ratio through an effective reduction in stacking fold.

Aliasing of multiples is simply caused by insufficient spatial sampling. Figure (2.1) is a field data example where even after applying NMO, (primary event A is flattened) the dip of the multiples, (events B and C) has caused most of the frequencies present in the wavelet at further offsets, to be beyond the spatial Nyquist Frequency (McGillem and Cooper, 1991), and hence to be spatially aliased. This aliased energy has leaked through to the stack, causing severe distortion of primary energy below events B and C.

Obviously stacking relies on moveout differences between primary and multiple data. As moveout differences decrease, the effectiveness of stacking as an attenuator of multiples decreases. On the North West shelf of Australia, velocity inversions often occur beneath shallow carbonates, resulting in little moveout difference between primary and multiple events.

The other inherent shortcoming of the technique is that it cannot produce multiple free, prestack data for a quantitative interpretation. This can be partially overcome by, for example, using near and far offset stacks. The multiple attenuating power of the stack is then, however, compromised. Stacking, especially weighted stacking can be effective at removing multiples, however an additional specific pre-stack multiple attenuation technique is generally necessary.
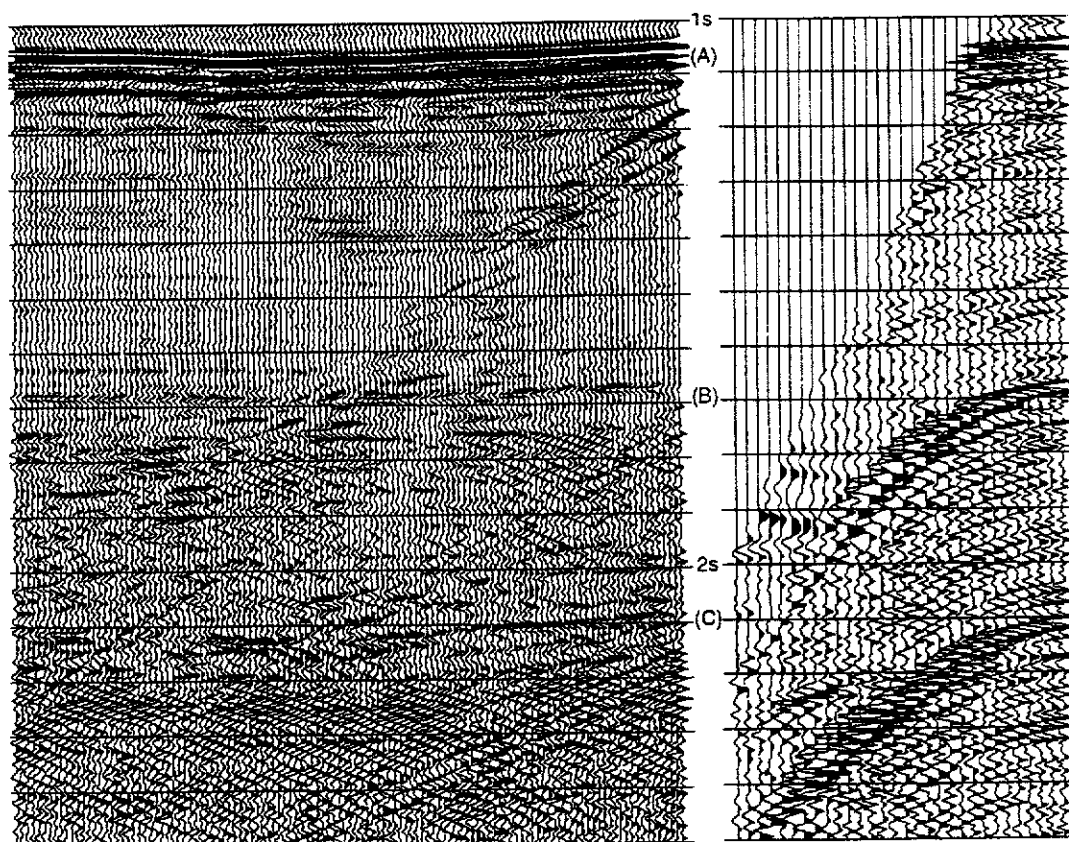
Figure (2.1) *CMP gather and stack illustrating the aliasing of multiples.*

    This figure illustrates how aliased multiples can leak through to the stack. The CDP
    gather (on the right) has been NMO corrected. On the stack, the aliasing due to
    multiple interference can be seen below events B and C. (from CGG brochure
    "Prestack Wavefield Dealiasing")

2.1.2 FK demultiple

The two-dimensional Fourier Domain (frequency - wavenumber or FK) has traditionally been used for low cost effective attenuation of multiples. Amongst the earliest papers were those by Smith (1958) and Embree et al. (1963), where use of the FK domain was first suggested for multiple attenuation.

The FK domain can be used to discriminate events on the basis of gradient on offset-time plots. Therefore, multiples can be removed by muting if there is dip discrimination between multiple and primary events. FK demultiple is applied after NMO correction. Generally an intermediate NMO correction is applied (anywhere between 85 and 95% of stacking velocities) to the CMP gather so that multiple events are under-corrected and primary events are over-corrected. This results, in the FK domain, in primary events mapping to the positive quadrant and multiples mapping to the negative quadrant. The multiples are then muted and the record transformed back to the x-t domain.

Spatial aliasing can be a problem at far offsets if the residual moveout of the multiple events causes a significant number of the spatial frequencies present to be beyond the Nyquist Frequency. This results in a degradation of the results from demultiple processing. It becomes a serious problem if the aliased energy crosses over the $K = O$ axis within the useable frequency range (Yilmaz, 1987).

For the FK method to be successful, there needs to be differential moveout of 50 milliseconds or greater between primary and multiple events (Hardy and Hobbs,

1991). At near offsets, very little dip discrimination exists and therefore multiples are not attenuated in this region of the shot record. This means that FK demultiple and weighted stacking go nicely together. To avoid the Gibbs Phenomenon, the pass zones in the FK domain need to be heavily tapered. This makes it difficult to cleanly separate primary and multiple events, with the result that the multiples are often attenuated along with some of the primary energy. The push for true amplitude processing has therefore seen the demise of FK demultiple techniques.

2.1.3 Radon Demultiple

Unlike FK demultiple, Radon Demultiple is currently a popular process, capable of reasonable amplitude preservation. The name "Radon Transforms", is used here to refer to the group of processes that perform decomposition of CMP gathers based on the moveout differences of the data along either parabolic or hyperbolic basis functions. This is in contrast to the group of processes that use linear basis functions and are referred to as τP transforms in this thesis.

When used for multiple attenuation purposes, the τP transforms are generally used as a data preconditioning process after which predictive deconvolution is more effective. Details are given in Chapter (2.2.3). On the other hand, Radon Demultiple is based on the ability of the Radon Transform to map primary and multiple data to different areas in a transform space, and hence are akin to FK demultiple processes. The transform space, however, is termed the τP domain - independent of which transform is used.

The movement of data into the τP domain can be thought of as either a transform (analogous to the τP transform) or as a modelling system (Hampson, 1986).

If implemented as a transform, the τP traces are calculated by summing (or stacking) the data along basis functions in the CMP domain. However, artefacts are introduced to the transform domain because of the finite offset window used and the fact that the commonly used basis functions do not form an orthonormal basis (Marfurt et al., 1996). Resolution can be improved by modelling the events using a

least squares fit and a deconvolution step (Thorson and Claerbout, 1985). This approach is however, more expensive. Zhou and Greenhalgh (1994) have given an excellent summary of the various implementations.

The more closely the basis functions match the moveout of the events, the better the separation of multiples and primaries in the transform domain (Foster and Mosher, 1992). Hampson (1986) showed that if the data are NMO corrected, then parabolic basis functions can be used to model the data in the CMP domain. That is, the NMO corrected events are approximately parabolic.

These parabolae are of the form $T = \tau + PX^2$, in which T is the two-way travel time, τ the intercept time at zero offset, X the offset and P the parameter governing the moveout. Then a parabolic event with a constant wavelet is described by a set of parabolae, all having an identical value of P, but different values of τ.

Thorson and Claerbout (1985) used hyperbolic basis functions of the form: $T = (\tau^2 + P^2 X^2)^{\frac{1}{2}}$. Russell et al. (1990) make the point that the introduction of the square root sign makes the equation highly non-linear and therefore the necessary matrix inversion becomes time consuming. It is advantageous for the basis functions to be time invariant in order for the computations to be done in the space-frequency domain for efficiency purposes.

Foster and Mosher (1992) presented a modified hyperbolic equation that required the same computation effort as the parabolic function. This modified hyperbolic

equation has the form: $T = \tau + P\left[\left(X^2 + Z_{ref}^2\right)^{\frac{1}{2}} - Z_{ref}\right]$. It can be seen that this

equation is time invariant and the matrix operators have a Toeplitz structure (allowing the use of fast solvers). As mentioned previously, the use of the hyperbolic form allows better focussing of events in the transform domain and therefore better separation of primary and multiple events. However, parabolic basis functions are the most commonly used.

Because of the move out difference, primary and multiple events will map to different P ranges. For instance, after NMO correction using primary velocities, the primaries map around $P=0$ and multiples are mapped at higher P-values. Multiple attenuation can be performed by muting that part of the transform domain where the multiples are mapped and subsequently transforming the data back to the x-t domain. Alternatively, the primaries may be muted in the transform domain, followed by backward transformation and subtraction of the resulting multiple model from the input CMP data.

For effective multiple attenuation, coherent noise events should be included in the modelling range (Marfurt et al., 1996). The P range should be chosen so that all data is included but not so large as to cause aliasing. Equation (2.1) describes the aliasing condition for parabolic basis functions:

$$\text{maximum P - minimum P} \leq \frac{\text{maximum offset}}{2 f \Delta x} \tag{2.1}$$

- maximum P is the largest P value (greatest moveout modelled)
- minimum P is the smallest P value

- f is the largest frequency in hertz

- Δx is the spatial sampling in the same units as the maximum offset

The frequency range must be large enough to include all the energy in the data.

The aliasing condition above should be satisfied for every frequency. However, if a conflict exists between events which need to be removed (large P's) and aliasing, the aliasing condition can be relaxed, however the *dominant* frequency should never be aliased. The frequency range should be measured at far offsets after NMO.

The effects of aliasing start out subtly but progressively degrade the far offset data with high frequency effects. Fundamentally, aliasing gives the energy two or more places to go in the transform domain. Some of the multiple energy is aliased to the primary region of the transform domain and left in by the filter. Conversely some of the high frequencies of the primaries at the far offset are aliased into the multiple region of the τP domain and removed by the filter.

Therefore, at the end of the day some high frequency noise is introduced at far offsets along with the loss of some of the high frequency content of the primary data at these offsets.

A second aliasing condition exists constraining the sampling of P in the transform domain. For parabolic basis functions;

$$\Delta P = \frac{maximumP - minimumP}{numberP - 1} \leq \frac{1}{2f} \qquad (2.2)$$

In addition to the definitions given previously:

ΔP is the P sampling interval,

numberP is the number of P values used in the transform.

Failing to satisfy this constraint will cause high frequency wrap around effects between the near and far offsets.

Given the correct velocity field and adequate moveout differences between primary and multiple events, Radon Demultiple can be very effective. It is very important to adequately sample the P range, which makes Radon Demultiple quite expensive.

The more approximate the parabolic assumption, the more P values that need to be used. A dipping sea floor will cause the apices of peg-leg multiples to be away from zero offset in both the shot and CMP domains. Complex geology will likewise cause non-hyperbolic/parabolic moveout curves. Therefore, Radon Demultiple is less effective in both of these situations but can be adequate if a greater P range and finer sampling in the transform are used.

2.2 Periodicity based techniques (Category II)

This second category includes the application of predictive deconvolution directly to seismic data as well as the combination of preconditioning processes and predictive deconvolution.

The preconditioning transforms include processes such as τP transforms (Carrion, 1986), and radial trace transforms (Taner, 1980). These techniques transform the data to domains which simulate different recording geometries.

The τP transform (point source implementation) simulates data recorded with plane waves. Each trace in the radial trace domain is recorded as if at zero time the source and the receiver were coincident at the shot location and as time progresses the receiver moves away from the source at a steady pace. Given that water bottom multiple energy for a horizontal sea floor hits the water-air interface at regular intervals, it is easy to understand why multiples are periodic on radial traces.

2.2.1 Predictive deconvolution

Standard 1D, minimum phase predictive deconvolution has a very long research history and is generally well understood by exploration geophysicists (Morley and Claerbout, 1983). Robinson (1957) introduced Wiener prediction techniques for the suppression of multiples. In 1959 Backus introduced the 3 point inverse operator. The work was then continued by Kunetz (1961), Kunetz and Fourman (1968), Silverman and Sparks (1965), and Watson (1965). Then Peacock and Treitel (1969) formally described predictive deconvolution. Since then many authors have described the application of predictive deconvolution (Morley and Claerbout, 1983; Gibson and Larner, 1984) and other variations of the technique (Sinton et al., 1978; Taner et al., 1995; Taylor et al., 1979) leading to the routine application of predictive deconvolution in commercial seismic processing.

Predictive deconvolution comprises of two steps (Graul, 1998):

1) predict future values of the waveform based on statistics (from the autocorrelation) and on recent values of the trace.

2) subtract the predicted values from the actual values. The prediction error (actual – predicted) may be considered as the reflectivity in the noise free case.

In practice, predictive deconvolution uses Wiener-Levinson Recursion to solve a system of normal equations derived from a least squares prediction error criterion (the prediction error in part 2 above). Because the autocorrelation is the basis for predicting future events, the events (multiples) must be periodic within a derivation/application window and the primary events should not be periodic. In

the normal pre-stack x-t space, water bottom multiples are actually periodic only at zero offset and then only in the case of a horizontal sea floor. As zero offset traces are not normally recorded, true periodicity is never observed (Haskey and Ashdown, 1991). However, for shallower water depths (shorter period multiples) periodicity holds approximately in a limited window. It has been suggested by Sinton et al. (1978) and De Pledge and Uren (1993), that the periodicity can be addressed by applying NMO to the traces prior to the application of predictive deconvolution. Naturally this introduces differential stretch down each trace and so it comes down to choosing the lesser of two evils. In addition predictive deconvolution does not address the fact that on each trace the multiples have had a more vertical travel path than the primary reflections through the water and hence have different angles of incidence at each reflection point.

In addition to the periodicity problems discussed above, designing prediction error filters for longer period multiples also suffers from the windowing effect due to the assumption that a true autoconvolution function can be computed from a finite portion of data (Taner et al., 1995). The main problem is that the wavelets are truncated at the start and finish of the window. One proposed solution (Taner et al., 1995) is to avoid using the autocorrelation by not forming the standard normal equations, but rather use gradient techniques to solve the modified equations. This paper also proposes a solution to the lack of periodicity of multiples by using a multichannel approach.

In summary, predictive deconvolution is and has been an industry workhorse for many years. It is however not very successful at removing longer period multiples in the x-t domain. It can be very effective at removing "ringing" multiple energy (Hardy and Hobbs, 1991). Predictive deconvolution can introduce spurious events and needs to be applied with care. The next two sections will discuss data transforms which will help overcome some of the problems mentioned above.

2.2.2 Radial trace transforms

As mentioned previously, predictive deconvolution in the time-offset space is not very effective at removing longer period multiples. This is mainly due to the lack of periodicity in the primary/multiple train, the autocorrelation assumption and to a lesser extent, because amplitudes are affected by the variation of angle of incidence, of each event, on each trace in the time - offset (t-x) domain (Taner, 1980).

However, along radial trajectories (that is straight lines through the origin at zero time and zero offset), fanning out through the data in the t-x domain, the water bottom primary and simple water bottom multiples are periodic given a horizontal sea floor (Taner, 1980). In addition, on each radial trace the events have all experienced the same common angle at shot emergence, receiver incidence, and at each bounce at the water bottom and water-air interfaces (see Figure (2.2)). These events then approximately form a stationary time series, and are amenable to predictive deconvolution and autoconvolution (see Chapter (2.4)). They only approximate a stationary time series because this process has not accounted for three-dimensional (3D) effects as well as the effects of attenuation, scattering, mode conversions and so forth. Because the multiples are now approximately periodic, longer windows can be used in the design of the prediction error filters. This makes the autocorrelation assumption more valid.
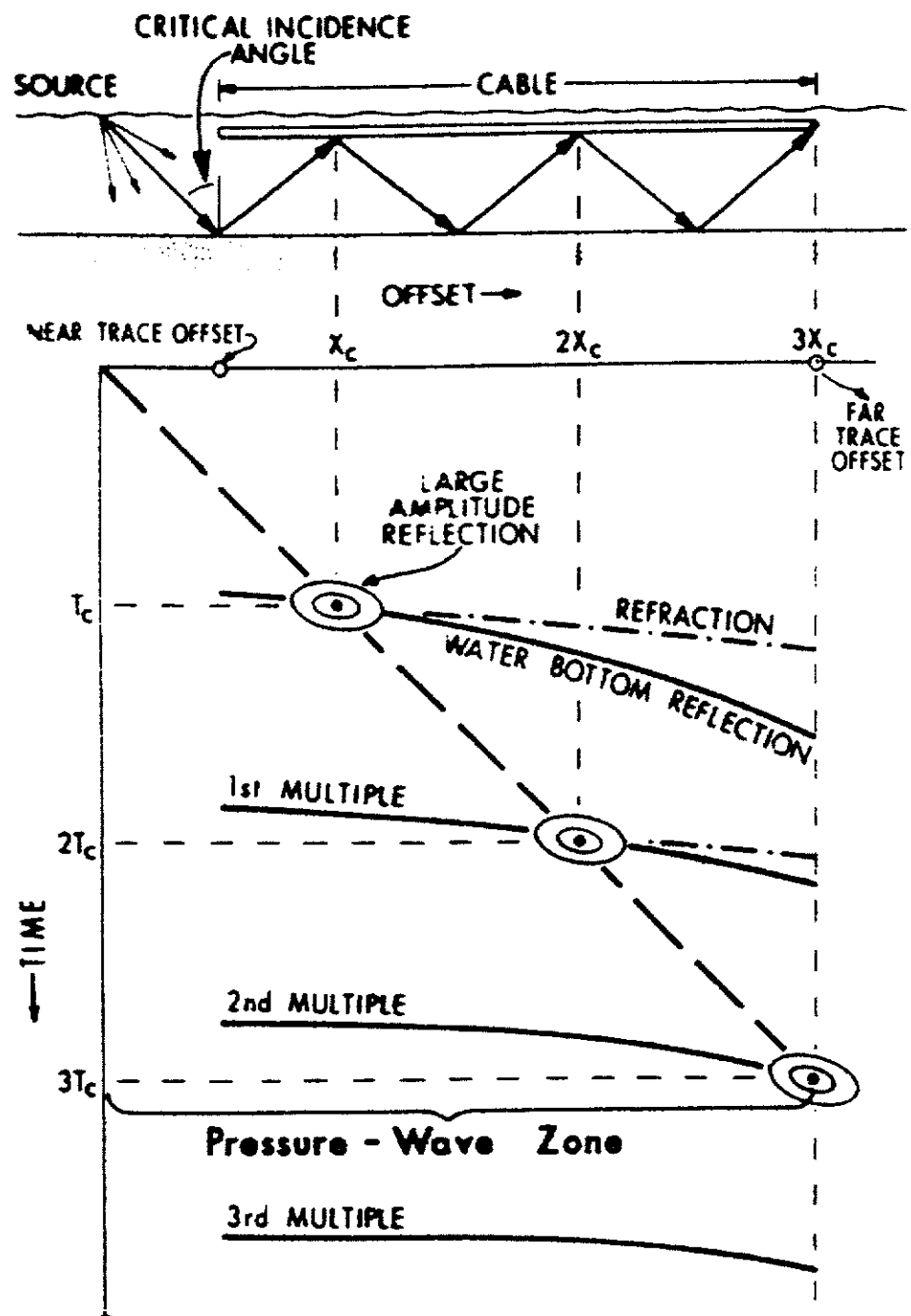
Figure (2.2) Time-offset relationship of critical angle reflections for a horizontal sea floor (Taner, 1980).

To use this periodicity, Taner (1980) suggested a method called *"Radial Multiple Suppression"*. Because of the coarse spatial sampling of seismic data, Taner does not try to form radial traces. Rather the data is divided into segments (time windows). Then to predict the multiples on a trace segment, another trace segment along the radial direction one multiple bounce closer to the source is used. In this manner the predictive deconvolution filters may be designed and the multiples in the shot record consequently attenuated.

Klotz (pers. comm.), of Western Atlas commercially implemented a continuous radial trace transform, where radial traces are formed by mapping the data onto radial trajectories.

The missing near offset traces (including the zero offset trace) also need to be extrapolated from the data which has been recorded. The period of the multiples changes from trace to trace in the radial trace domain. Therefore in order to do ensemble-type deconvolution where the auto- and cross-correlations of several traces are summed prior to the derivation of the filter (in order to improve statistics), the radial traces need to be sorted into the common radial trace domain.

2.2.3 τP transforms

τP transforms can be implemented in several different forms. The simplest implementation involves summing the gather along lines of constant dip either in the time domain or the equivalent operation in the frequency domain (Benoliel et al., 1987). This is commonly known as the delay and sum τP transform. This method has no physical significance, because it is only a true τP transformation in the sense of producing the plane wave response of a horizontally layered medium at each slowness with a line source (Kappus et al., 1990). This 2D method results in output with incorrect amplitudes and phases. Kappus et al. (1990) presents a good comparison of the various implementations. Various transforms exist including implementations derived from the solution of the wave equation for a point source. A point source is a much better approximation to a true seismic source than a line source. These solutions produce data with true amplitudes and phases for flat subsurface layers, but are more computer intensive and are also more prone to aliasing.

τP transforms act as mixing filters (Benoliel et al., 1987) and have been used for this purpose. This can be a drawback of τP transforms as fine reflector detail may be lost. Benoliel et al. (1987) also say that multiple suppression in the τP domain is at least as effective as in the t-x domain. This is because once in the τP domain, the simple water bottom multiples are exactly periodic for a horizontal subsurface and for a particular ray parameter (Alam and Austin, 1981; Diebold and Stoffa, 1981; Benoliel et al., 1987; Kappus et al., 1990; Treitel et al., 1982).

Therefore predictive deconvolution can be applied in the τP domain, to utilise the periodicity. However some problems remain. The suppression of water layer peg-legs requires a second order operator while the conventional predictive deconvolution operator is a first order operator. Therefore simultaneous removal of both types of multiples is impossible using predictive deconvolution (Lokshtanov and Sagehaug, 1995).

Summary

The periodicity gained by the τP transform is the same as that gained by a radial trace transform. In fact the τP domain might be considered as a more general form of this operation (Taner et al., 1995). Compared with the radial trace transforms, τP transforms are very expensive. Even so they are generally the favoured option because they can be a true plane wave decomposition. In addition radial trace transforms require spatial interpolation as well as temporal interpolation. Radial trace transforms also require near offset traces in order to have radial traces starting from zero time. τP transforms do not necessarily need these, however by forming fully populated, split spread, shot records (using reciprocity) line sources can be better simulated (Taner, pers. comm.). Hence the phase and amplitude distortions of the simple delay and sum τP transform may be avoided. The formation of these split spread shot records necessarily means the synthesis of the near offset traces. In summary both the τP and the radial trace transforms achieve the same degree of periodicity. The radial trace transform is by far the cheapest option. There are pros and cons for both transforms and both assume a 1D earth.

2.3 Model based methods which predict the occurrence of the multiples (Category III)

The third category contains methods such as wave equation demultiple and ray tracing based demultiple. Both of these techniques can handle uneven/rugose sea floors, but are computationally expensive to apply. These processes do not require moveout differences between primary and multiple events.

2.3.1 Wave equation based demultiple

The wave equation based demultiple process is formulated to remove water bottom related multiples (type a and b in Figure (1.1)). In doing so it requires a model of the water layer including water bottom depth and reflectivity combined with the water velocity.

The basis of the technique is to move the data to later times by spatial and temporal extrapolation using the acoustic wave equation (that is by adding an additional round trip through the water). Then after combining the reflectivity with this data, a model of the water bottom multiples is obtained. This model data is then subtracted from the original data.

Wave equation techniques were first introduced for multiple attenuation in the CMP domain by Loewenthal et al. (1974). Morley (1982), Bernth and Sonneland (1983), Berryhill and Kim (1986), Levin (1987) and Wiggins (1988), developed the technique into a more accurate process able to model rugose sea floors with laterally changing reflectivity. They applied the technique to shot records.

When the technique is applied to shot records, the receiver side water bottom peg leg multiples are modelled. However, to model the shot side peg legs, the data needs to be sorted to receiver gathers and the extrapolation and subtraction applied again. The main difficulties with the technique are i) the lack of near offset traces, and ii) computation times required. Before application, the near offset traces need to be accurately modelled, which is especially difficult for shallow water depths. The process is expensive (even with modern hardware) and exorbitant if both source and

receiver side peg legs are to be removed. The results never quite live up to expectations (Kneib and Bardan, 1997).

Haase (1992) proposed the application of wave equation demultiple in the common offset domain, hence avoiding the problem of lack of near offset traces. The results displayed after application of his techniques to field data are less than convincing. Generally the multiple model produced by these techniques is only approximate. This is due to 3D effects not modelled, inaccuracy synthesizing the near offset traces, water bottom reflection coefficient assumptions and so forth. Therefore an adaptive multiple removal procedure is generally required.

2.3.2 Ray tracing based prediction and subtraction of water layer multiples

Calvert (1990) suggests removing multiples by predicting multiple arrival times by ray tracing through a model of the laterally varying water layer and possibly the subsurface. The multiple waveform is estimated by stacking a window of data around the calculated arrival times. The predicted multiples are then subtracted from the prestack data.

Calvert has suggested this technique mainly for water bottom multiples because the water bottom model can be accurately obtained. Because the multiple waveform is obtained by stacking along the trajectory obtained by ray tracing, this technique still relies on velocity discrimination between primary and multiple events. It is also only useful for simple water bottom multiples (category I - Figure (1.1)). It could be useful for removing other categories of multiples if a specific mechanism could be identified, an accurate model constructed, and an appropriate adaptive multiple subtraction technique devised.

2.4 Convolution techniques (Category IV)

Convolution techniques use the data itself to predict the multiples. A trace convolved with itself contains only multiple information (Anstey, 1966). This technique assumes the convolutional model; that a seismic response is a convolution of the Earth's impulse response with a seismic source wavelet. This section will commence by considering, in some detail, autoconvolution (called *event prediction* by De Pledge and Uren, 1993). This will lay the foundation for the 2D techniques, and is also one of the attenuation techniques used in Chapter 3 (along with gapped deconvolution).

Autoconvolution

Figure (2.3) shows a simple model (zero offset, vertical incidence) used to illustrate autoconvolution, where S is the source amplitude and r is the normal incidence amplitude reflection coefficient of the sea floor. It describes the amplitude and polarity of the water bottom primary event along with all orders of water bottom multiples. Each bounce of the energy at the surface can be thought of as coming from a delayed source. No account is taken of amplitude variation due to spherical divergence or absorption.

The left-hand trace in Figure (2.4a) is the zero offset trace recorded from this model. The subsequent traces are the input trace convolved with itself once, twice and so forth, that is in a feedback loop (Anstey, 1966). The most noticeable feature of each of the traces is how the first event on each trace is delayed by the water bottom period multiplied by the number of convolutions involved in producing the trace.
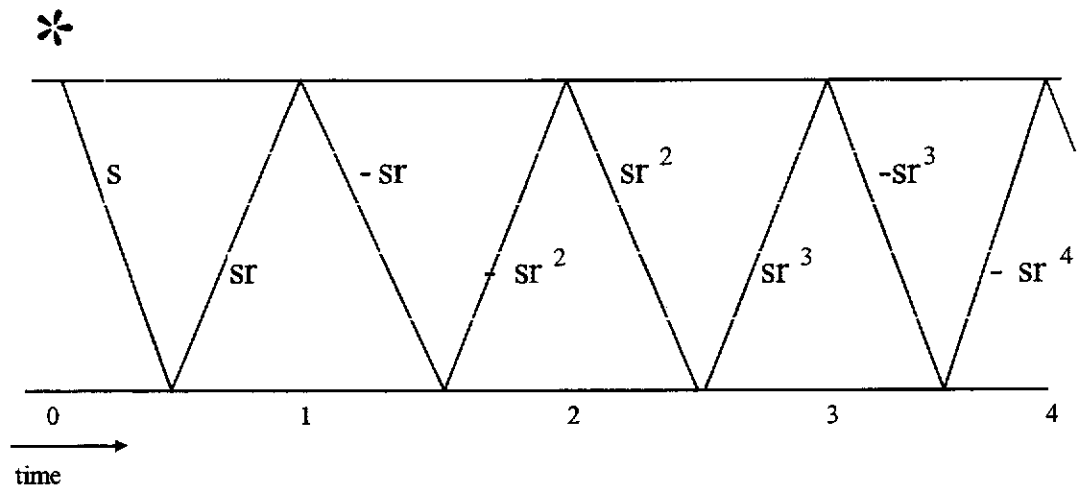
Figure (2.3) *Simple 1D model used to describe the kinetics of autoconvolution.*
s *is the source wavelet,* r *is the reflection coefficient and the horizontal dimension is time.*
That is, the model is representing a zero offset, normal incidence ray path. The diagram is

$$t \qquad t^*t \qquad t(^*t)^2 \qquad t(^*t)^3$$

tim

$-sr$

$--sr^2 \qquad s^2r^2$

$-sr^3 \qquad -2s^2r^3 \qquad s^3r^3$

$--sr^4 \qquad 3s^2r^4 \qquad -3s^3r^4 \qquad s^4r^4$

Figure (2.4a)

$$t \qquad t^*t^*s^{-1} \qquad t(^*t^*s^{-1})^2 \qquad t(^*t^*s^{-1})^3 \qquad p$$

time

$-sr \qquad\qquad\qquad\qquad\qquad\qquad -sr$

$--sr^2 \quad + \quad sr^2$

$-sr^3 \quad + \quad -2sr^3 \quad + \quad sr^3$

$=$

$-sr^4 \qquad 3sr^4 \qquad --3sr^4 \qquad sr^4$
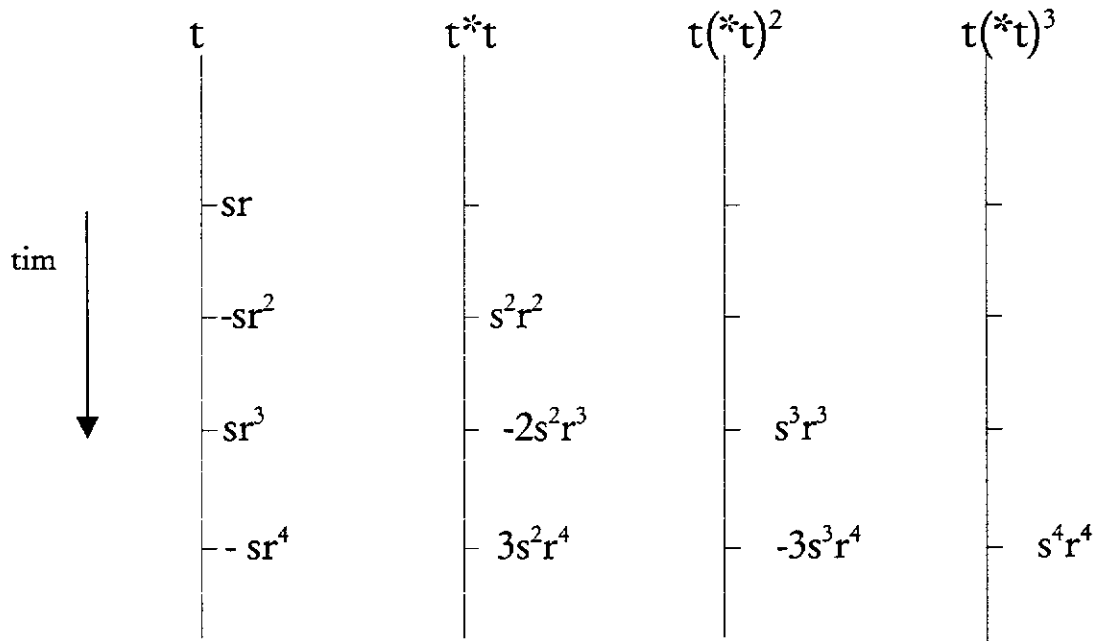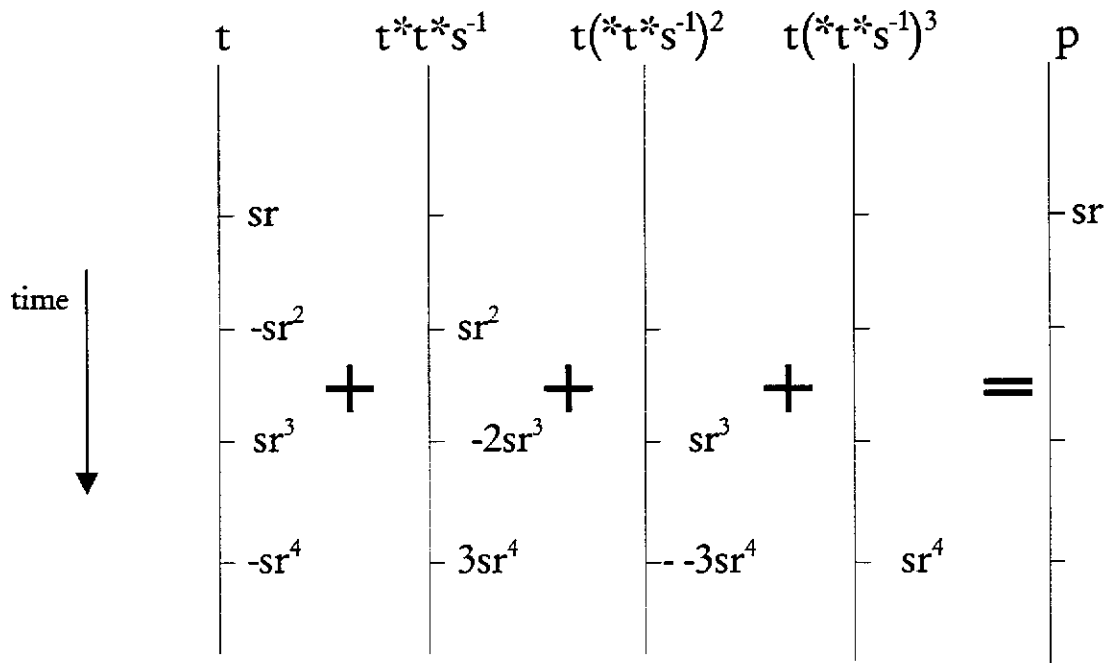
Figure (2.4b)

Figure (2.4) *An illustration of the autoconvolution procedure. The trace t is the trace recorded from the model in Figure (2.3). The symbol r is the reflection coefficient of the sea floor. The * represents convolution. Hence, t*t is the trace convolved with itself once. t(*t)² is the trace convolved with itself twice and so forth as shown in Figure (2.4a). If the traces are then convolved with the inverse of the wavelet the number of times they are autoconvolved, they can then be added together to obtain perfect multiple suppression as shown in trace P; the primaries only trace (Figure (2.4b)).*

If each trace is now convolved with the inverse of the wavelet a number of times equal to the number of times the trace is autoconvolved, then the traces can then be added together as shown in Figure (2.4b) and the multiples cancel out. Note that it is also possible to convolve the inverse of the wavelet with the trace prior to convolution and hence avoid filtering traces multiple times subsequently. However better results have been achieved by filtering the traces after autoconvolution. Figures (2.3) and (2.4) together with this explanation illustrate a 1D version of Equation (3.13) in Verschuur (1991).

Autoconvolution (1-D convolution) can also be illustrated using a very simple synthetic, shown in Figure (2.5a), containing one primary and one simple multiple event. The multiple is simulated to have been reflected off a sea floor with a reflection coefficient of 0.7 and a water - air interface with a reflection coefficient of - 1. This gives the overall effect of a reverse polarity wavelet 0.7 times the amplitude of the primary wavelet. This synthetic trace is then autoconvolved to give the trace shown in Figure (2.5b). The predicted multiple contains an extended wavelet. This extended wavelet can be deconvolved by convolving the trace with the inverse of the wavelet, see Figure (2.5c). The predicted trace is now an estimate of the multiple contained on the original trace but with reverse polarity. When the original and this predicted trace are stacked, the multiple is substantially attenuated as shown in Figure (2.5d).

De Pledge and Uren (1992) used autoconvolution on NMO corrected synthetic data within a CMP gather to predict and subtract multiple events. They NMO corrected
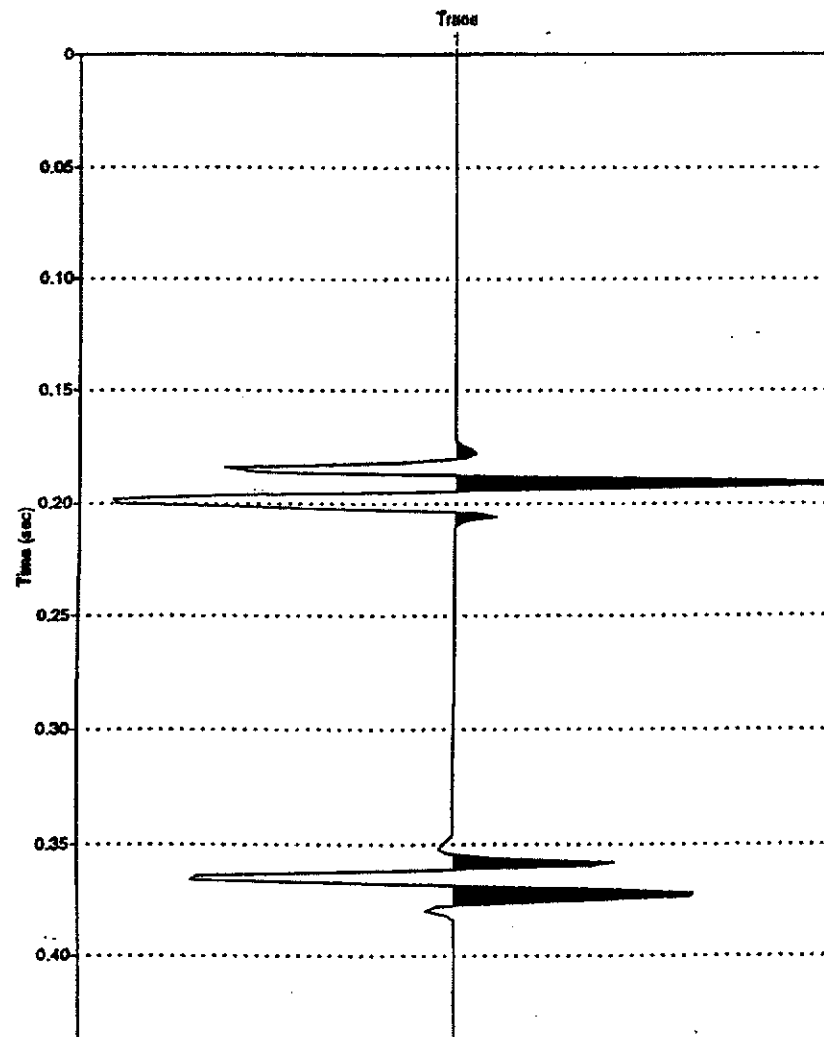
Figure (2.5a) Normal incidence synthetic.

> A synthetic trace is shown containing one primary and one multiple event. The
> multiple is simulated to have been reflected off a sea floor with a reflection coefficient
> of 0.7 and a water -air interface with a reflection coefficient of -1, giving an overall
> effect of a reverse polarity wavelet 0.7 times the amplitude of the primary wavelet.
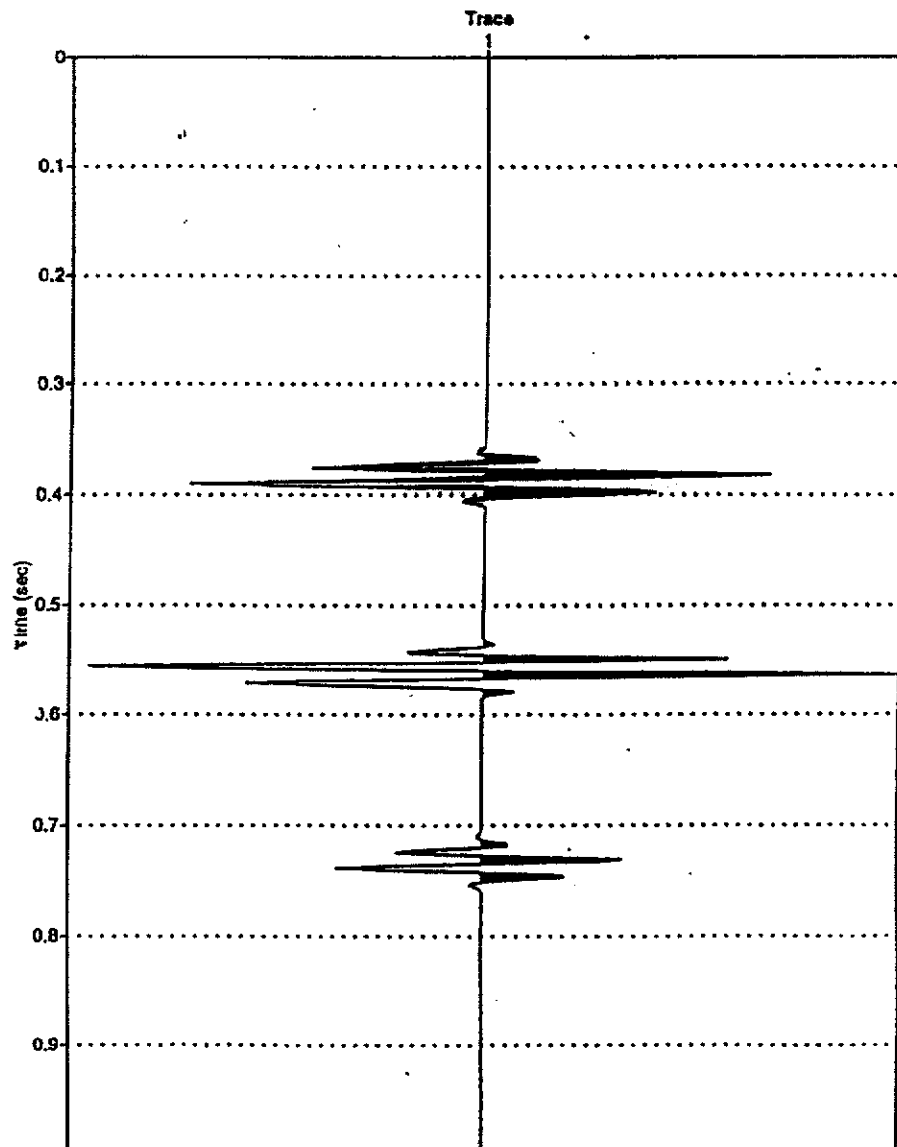
Figure (2.5b) Autoconvolution of the synthetic trace.

Notice that the first event now aligns itself temporally with the multiple in Figure 2.5a.
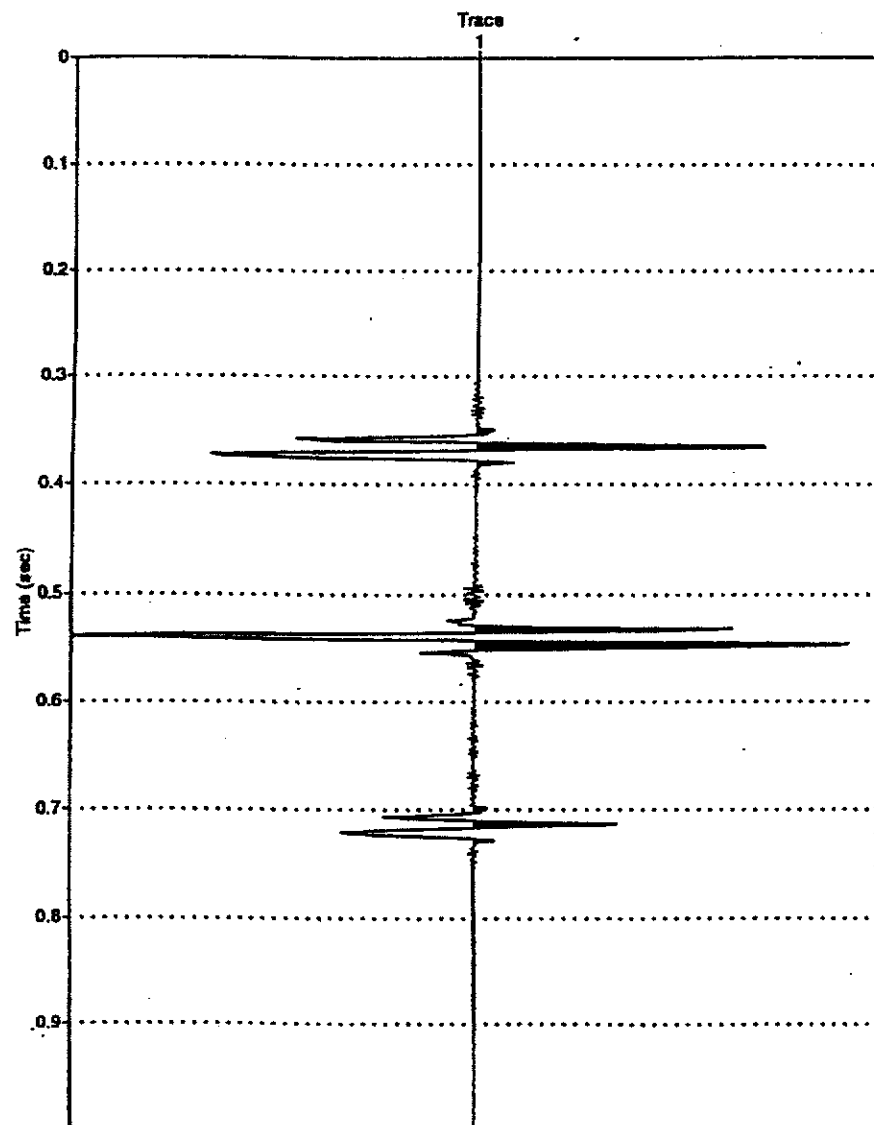
Figure (2.5c)This trace shows the convolution of the inverse of the wavelet with the
autoconvolved trace from Figure 2.5b.

Notice that the original wavelet shape has largely been recovered.
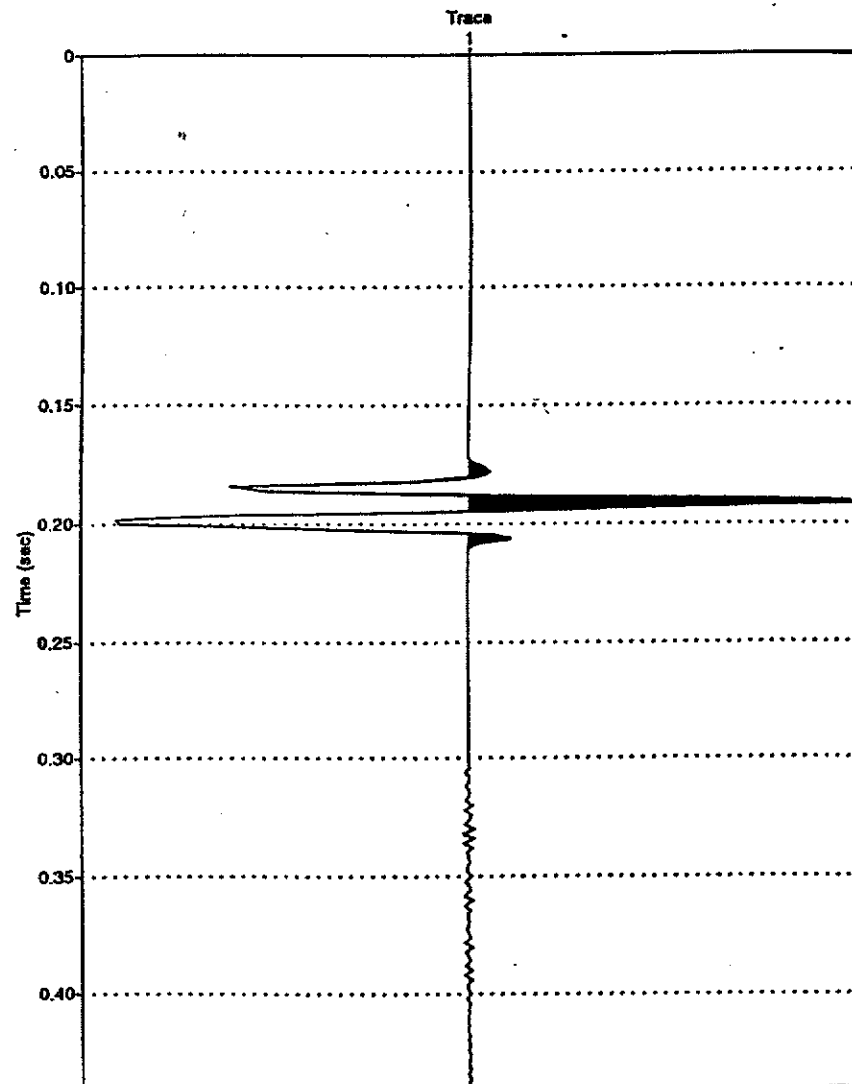
Figure (2.5d)   This final figure is the addition of the trace in Figure 2.5c to the initial trace. Note that the multiple has been cleanly removed.

CMP gathers, thus making the multiples approximately periodic on all traces in the gather. They then applied autoconvolution to attenuate the multiples followed by inverse NMO correction.

De Pledge and Uren (1992) showed the potential of autoconvolution and showed that some form of preconditioning is necessary. As shown, autoconvolution assumes a zero offset trace from a flat sea floor. Perhaps the next simplest preconditioning step (to NMO correction) would be a radial trace transform (as discussed in Chapter (2.2.2)) for data recorded over a horizontal sea floor.

2D convolution based demultiple or surface multiple attenuation (SMA)

SMA is theoretically capable of removing all orders of all surface multiples present within the wavefield (Dragoset and Jericevic, 1997).

As in autoconvolution, the bounce of a wavefront at the free surface can be thought of as coming from a delayed source. Figure (2.6) illustrates this concept. If the shot and receiver spacings are equal in a survey and the data are recorded in a split spread fashion including near offset/zero offset traces, then the two bounces of the wavefront will be recorded as two primaries in the dataset. Then convolving the trace recorded with the shot at A and receiver at B with the trace recorded with the shot at B and receiver at C will predict the multiple at the correct time on the trace recorded with the shot at A and the receiver at C. This is the simple but powerful concept on which SMA is based. Every surface-predictable multiple, no matter how complicated its ray path, consists of segments which, from a surface perspective, are primary events (Dragoset and Jericevic, 1997).

A   B   C

free surface

water bottom

n^{th} *reflector*

Water bottom peg leg ray path
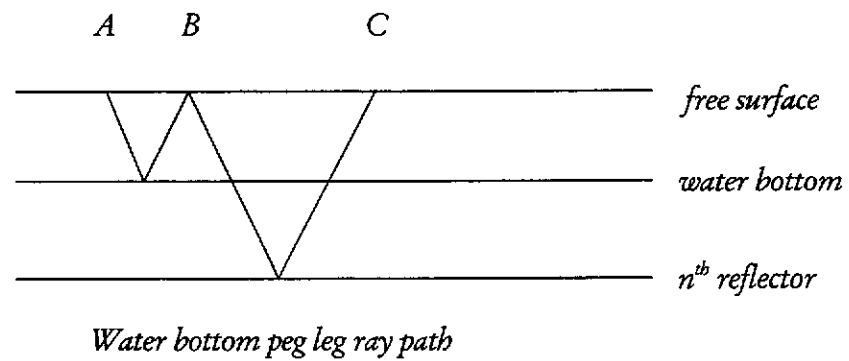
Figure (2.6)   *The ray path of a water bottom peg leg.*

   This illustration shows how the multiple ABC is composed of the primary "pieces"

   AB and BC. This leads to the notion of B being the position of a delayed source .

It is not possible to individually calculate which traces need to be convolved to synthesize the multiples for a particular trace. Indeed the multiples for a particular trace will need to be predicted from several different pairs of traces. In practice this problem is overcome by convolving all traces common to a particular surface location and by then combining them using the Kirchhoff integral to produce the ultimate prediction trace. This is the wave equation consistent solution used by both Verschuur (1991) and by Dragoset and Jericevic (1997). In particular, Dragoset and Jericevic (1997) give a very clear explanation of the derivation of SMA based on the Kirchhoff integral, which is a mathematical statement of Huygens's Principle.

All convolution techniques predict the multiples using the data itself. Hence, the water bottom primary event must be present and in good order for this method to work. This restriction makes SMA unsuitable for shallow water depths.

Finally, the wavelet must be known in order to calculate its inverse. Slight errors in wavelet amplitude and especially in phase lead to gross errors in predicted multiples. A way around the unknown wavelet is to pose the equation as an optimization problem, selecting which wavelet inverse yields the best results, according to some criterion (Dragoset and Jericevic, 1997). The criterion generally used is minimum energy (Verschuur, 1991). The total energy minimum occurs when the inverse wavelet best compensates for the acquisition wavelet, 3D effects and so forth.

SMA is a very elegant technique, which has the potential to remove 95% of the troublesome multiples. However its practical performance to date has been at best inconsistent (Dragoset and Jericevic, 1997).

2.5 Eigenvector based techniques (Category V)

There are several implementations of demultiple procedures in the literature based on eigenvalues (Kneib and Bardan, 1997; Manin and Spitz, 1995). They target a specific mechanism where the primary and multiple events can be easily recognised. In addition, the multiple events need to be approximately parallel to the primary event. The typical multiple class which this technique targets is the water bottom peg-leg from a specific strong reflector.

The basic technique is to pick the strong reflector and then flatten the seismic section on this reflector. The seismic data can then be decomposed using eigenimages following various preconditioning algorithms. Manin and Spitz (1995) use a spectral technique in the frequency-space (FX) domain, Kneib and Bardan (1997) use the covariance matrix of a specific time - space window.

The premise is that the data can then be recomposed without the multiple energy. These techniques are most effective when a clear mechanism exists for the multiples, the multiple energy is the dominant energy, and the primary and multiple energy are not parallel to one another. Hence they are of value on only a very small percentage of actual exploration data sets.

2.6 Summary

The main demultiple procedures in current use have been classified and reviewed. All of these techniques have their own particular strengths and weaknesses. A multiple attenuation strategy based on these existing techniques would use one or a combination of these techniques. The choice of techniques would depend on the specifics of the data set together with the budget and time available. There still remains a pressing need for a multiple attenuation method that can effectively attenuate long period water layer multiples generated from a dipping sea floor.

Multiple removal using preconditioning wavefield transformations

In Chapter (2.2) the main shortcomings of predictive deconvolution in x-t space were discussed:

- Lack of periodicity of multiple trains,

- Limitations of the autocorrelation assumption,

- Change of wavelet shape (due to the variation of angle of incidence) of events on each trace.

For autoconvolution (Chapter (2.4)) to be effective it needs a zero offset trace from a 1D earth. The multiples on such a trace form a stationary time series (ignoring absorption and so forth).

Predictive deconvolution is used to remove periodic energy from records. Autoconvolution predicts surface-related multiples. Therefore, when being used to remove water bottom related multiples the requirements of these two processes are slightly

different. In addition to requiring the water bottom multiples to be periodic, autoconvolution requires the data to resemble zero offset data from a 1D earth. In practice this means that the time down to the water bottom event needs to equal the period of the multiples, and the record above this event needs to be clear of any other events (such as direct arrivals).

Standard finite offset x-t data is far from ideal for input into either operation. Two wavefield transforms have been discussed in Chapter (2.1), as a means of preparing the data for these attenuation techniques:

- radial trace transforms,
- τP transforms.

For a horizontal sea floor water bottom multiples are periodic in these domains and water bottom pegleg multiples are nearly periodic. How well the pegleg multiples are conditioned is determined by the complexity of the geology.

Multiples generated by a dipping sea floor have characteristics, which make them more difficult to attenuate. A very small dip on the water bottom reflector is enough to appreciably change the arrival times of multiples (Levin, 1971). Table (3.1) contains the difference in arrival times along a radial trace between the water bottom multiples for a sea floor with a dip of 0.2 degrees and the expected times (if the multiples were periodic). It demonstrates that especially for higher order multiples, small dips on the sea floor make significant differences. The zero offset time of the water bottom was one second. If no dip were present on the sea floor, the events on a radial trace would be perfectly periodic.

Event	Offset (m)	Arrival time (msec)	Actual -- expected arrival times (msec)
Water bottom (WB) primary	500	1053	
1st WB multiple	1000	2104	2.222
2nd WB multiple	1500	3152	6.683
3rd WB multiple	2000	4199	13.396

Table (3.1) Arrival times of events along one radial trace as well as the difference between the actual arrival times and the expected arrival times (the arrival times should the multiples be periodic) for a model with a sea floor dip of 0.2 degrees.
It illustrates that even for a very mild dip the travel times of the events vary significantly and the periodicity is lost.

The dip will cause water bottom pegleg multiples to have hyperbolic time-distance curves with apices at offsets other than zero on both shot records and CMP gathers (Levin and Shah, 1977). In addition the pegleg events split into 2 or more events (depending on the order of the multiple). This is due to the travel time difference between the up dip and down dip water bottom pegleg ray paths (Figure (3.1)).
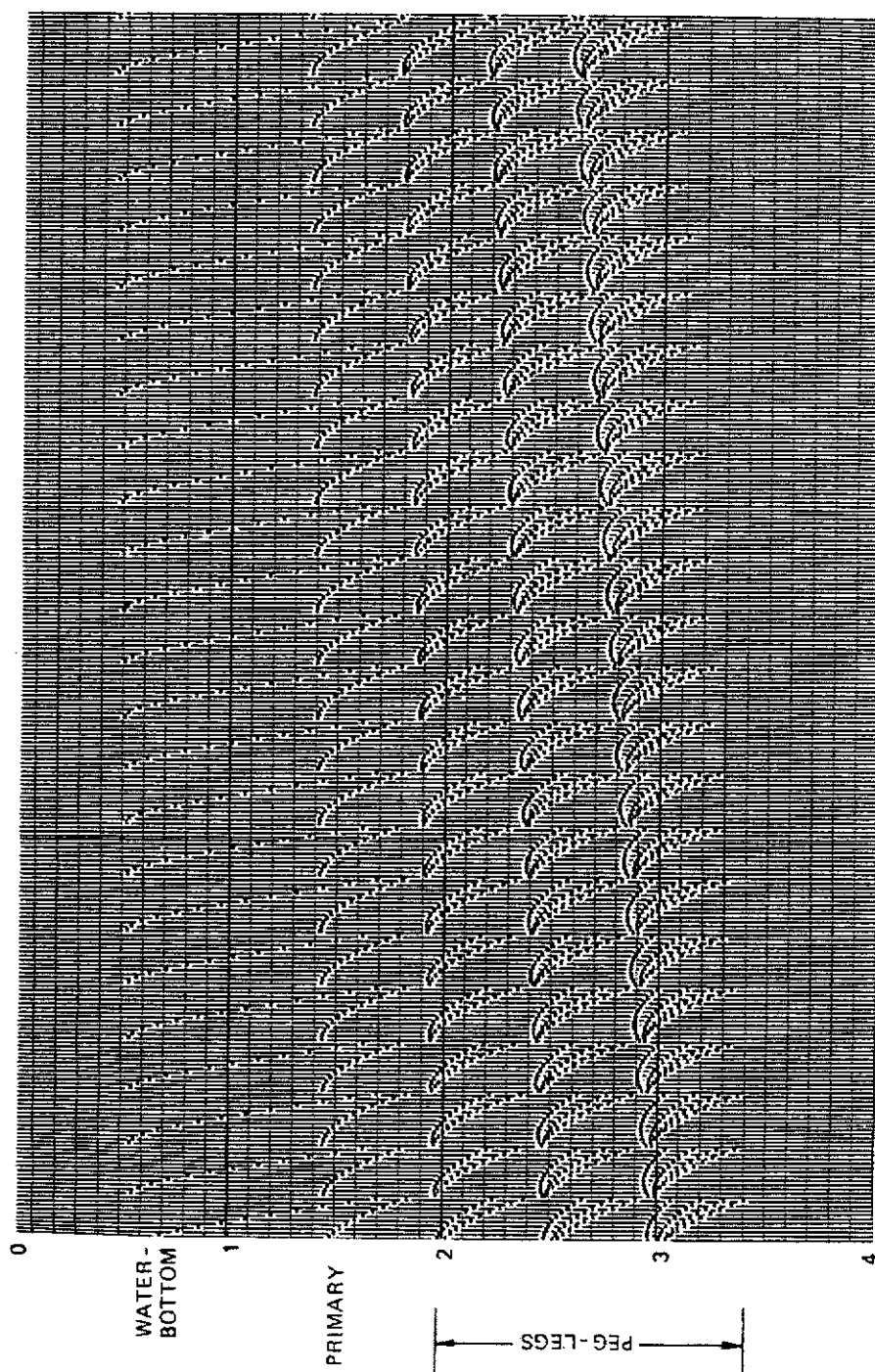
Figure (3.1) *Behaviour of water bottom pegleg multiples, in CMP gathers, for a dipping sea floor.*

The events split because of the difference in travel times between the up dip and down dip water bottom pegleg ray paths. The apices of the pegleg multiples are away from zero offset (Levin and Shah, 1977).

Therefore the radial trace and τP transforms will not produce periodic data if the water

bottom is dipping to any degree. What is needed is a new transform process that will work

for both horizontal and dipping sea floors.

It is possible to "bend" the radial traces in order to introduce periodicity into the water

bottom primary/multiple events for a dipping sea floor. With straight radial traces (and a

horizontal sea floor) the water bottom multiples are naturally periodic both in radial

distance and time (this is illustrated in Figure (2.2)). For a dipping sea floor, the "bent"

radial traces can be curved to introduce periodicity in either time or radial distance.

Curved radial traces which introduce periodicity in the distance between the water bottom

events along the radial traces, were derived by Downie et al. (1995). They prove to be

difficult to implement due to ambiguous units and poor solution approximations as time

approaches zero (Hartley and Lamont, 1996).

By far the simplest approach is to define curved trajectories along which the multiples

would be periodic in time. Spatial interpolation could then be used to map data from the

x-t traces onto these curved trajectories in order to form the new radial traces. The units

of the new traces would still be time. Curved radial traces of both types are derived in a

Curtin University internal report by Hartley and Lamont (1996), which is included as

Appendix A.

One problem with the curved radial trace implementations of Downie et al. (1995) and

Hartley and Lamont (1996) is that they fail to transform a significant proportion of the

gather. This effect is demonstrated in Figure (3.2), which is a plot of the radial trajectories designed to make the multiples periodic in time, for a dipping sea floor (for both the shot and CMP domains). For a shot record (Figure (3.2a)), on the up dip side, the curved trajectories veer quickly away from zero offset. On the down dip side the coverage of the curved trajectories is much improved.

For the CMP domain it is also found that the curved trajectories veer away from zero offset. In both the CMP and shot record domains therefore, the radial trace pattern effectively results in an inner trace mute. For this reason curved radial trace transforms will not be pursued further in this thesis. Some other process will be sought.

An alternative approach to introduce stationarity into the water bottom multiples for both horizontal and dipping sea floors is required. If NMO, with a constant velocity field equal to the water velocity, is applied to data recorded over a horizontal sea floor, the water bottom primary event is flattened. In addition, the simple water bottom multiples are also flattened and as a result form a periodic sequence on each trace (water bottom primary plus multiples). This is illustrated in Figure (3.3). Figure (3.3a) shows the travel time information for the water bottom primary and multiple events for a horizontal sea floor. In Figure (3.3b), NMO (using water velocity) has been applied. The "travel times" are now flat and periodic. However, when applied to trace data, the events do not form a

Normalised Offset

Down dip side

Up dip side

Radial trajectories

Water bottom
multiple events

Time

Figure (3.2a)

Normalised Offset

Water bottom primary event

Curved trajectories

Time

Water bottom multiples
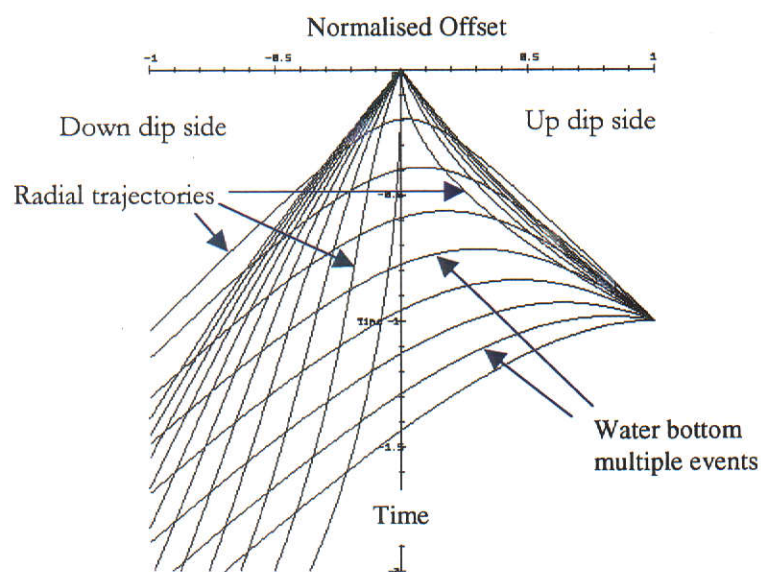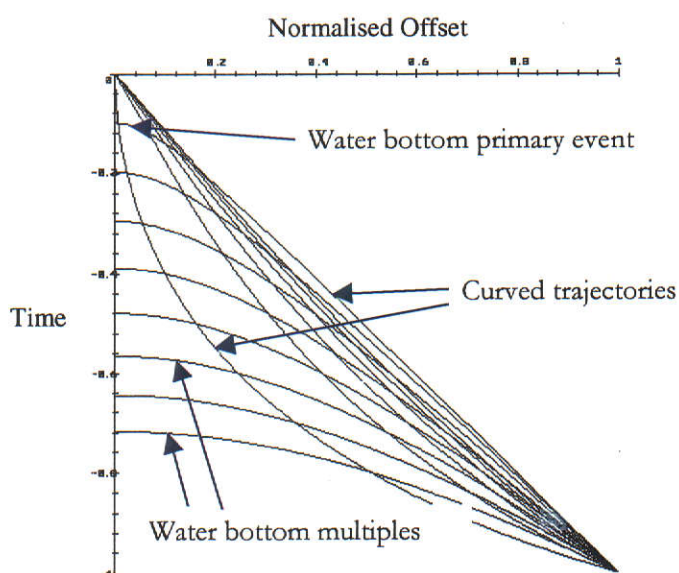
Figure (3.2b)

Figure (3.2) Time basis radial trace trajectories overlaid on the water bottom events for a shot record (a) and a CMP gather (b).
Notice that the trajectories in all cases veer away from zero offset, which would result in the equivalent of an inner trace mute.
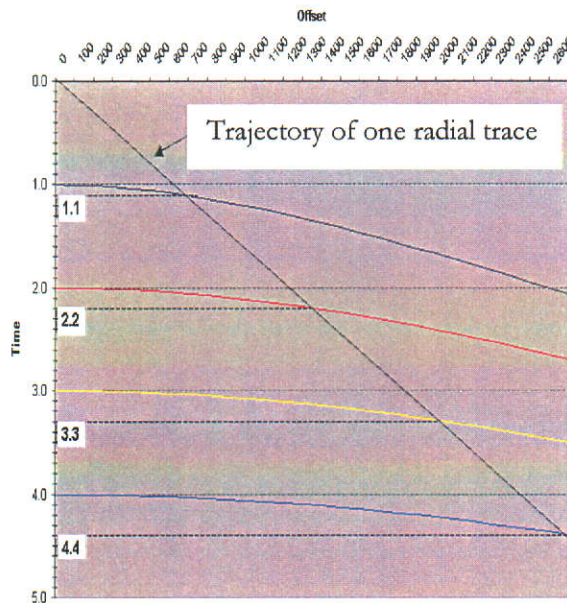
Figure (3.3a)
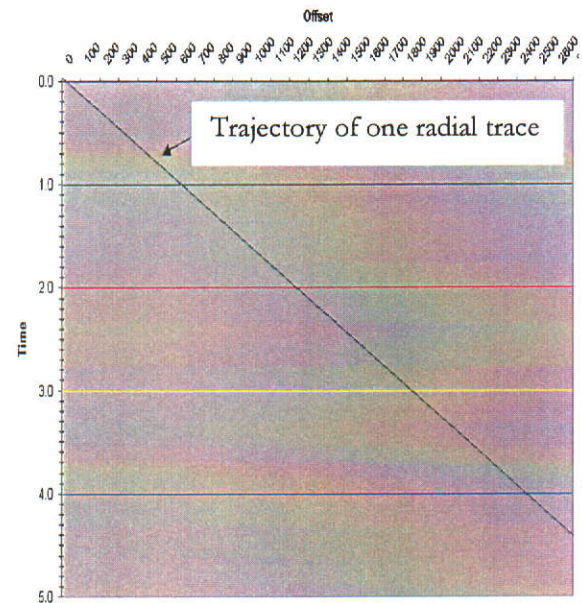
Figure (3.3b)
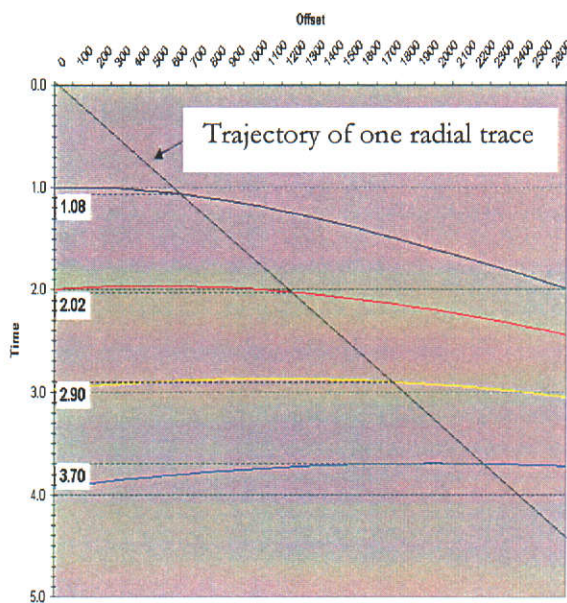
Figure (3.3c)
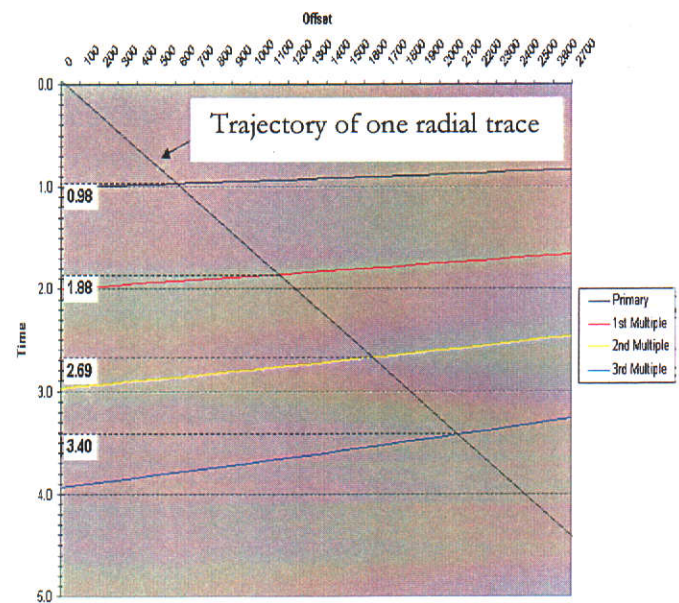
Figure (3.3d)

Figure (3.3)   An illustration of the travel time behavior of water bottom multiples.
The diagrams show the water bottom primary event and the first three multiples for a;
a)   *non-dipping sea floor,*
b)   *non-dipping sea floor after NMO (standard NMO with velocity=1500 m/sec),*
c)   *sea floor dipping at 5 degrees,*
d)   *sea floor dipping at 5 degrees after NMO (standard NMO with velocity=1500 m/sec).*
For a non-dipping sea floor, the water bottom primary/multiple events are periodic at zero offset and at all offsets on radial traces. For a non-dipping sea floor, the application of NMO using a velocity field equal to the water velocity, will flatten water bottom primary and multiple events. The events will then be periodic in time, on a radial trace and in distance along each radial trace. When a dip is present on the sea floor, in x-t space, the water bottom primary/multiple events are not periodic at any offset in time or on a radial trace in time or radial distance, and simple NMO will not make them periodic.

stationary time series, due to the variable stretch which has been introduced into the record, together with the variation of angle of incidence that each event, on any one trace, has experienced.

However, a straight radial trace transform, following the NMO transform, will map events with constant stretch onto separate traces (this will be demonstrated mathematically later in this chapter). In addition the events on each radial trace will have experienced constant shot emergence angles, incident angle at each bounce within the water layer and receiver incidence angles. In other words the transform pair; NMO with water velocity followed by a straight radial trace transform, will achieve the same preconditioning as a τP transform or a straight radial trace transform alone. However the introduction of a dipping sea floor assigns this transform pair to the same fate as the τP and radial trace transforms, namely that the multiples are no longer periodic (Figures (3.3 c and d)).

The remainder of this chapter will investigate whether this transform pair can be generalised so as to work with dipping sea floors in addition to horizontal sea floors.

To illustrate each transform, a simple split spread synthetic shot record will be used (Figure 3.4). This synthetic has 3 primary events together with their full multiple wave trains. The water bottom primary is located at around 0.4 seconds. A subtle primary is found at around 1.3 seconds and a high amplitude primary at approximately 2.2 seconds.
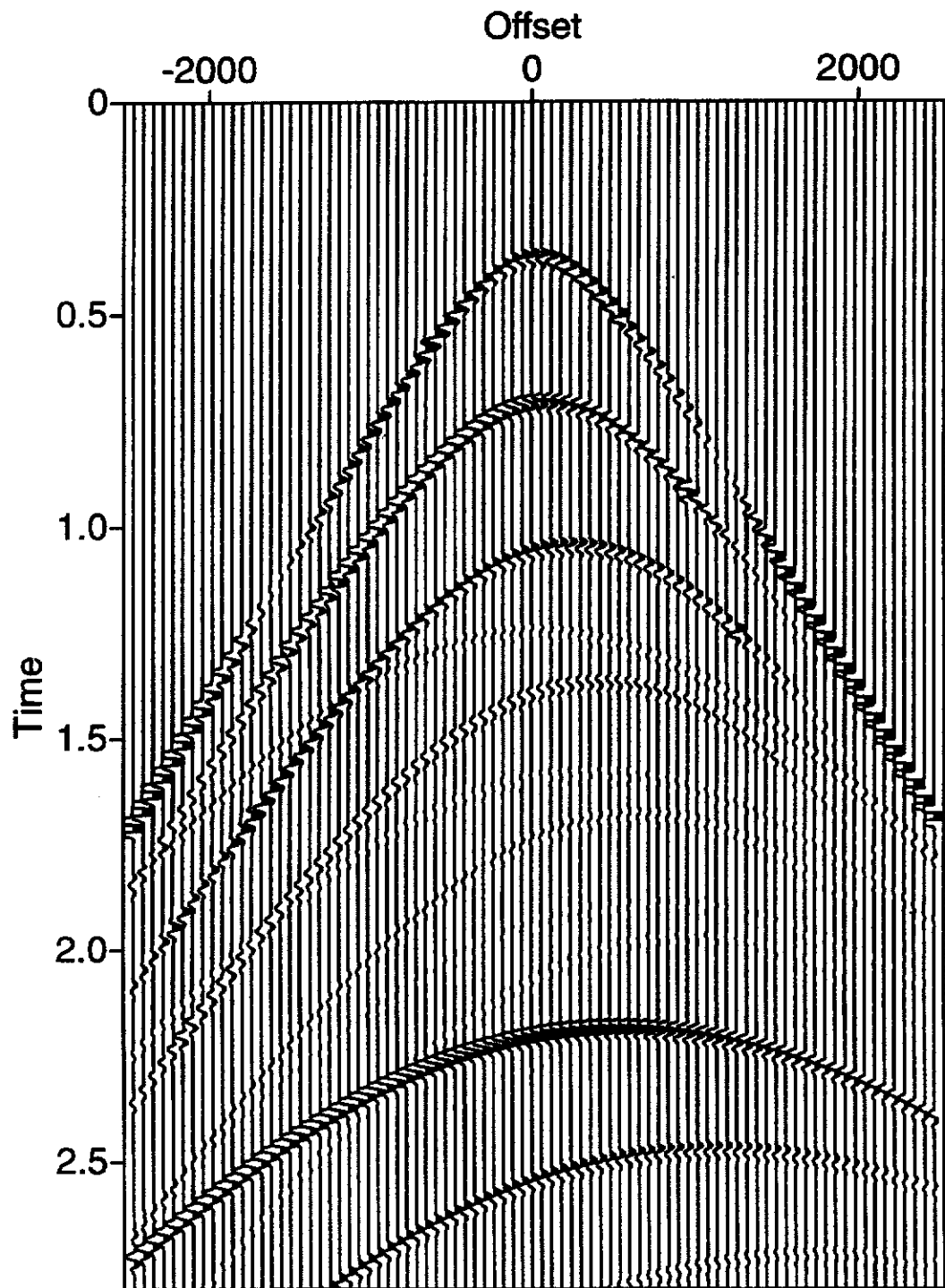
Figure (3.4) A split spread synthetic shot record which is used to demonstrate the new preconditioning transforms.

Three primaries are present with apices at 0.4, 1.3 and 2.2 seconds, together with their full water bottom multiple trains. The sea floor over which the synthetic was modelled has a dip of three degrees.

3.1   Derivation of the generalised NMO equation

As has been discussed, for a horizontal sea floor, NMO applied using water velocity will flatten the water bottom primary/multiple events, and hence render them periodic. This section will investigate whether a more generalised NMO-style equation can be derived which will achieve the same results for a dipping sea floor.

Using the method of images, a circle diagram can be constructed which describes the zero offset times of all orders of water bottom multiples (Figure 3.5).

- α is the dip of the sea floor.

- D is the distance from the surface to the sea floor, normal to the sea floor.

- R is the distance from shot position to where the sea floor would meet the ocean surface.

- Oa is the zero offset distance (two way) for the water bottom primary.

- Ob is the zero offset distance for the first order water bottom multiple.

- Oc is the distance for the second order water bottom multiple.

(Dividing these distances by the water velocity yields the zero offset two way reflection times of the primary and multiple events).

This construction was first published by Born and Wolf (1964) with reference to optics and subsequently by Levin (1971).
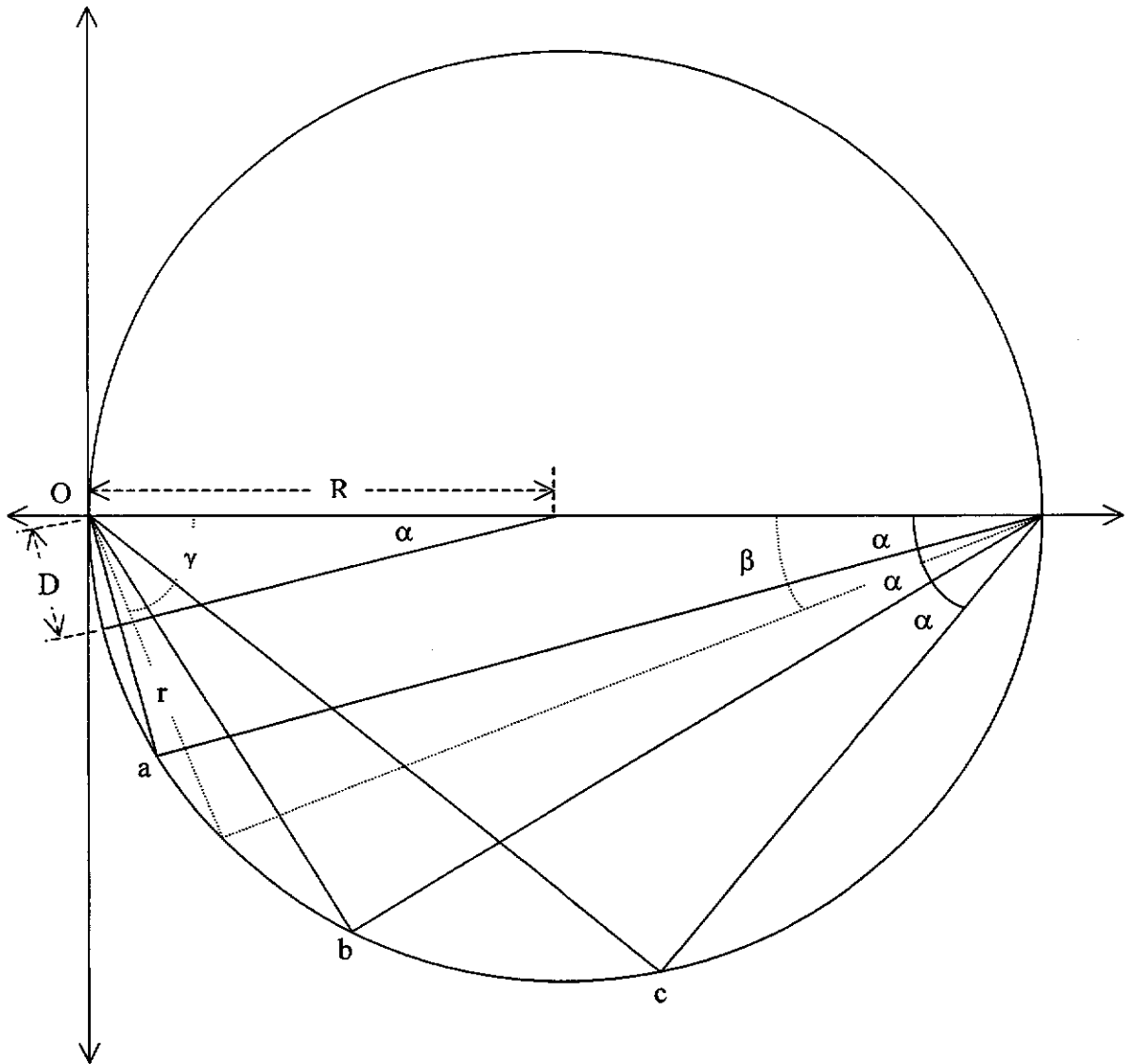
Figure (3.5)   *A circle diagram which is used to derive the zero offset times of the*
               water bottom primary and multiple wave trains.

α *is the dip of the sea floor.* D *is the depth of the sea floor, normal to the sea floor. The zero offset*
distance (two way) for the water bottom primary is Oa. *Likewise* Ob *is the zero offset distance for the*
first order water bottom multiple. Oc *is the distance for the second order water bottom multiple.*
Dividing these distances by the water velocity yeilds the zero offset times of the events. r *is a continuous*
function which describes the zero offset times of all reflection energy which has been trapped in the water
layer. Similarly β *is the continuous apparent dip of the sea floor (after Levin, 1971).*

In addition let r be a continuous function which describes the zero offset times of all reflection energy which has been trapped in the water layer, and β be a continuous variable describing the apparent dip of the sea floor.

The position of the axes in Figure (3.5) (relative to the circle) enables the reduction of the polar equation of a circle to:

$$r = 2.R.\cos(\gamma), \tag{3.1}$$

where

$$R = \frac{D}{\sin(\alpha)}. \tag{3.2}$$

By substituting Equation (3.2) into Equation (3.1) and dividing by the water velocity (v), the following relationships are obtained:

$$\frac{r}{v} = 2.\frac{D}{v}.\frac{\cos(\gamma)}{\sin(\alpha)},$$

$$t_0 = t_{0_p}.\frac{\cos(\gamma)}{\sin(\alpha)}, \tag{3.3}$$

or:

$$= t_{0_p}.\frac{\sin(\beta)}{\sin(\alpha)}, \tag{3.4}$$

where t_0 is the zero offset time and t_{0_p} is the zero offset time of the water bottom primary event. Equation (3.3) is then substituted into the standard dipping layer moveout equation for a shot record to arrive at:

$$t_x^2 = t_0^2 + \frac{x^2}{v^2} - 2.\frac{t_0^2}{t_{0_p}}.\frac{x}{v}.\sin \alpha. \tag{3.5}$$

This equation forms the basis of a procedure to flatten the primary and water bottom multiple events (for shot records). However, because the zero offset times are not periodic for a dipping sea floor, simply flattening the water bottom primary and multiple events does not make them periodic. It is therefore necessary to substitute an expression for t_0 which will make the zero offset times periodic.

When $\beta = 2.\alpha$ it is necessary to convert t_0 to $2.t_{0_p}$. Likewise when $\beta = 3.\alpha$ it is necessary to convert t_0 to $3.t_{0_p}$ and so forth. Using Equation (3.4) it can be seen that what is needed is a function (T), which satisfies the following equations:

$$2.t_{0_p}.T = t_{0_p}.\frac{\sin(2.\psi)}{\sin\psi},$$

$$3.t_{0_p}.T = t_{0_p}.\frac{\sin(3.\psi)}{\sin\psi},$$

etc.

These equations are of the form:

$$\frac{\beta}{\alpha}.T = \frac{\sin\beta}{\sin\alpha}. \tag{3.6}$$

By rearranging Equation (3.4) the following relationship can be established:

$$\beta = \sin^{-1}\left(\sin(\alpha).\frac{t_0}{t_{0_p}}\right). \tag{3.7}$$

Then by substituting Equation (3.7) into Equation (3.6) we get:

$$T = \frac{\alpha}{\sin^{-1}\left(\sin(\alpha)\dfrac{t_0}{t_{0_P}}\right)} \cdot \frac{t_0}{t_{0_P}}. \tag{3.8}$$

T was designed so that:

$$t_{0_{periodic}}.T = t_0, \tag{3.9}$$

where $t_{0_{periodic}}$ is a stretched version of t_0, so that the zero offset water bottom multiples are now periodic with a period equal to t_{0_P}. By substituting Equation (3.8) into

Equation (3.9) and rearranging we get:

$$t_{0_{periodic}} \cdot \frac{\alpha}{\sin^{-1}\left(\sin(\alpha)\dfrac{t_0}{t_{0_P}}\right)} \cdot \frac{t_0}{t_{0_P}} = t_0,$$

$$\sin^{-1}\left(\sin(\alpha)\frac{t_0}{t_{0_P}}\right) = \alpha.\frac{t_{0_{periodic}}}{t_{0_P}},$$

$$t_0 = t_{0_P}.\frac{\sin\left(\alpha.\dfrac{t_{0_{periodic}}}{t_{0_P}}\right)}{\sin\alpha}. \tag{3.10}$$

Finally we substitute Equation (3.10) into Equation (3.5) to arrive at:

$$t_x^2 = \left(t_{0_P}.\frac{\sin\left(\alpha.\dfrac{t_{0_{periodic}}}{t_{0_P}}\right)}{\sin\alpha}\right)^2 + \frac{x^2}{v^2} - 2.t_{0_P}.\frac{\sin^2\left(\alpha.\dfrac{t_{0_{periodic}}}{t_{0_P}}\right)}{\sin\alpha}.\frac{x}{v}. \tag{3.11}$$

When $t_{0_{periodic}}$ is equal to an integer (n) times t_{0_P}, Equation (3.11) is the travel time equation

for the water bottom events. For example, when n=1, it describes the travel times for the

water bottom primary. When n=2, it describes the travel times for the first order water bottom multiple and so forth.

Equation (3.11) needs to be rearranged to yield the transform equation;

$$t_x^2 = \frac{t_{0_p}^2 \sin^2\left(\frac{t_{0_{periodic}}}{t_{0_p}}.\alpha\right)}{\sin^2\alpha} + \frac{x^2}{v^2} - 2.\frac{x}{v}.t_{0_p}.\frac{\sin^2\left(\frac{t_{0_{periodic}}}{t_{0_p}}.\alpha\right)}{\sin\alpha},$$

$$t_x^2 = \sin^2\left(\frac{t_{0_{periodic}}}{t_{0_p}}.\alpha\right)\left(\frac{t_{0_p}^2}{\sin^2\alpha} - 2.\frac{x}{v}.\frac{t_{0_p}}{\sin\alpha}\right) + \frac{x^2}{v^2},$$

$$\sin^2\left(\frac{t_{0_{periodic}}}{t_{0_p}}.\alpha\right) = \frac{t_x^2 - \frac{x^2}{v^2}}{\frac{t_{0_p}^2}{\sin^2\alpha} - 2.\frac{x}{v}.\frac{t_{0_p}}{\sin\alpha}},$$

$$t_{0_{periodic}} = \frac{t_{0_p}}{\alpha}\sin^{-1}\sqrt{\frac{t_x^2 - \frac{x^2}{v^2}}{\frac{t_{0_p}^2}{\sin^2\alpha} - 2.\frac{x}{v}.\frac{t_{0_p}}{\sin\alpha}}}. \qquad (3.12)$$

Equation (3.12) is a continuous transform which will flatten the water bottom primary event, and make the simple water bottom multiples periodic with this flattened primary. It is therefore the generalised NMO equation, for a dipping sea floor, which we have been seeking. This transform has been called Multiple MoveOut (MMO). This has been the derivation of the MMO Equation for a shot record.

Figure (3.6) shows the result of the application of the MMO transform to the data in Figure (3.4). The primary event is now flat and the water bottom multiples are periodic with the primary (due to the minimum phase wavelets, the onset of the wavelet is flat and periodic). The second and third primary events have been overcorrected along with their respective water bottom multiple trains (water bottom pegleg multiples). These pegleg water bottom multiple sequences are approximately periodic also.

The corresponding MMO equation for CMP gathers can be simply derived starting with the dipping CMP NMO equation:

$$t_x^2 = t_0^2 + \frac{x^2}{v^2}\cos^2(\beta),$$ (3.13)

From Equations (3.4) and (3.10) it is evident that:

$$\beta = \frac{\alpha t_{0_{periodic}}}{t_{0_p}}.$$ (3.14)

Substitute Equations (3.10) and (3.14) into (3.13) to obtain:

$$t_x^2 = \left(t_{0_p} \cdot \frac{\sin\left(\frac{\alpha t_{0_{periodic}}}{t_{0_p}}\right)}{\sin(\alpha)} \right)^2 + \frac{x^2}{v^2}.\cos^2\left(\frac{\alpha t_{0_{periodic}}}{t_{0_p}}\right).$$ (3.15)
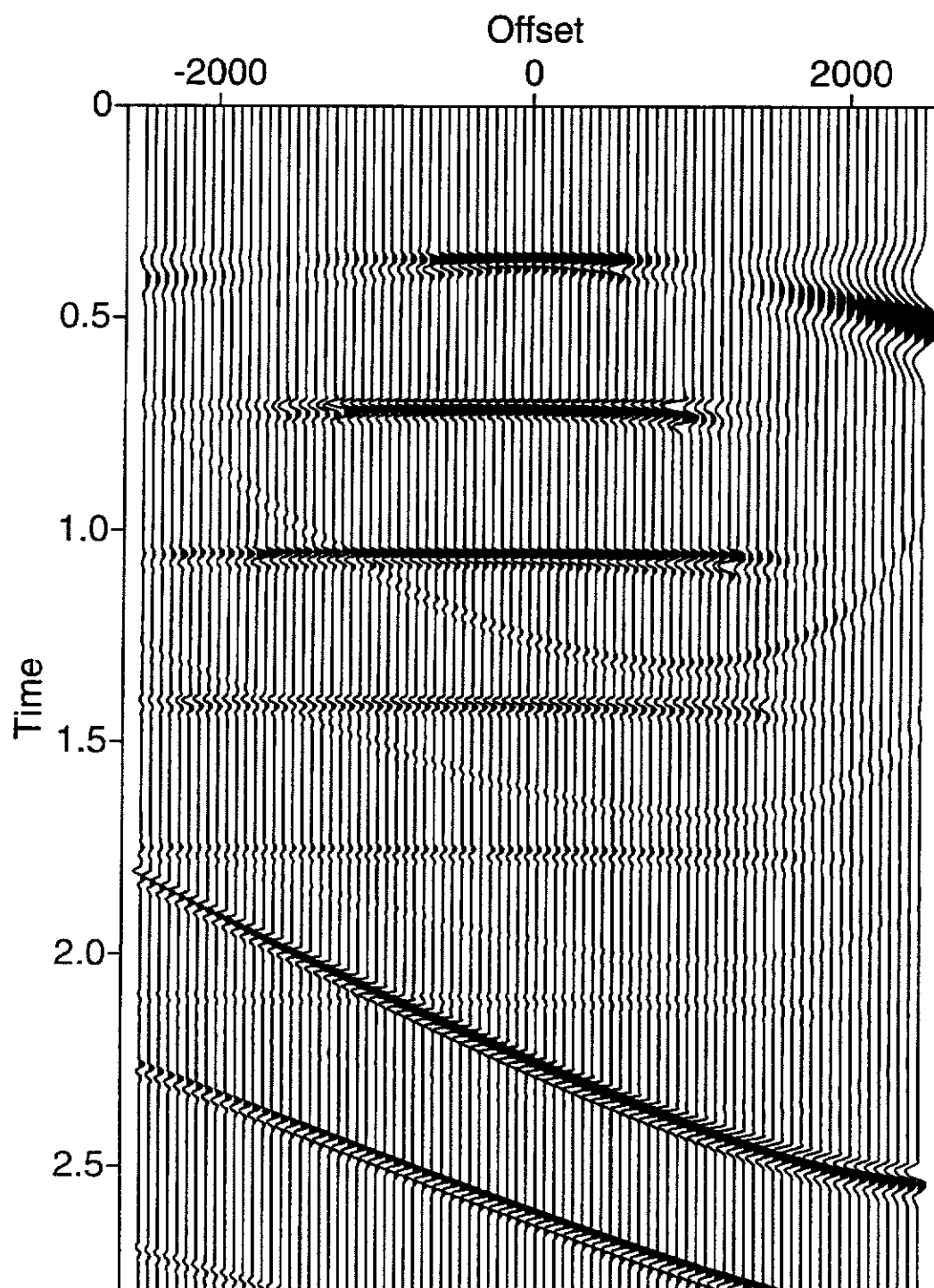
Figure (3.6) **The synthetic shot record after the application of MMO.**
Although masked by the phase changes of the events with offset and the introduced stretch, the simple water bottom multiples are now flat and periodic while the water bottom peg leg multiples are approximately periodic.

Equation (3.15) is the travel time equation for the water bottom related events (primary plus simple multiples) for a CMP gather. Once again we rearrange this equation to obtain the MMO equation;

$$= \left(t_{0_p} \cdot \frac{\sin\left(\frac{\alpha t_{0_{periodic}}}{t_{0_p}}\right)}{\sin(\alpha)} \right)^2 + \frac{x^2}{v^2}\left(1 - \sin^2\left(\frac{\alpha t_{0_{periodic}}}{t_{0_p}}\right)\right),$$

$$= \left(t_{0_p} \cdot \frac{\sin\left(\frac{\alpha t_{0_{periodic}}}{t_{0_p}}\right)}{\sin(\alpha)} \right)^2 + \frac{x^2}{v^2} - \frac{x^2}{v^2}\sin^2\left(\frac{\alpha t_{0_{periodic}}}{t_{0_p}}\right),$$

$$= \sin^2\left(\frac{\alpha t_{0_{periodic}}}{t_{0_p}}\right)\left(\frac{t_{0_p}^2}{\sin^2(\alpha)} - \frac{x^2}{v^2}\right) + \frac{x^2}{v^2},$$

$$\sin^2\left(\frac{\alpha t_{0_{periodic}}}{t_{0_p}}\right) = \frac{t_x^2 - \frac{x^2}{v^2}}{\frac{t_{0_p}^2}{\sin^2(\alpha)} - \frac{x^2}{v^2}},$$

$$t_{0_{periodic}} = \frac{t_{0_p}}{\alpha} \cdot \sin^{-1}\sqrt{\frac{t_x^2 - \frac{x^2}{v^2}}{\frac{t_{0_p}^2}{\sin^2(\alpha)} - \frac{x^2}{v^2}}}. \qquad (3.16)$$

This is the CMP MMO Equation.

At first glance Equations (3.11) and (3.15) do not appear to reduce to the non-dipping equation when $\alpha = 0$ (naturally the travel time equation is the same for both CMP and

shot gathers for a 1D earth). By using Taylor Series expansions it can be shown that they do. Two parts of these MMO Equations can be dealt with separately initially. These are:

$$\frac{\sin^2\left(\dfrac{\alpha t_{0_{periodic}}}{t_{0_p}}\right)}{\sin^2(\alpha)},$$

(3.17)

and

$$\frac{\sin^2\left(\dfrac{\alpha\, t_{0_{periodic}}}{t_{0_p}}\right)}{\sin(\alpha)}.$$

(3.18)

Starting with Equation (3.17):

$$\frac{\sin^2\left(\dfrac{\alpha t_{0_{periodic}}}{t_{0_p}}\right)}{\sin^2(\alpha)} = \frac{\left(\dfrac{\alpha t_{0_{periodic}}}{t_{0_p}} - \dfrac{\alpha^3 t_{0_{periodic}}^{\;3}}{t_{0_p}^{\;3} 3!} + \dfrac{\alpha^5 t_{0_{periodic}}^{\;5}}{t_{0_p}^{\;5} 5!} \cdots\right)^2}{\left(\alpha - \dfrac{\alpha^3}{3!} + \dfrac{\alpha^5}{5!} \cdots\right)^2},$$

$$= \frac{t_{0_{periodic}}^{\;2}}{t_{0_p}^{\;2}} \cdot \frac{\left(1 - \dfrac{\alpha^2 t_{0_{periodic}}^{\;2}}{t_{0_p}^{\;2} 3!} + \dfrac{\alpha^4 t_{0_{periodic}}^{\;4}}{t_{0_p}^{\;4} 5!} \cdots\right)^2}{\left(1 - \dfrac{\alpha^2}{3!} + \dfrac{\alpha^4}{5!} \cdots\right)^2},$$

which as $\alpha \to 0$:

$$= \frac{t_{0_{periodic}}^{\;2}}{t_{0_p}^{\;2}},$$

$$= 1,$$

because t_0 equals $t_{0_{periodic}}$ for $\alpha \to 0$.

Secondly with Equation (3.18):

$$\frac{\sin^2\left(\dfrac{\alpha t_{0_{periodic}}}{t_{0_p}}\right)}{\sin(\alpha)} = \frac{\left(\dfrac{\alpha t_{0_{periodic}}}{t_{0_p}} - \dfrac{\alpha^3 t_{0_{periodic}}^3}{t_{0_p}^3 3!} + \dfrac{\alpha^5 t_{0_{periodic}}^5}{t_{0_p}^5 5!}....\right)^2}{\left(\alpha - \dfrac{\alpha^3}{3!} + \dfrac{\alpha^5}{5!}....\right)},$$

$$= \frac{\alpha t_{0_{periodic}}^2}{t_{0_p}^2} \cdot \frac{\left(1 - \dfrac{\alpha^2 t_{0_{periodic}}^2}{t_{0_p}^2 3!} + \dfrac{\alpha^4 t_{0_{periodic}}^4}{t_{0_p}^4 5!}....\right)}{\left(1 - \dfrac{\alpha^2}{3!} + \dfrac{\alpha^4}{5!}....\right)^2},$$

which as $\alpha \to 0$:

$$= 0.$$

Therefore as $\alpha \to 0$ the shot record travel time equation (Equation 3.11) becomes:

$$t_x^2 = t_0^2 + \frac{x^2}{v^2}, \tag{3.19}$$

which is the non-dipping NMO equation. Likewise the CMP travel time equation (Equation 3.15) reduces to Equation (3.19).

After application of the MMO Equation, in either shot or CMP domain, the water bottom primary and multiple events become periodic. However differential stretch occurs down each trace. Also there is a change of angle of incidence for each reflection event (and hence a likely change in wavelet shape). In a similar manner to the non-dipping solution, these two problems can be solved by mapping the data onto radial type trajectories, which follow the introduced stretch patterns through the data. An obvious name for a transform, which follows trajectories of constant stretch, is an IsoStretch Radial trace transform (the ISR transform).

3.2   Derivation of the ISR transform.

The first step in the derivation of the ISR transform is to develop an equation to describe the stretch, which is introduced, by the MMO equation. Firstly the non-dipping stretch function will be derived. Starting with the NMO equation:

$$t_0^2 = t_x^2 - \frac{x^2}{v^2},$$

$$t_0 = \sqrt{t_x^2 - \frac{x^2}{v^2}},$$

$$= \Im(t_x)$$
(3.20)

Let

$$t_x + dt = \overline{t_x},$$

and

$$\Im(t_x + dt) = \overline{t_0}.$$

Stretch is the ratio of a small change in t_0 to the corresponding change in t_x:

$$Stretch = \frac{\overline{t_0} - t_0}{\overline{t_x} - t_x},$$

$$= \frac{\Im(t_x + dt) - \Im(t_x)}{t_x + dt - t_x},$$

$$= \frac{\Im(t_x + dt) - \Im(t_x)}{dt},$$

$$= \frac{d\Im(t_x)}{dt_x}.$$
(3.21)

Therefore by differentiating Equation (3.20) the Stretch Function can be obtained:

$$Stretch = \frac{t_x}{\left(t_x^2 - \frac{x^2}{v^2}\right)^{\frac{1}{2}}},$$

$$= \frac{t_x}{t_0}. \tag{3.22}$$

So for the non-dipping case, Equation (3.22) describes a set of lines, which run through the origin and fan out through the data (an equation for each line is found by letting "Stretch" in Equation (3.22) equal a constant).

In order to calculate stretch in the non-dipping case it is necessary to use the chain rule:

$$\frac{dt_0}{dt_x} = \frac{dt_0}{dt_{0_{periodic}}} \cdot \frac{dt_{0_{periodic}}}{dt_x}. \tag{3.23}$$

For both the shot record and CMP gather we start with Equation (3.10) from which, $\frac{dt_0}{dt_{0_{periodic}}}$ can be determined:

$$t_0 = t_{0_p} \cdot \frac{\sin\left(\frac{t_{0_{periodic}}}{t_{0_p}} \cdot \alpha\right)}{\sin \alpha},$$

$$\frac{dt_0}{dt_{0_{periodic}}} = \frac{t_{0_p}}{\sin \alpha} \cdot \cos\left(\frac{t_{0_{periodic}}}{t_{0_p}} \cdot \alpha\right) \cdot \frac{\alpha}{t_{0_p}},$$

$$= \frac{\alpha}{\sin \alpha} \cdot \cos\left(\frac{t_{0_{periodic}}}{t_{0_p}} \cdot \alpha\right). \tag{3.24}$$

Finally by differentiating $t_{0_{periodic}}$ with respect to t_x for a shot record (Equation 3.12);

$$\frac{dt_{0_{periodic}}}{dt_x} = \frac{t_{0_p}}{\alpha} \cdot \frac{1}{\sqrt{1 - \frac{t_x^2 - \frac{x^2}{v^2}}{\frac{t_{0_p}^2}{\sin^2\alpha} - 2 \cdot \frac{x}{v} \cdot \frac{t_{0_p}}{\sin\alpha}}}} \cdot \frac{1}{2} \cdot \frac{1}{\sqrt{\frac{t_x^2 - \frac{x^2}{v^2}}{\frac{t_{0_p}^2}{\sin^2\alpha} - 2 \cdot \frac{x}{v} \cdot \frac{t_{0_p}}{\sin\alpha}}}} \cdot \frac{2t_x}{\frac{t_{0_p}^2}{\sin^2\alpha} - 2 \cdot \frac{x}{v} \cdot \frac{t_{0_p}}{\sin\alpha}},$$

$$= \frac{t_{0_p}}{\alpha} \cdot \sqrt{\frac{\frac{t_{0_p}^2}{\sin^2\alpha} - 2 \cdot \frac{x}{v} \cdot \frac{t_{0_p}}{\sin\alpha}}{\frac{t_{0_p}^2}{\sin^2\alpha} - 2 \cdot \frac{x}{v} \cdot \frac{t_{0_p}}{\sin\alpha} - t_x^2 + \frac{x^2}{v^2}}} \cdot \sqrt{\frac{\frac{t_{0_p}^2}{\sin^2\alpha} - 2 \cdot \frac{x}{v} \cdot \frac{t_{0_p}}{\sin\alpha}}{t_x^2 - \frac{x^2}{v^2}}} \cdot \frac{t_x}{\frac{t_{0_p}^2}{\sin^2\alpha} - 2 \cdot \frac{x}{v} \cdot \frac{t_{0_p}}{\sin\alpha}},$$

$$= \frac{t_x t_{0_p}}{\alpha \sqrt{\left(\frac{t_{0_p}^2}{\sin^2\alpha} - 2 \cdot \frac{x}{v} \cdot \frac{t_{0_p}}{\sin\alpha} - t_x^2 + \frac{x^2}{v^2}\right)\left(t_x^2 - \frac{x^2}{v^2}\right)}}. \qquad (3.25)$$

Therefore by combining Equation (3.24) and (3.25) using Equation (3.21) the stretch function can be derived:

$$Stretch = \frac{dt_0}{dt_x} = \frac{dt_0}{dt_{0_{periodic}}} \cdot \frac{dt_{0_{periodic}}}{dt_x},$$

$$= \frac{\alpha}{\sin(\alpha)} \cdot \cos\left(\frac{t_{0_{periodic}}}{t_{0_p}} \cdot \alpha\right) \cdot \frac{t_x t_{0_p}}{\alpha \sqrt{\left(\frac{t_{0_p}^2}{\sin^2\alpha} - 2 \cdot \frac{x}{v} \cdot \frac{t_{0_p}}{\sin\alpha} - t_x^2 + \frac{x^2}{v^2}\right)\left(t_x^2 - \frac{x^2}{v^2}\right)}},$$

$$= \frac{t_x}{\sqrt{t_x^2 - \frac{x^2}{v^2}}} \cdot \cos\left(\frac{t_{0_{periodic}}}{t_{0_p}} \cdot \alpha\right) \cdot \frac{t_{0_p} \cdot v}{\sqrt{v^2 t_{0_p}^2 - 2 \cdot x \cdot v \cdot \sin(\alpha) t_{0_p} - t_x^2 \cdot v^2 \cdot \sin^2(\alpha) + x^2 \cdot \sin^2(\alpha)}},$$

$$= \frac{t_x}{\sqrt{t_x^2 - \frac{x^2}{v^2}}} . \cos\left(\frac{t_{0_{periodic}}}{t_{0_p}} . \alpha\right) \frac{t_{0_p} . v}{\sqrt{\left(v.t_{0_p} - x.\sin(\alpha)\right)^2 - t_x^2 . v^2 . \sin^2(\alpha)}} . \qquad (3.26)$$

This equation is the ISR equation for a shot record with a dipping sea floor. When there is no dip on the sea floor, Equation (3.26) becomes:

$$= \frac{t_x}{t_0} . 1 . \frac{t_{0_p} . v}{\sqrt{v^2 . t_{0_p}^2}} ,$$

$$= \frac{t_x}{t_0} ,$$

which is the ISR equation for a non-dipping sea floor (Equation 3.22).

Once again the chain rule is used to derive the stretch function for the CMP domain. $\frac{dt_0}{dt_{0_{periodic}}}$ is the same as calculated for the shot record.

In order to determine $\frac{dt_{0_{periodic}}}{dt_x}$ for a CMP gather we differentiate Equation (3.16):

$$\frac{dt_{0_{periodic}}}{dt_x} = \frac{t_{0_p}}{\alpha} . \frac{1}{\sqrt{1 - \frac{t_x^2 - \frac{x^2}{v^2}}{\frac{t_{0_p}^2}{\sin^2\alpha} - \frac{x^2}{v^2}}}} . \frac{1}{2} . \frac{1}{\sqrt{\frac{t_x^2 - \frac{x^2}{v^2}}{\frac{t_{0_p}^2}{\sin^2\alpha} - \frac{x^2}{v^2}}}} . \frac{2t_x}{\frac{t_{0_p}^2}{\sin^2\alpha} - \frac{x^2}{v^2}} ,$$

$$= \frac{t_{0_p}}{\alpha} \cdot \sqrt{\frac{\dfrac{t_{0_p}^{~2}}{\sin^2 \alpha} - \dfrac{x^2}{v^2}}{\dfrac{t_{0_p}^{~2}}{\sin^2 \alpha} - \dfrac{x^2}{v^2} - t_x^{~2} + \dfrac{x^2}{v^2}}} \cdot \sqrt{\frac{\dfrac{t_{0_p}^{~2}}{\sin^2 \alpha} - \dfrac{x^2}{v^2}}{t_x^{~2} - \dfrac{x^2}{v^2}}} \cdot \frac{t_x}{\dfrac{t_{0_p}^{~2}}{\sin^2 \alpha} - \dfrac{x^2}{v^2}},$$

$$= \frac{t_x t_{0_p}}{\alpha \sqrt{\left(\dfrac{t_{0_p}^{~2}}{\sin^2 \alpha} - t_x^{~2}\right)\left(t_x^{~2} - \dfrac{x^2}{v^2}\right)}},$$

$$= \frac{t_x . t_{0_p} . \sin(\alpha)}{\alpha \sqrt{\left(t_{0_p}^{~2} - t_x^{~2} . \sin^2(\alpha)\right)\left(t_x^{~2} - \dfrac{x^2}{v^2}\right)}}. \qquad (3.27)$$

Therefore by combining Equations (3.22) and (3.27) using Equation (3.16) the dipping stretch function for the CMP domain can be derived:

$$\text{Stretch} = \frac{\alpha}{\sin(\alpha)} . \cos\left(\frac{t_{0_{periodic}}}{t_{0_p}} . \alpha\right) . \frac{t_x . t_{0_p} . \sin(\alpha)}{\alpha \sqrt{\left(t_{0_p}^{~2} - t_x^{~2} . \sin^2(\alpha)\right)\left(t_x^{~2} - \dfrac{x^2}{v^2}\right)}},$$

$$= \cos\left(\frac{t_{0_{periodic}}}{t_{0_p}} . \alpha\right) . \frac{t_x . t_{0_p}}{\sqrt{\left(t_{0_p}^{~2} - t_x^{~2} . \sin^2(\alpha)\right)\left(t_x^{~2} - \dfrac{x^2}{v^2}\right)}}. \qquad (3.28)$$

For a non-dipping sea floor Equation (3.28) reduces to:

$$\frac{t_x}{t_0},$$

which is once again the non-dipping stretch function.

The application of ISR to the synthetic shot record of Figure (3.6) is demonstrated in Figure (3.7). In addition to mapping constant stretch on each trace, ISR traces will also exactly map shot emergence angles (Hartley (1998); Hartley and Lamont (1996)). This can be clearly seen by the location of the critical angle reflection events in Figure (3.7). In the case of a horizontal sea floor, the angle of shot emergence, the incidence angle of each reflection in the water layer, as well as receiver incidence angle, are all the same on each trace. Therefore after this transform the water bottom primary and multiple trains will be periodic and have similar wavelet shapes and hence should form stationary time series on each trace.

The water bottom peg leg multiples approximately form a stationary time series. This claim is based on observation of synthetics and field datasets before and after transforms. It is not theoretically substantiated or quantified in this thesis. It is analogous to the preconditioning of water bottom pegleg multiples using the τP transform.

Hence, following the transforms, each trace resembles a zero offset trace recorded over a 1D earth. All multiples are thereby well prepared by the MMO and ISR transforms, for their attenuation by either predictive deconvolution or autoconvolution.
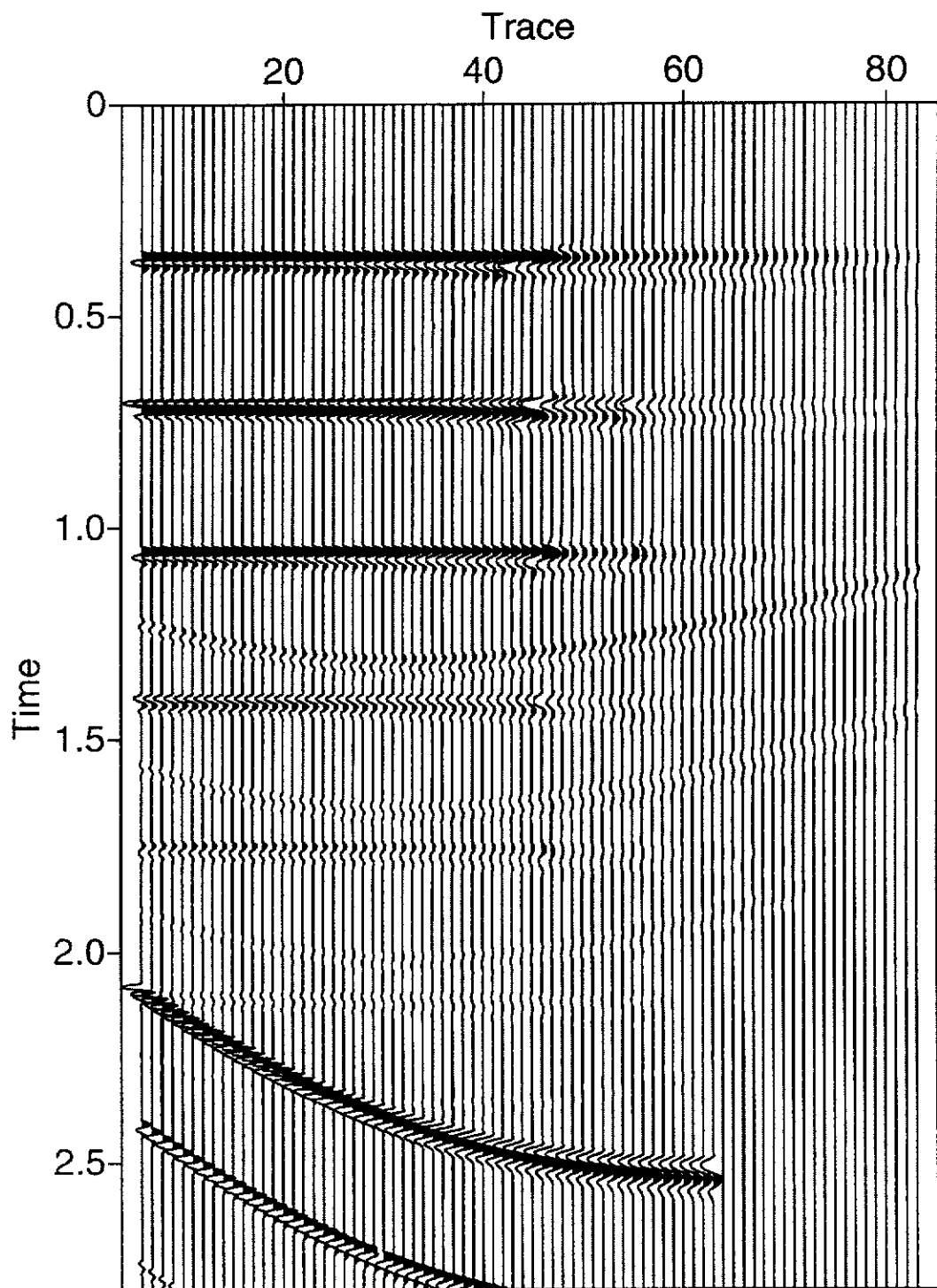
Figure (3.7) The synthetic shot record after application of MMO and ISR.
The wavelets on each trace now form a stationary time series.

3.3   Implementation of the MMO and ISR transforms

Only the shot record forms of the MMO/ISR transforms have been implemented. Typically CMP gathers have four times the trace spacing that shot records have. It is therefore more accurate to interpolate shot records spatially (during the formation of the radial traces). For this reason the shot domain will always be a better place to perform this type of operation and hence was chosen for the initial implementation of the transforms.

An assumption of the MMO and ISR transform procedure is that the sea floor is linear and geologically consistent over the spread length. If we were dealing with primary reflection data, then the CMP domain would offer the advantage of the sea floor reflection points being focussed over a small area of the sea floor (not the entire spread length). However, the reflection points for multiples are spread out, especially for higher order multiples, and hence the advantage is actually not as great as it might seem. Likewise for the shot record, the average dip along most of the spread length is required and not only over the front half of the cable, as would be the case if only primary reflection data were being considered.

The source code (in the C language) for the MMO, ISR and autoconvolution routines was written by the author of this thesis, as modules for the Colorado School of Mines free seismic processing package (Seismic Unix : SU).

The MMO transform is implemented in a very similar manner to an NMO transform. The MMO transformation is a single trace operation. A trace is brought into the program,

MMO applied, the trace is then output and a new trace brought in and so forth. Using Equation (3.12), each sample in the MMO domain is calculated using 8 point sinc interpolation. The input parameters are the dip of the sea floor, t_{0_p} and the water velocity. These parameters are read from the trace headers (the derivation of these parameters is discussed in Chapter 4). The inverse MMO transform is accomplished using Equation (3.11).

The ISR transform is a more complex multichannel program than the MMO program. In addition to the parameters required for the MMO program, ISR requires a reconstructed split spread shot record to be input, along with the information required to position the ISR traces correctly. This information is input from the command line. Split spread shot records are reconstructed for marine surveys by invoking source-receiver reciprocity.

The ISR process commences by inputting a full shot record. The stretch values required for each specified ISR trace location are then calculated using Equation (3.25). The required offsets (x), to form each of the output ISR traces are then calculated using Equation (3.25), rearranged so that it is explicit in x. Four point LaGrangian interpolation is then used to form the ISR traces; this type of interpolation being able to cope with irregularly spaced traces. The ISR traces are then output. The process continues by reading in a new shot record and so on. The inverse ISR transform is accomplished using Equation (3.25) directly after processing in the transform domain is complete.

So far four-point interpolation applied across traces for a constant time (or sample) value has been found to be adequate. Figure (3.8) shows the shot record from Figure (3.4) after

it has undergone the forward MMO and ISR transforms followed by their inverse transforms. A comparison of Figures (3.4) and (3.8) shows that apart from the apparent mute which has been applied (by the extent of the radial traces), visually, the two are identical, verifying the integrity of the transforms. The processor chooses the position of the mutes. They can have effectively no mute by having the ISR traces cover almost 180 degrees. This does lead to the first and last ISR traces being short in time.

The inverse ISR transform uses the same techniques as the forward transform, utilising Equation (3.25) directly. All of the original trace header information is stored so that the inverse transformation recovers the original traces which were input to the forward transform.
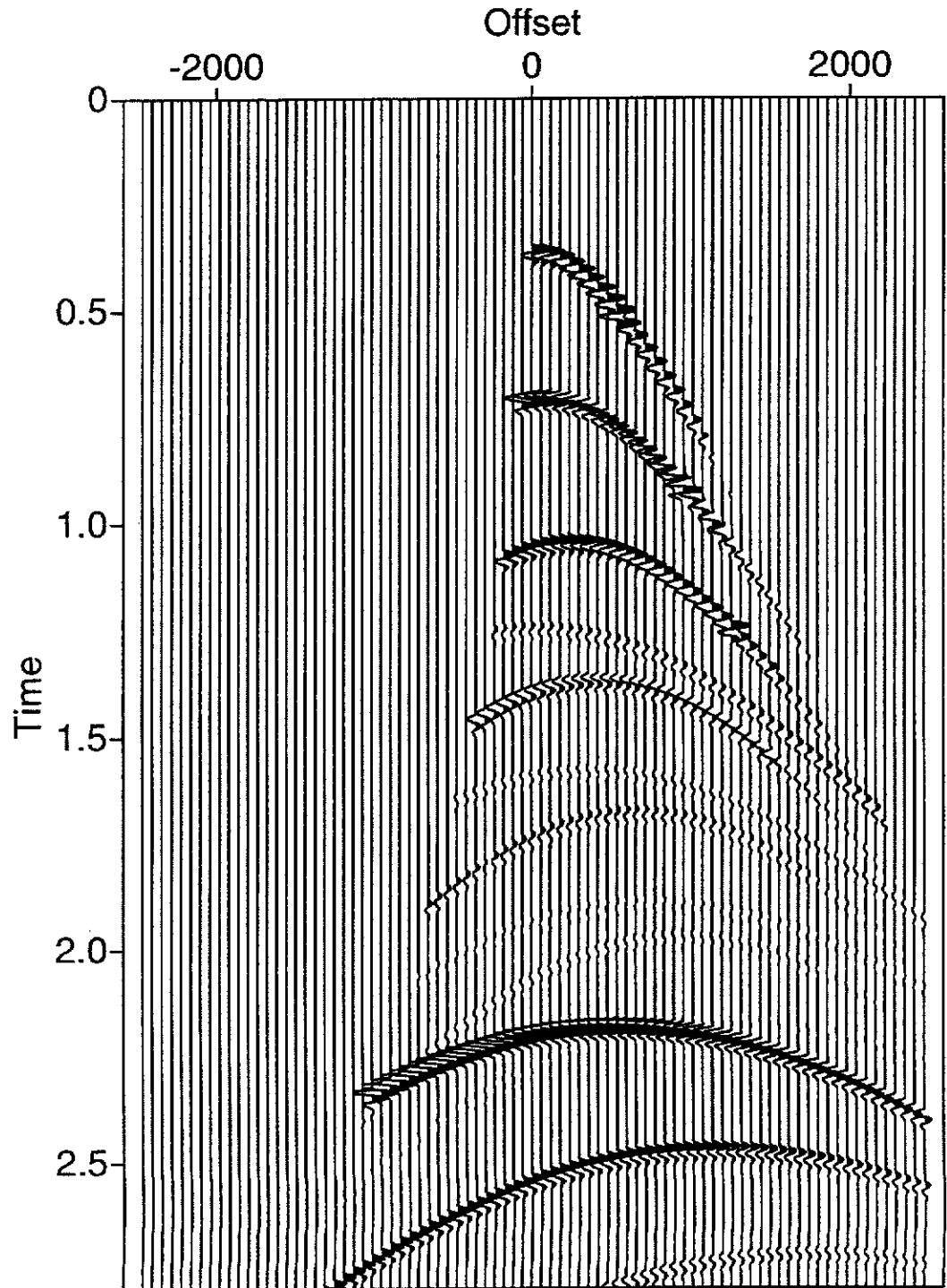
Figure (3.8) *The synthetic record after application of the forward MMO and ISR transformations followed by the inverse transforms.*

Notice that there is no visual difference (besides the "mute") between this record and the original record in Figure (3.4).

3.4   Multiple attenuation in the transform space

If the period of the multiples in the transform domain is less than 400 milliseconds (msec), predictive deconvolution is a very suitable tool for attenuating the multiples. If the period is over 400 msec, as a rule of thumb, then autoconvolution is probably a better choice.

The problem with gapped deconvolution for longer period multiples is in the design of the filters. It has been found best to have at least 3 occurrences of the multiples within the active filter length. Therefore for a 400 msec period, the filter needs to be at least 1000 msec long. It is also a good rule of thumb to have the design windows ten times the length of the filter, with five times the length as a minimum. With the data preconditioned with the MMO/ISR combination, the full trace length can be used to design the filters because of the stationarity of the primary/multiple wave trains created by the transforms. Therefore, with the typical data length being 6 seconds, 6 times the length of a 1000 msec filter, it is evident that attenuation of multiples with a period greater than 400 msecs should not be attempted.

Figure (3.9) shows the results of the application of predictive deconvolution in the MMO and ISR transform domain when applied to the synthetic test data set shown in Figure (3.4). Note that the majority of multiple energy has been removed, and at least as importantly, the primary events have been preserved. Figure (3.10) shows the data after transformation back to the x-t domain.
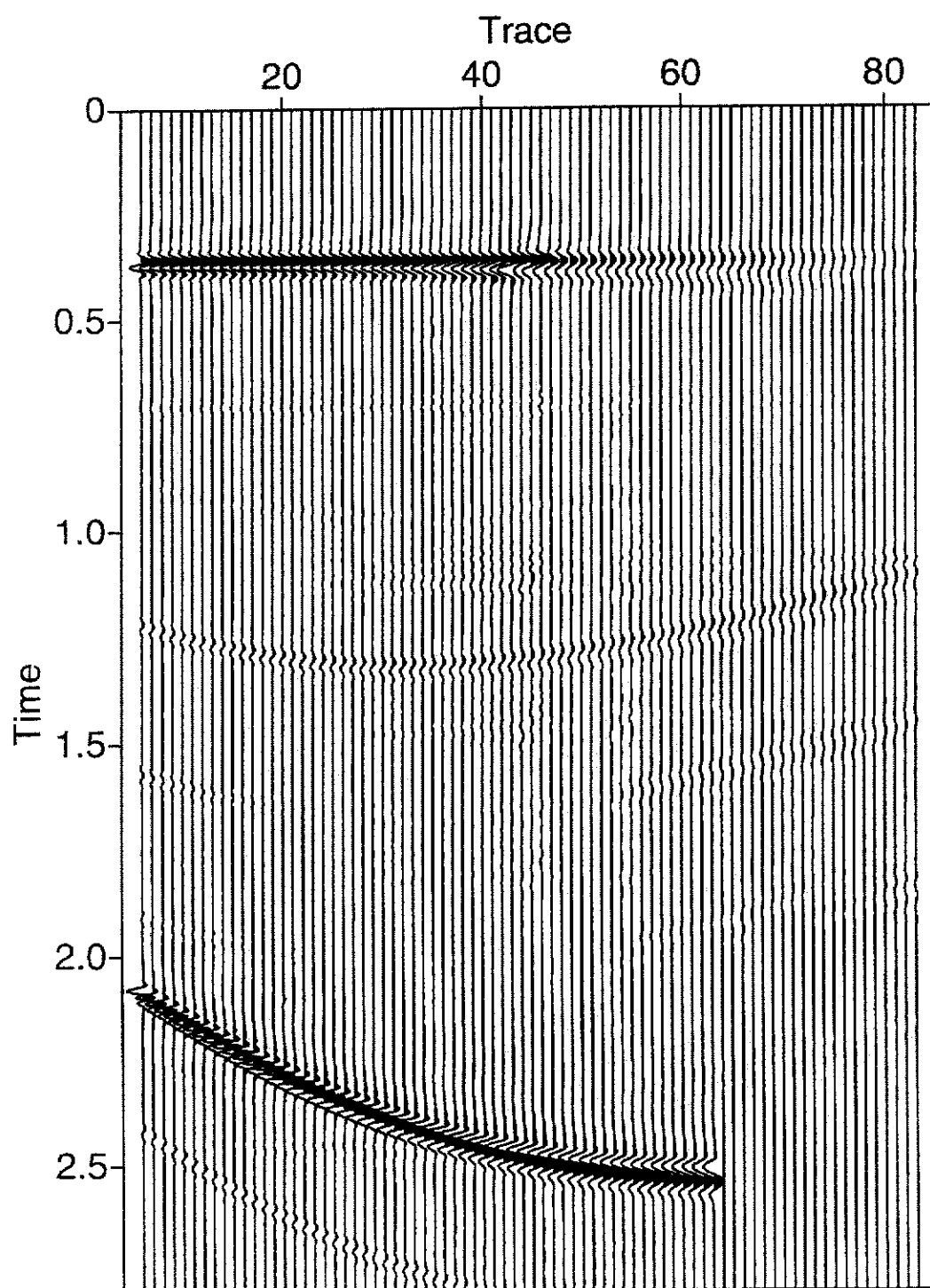
Figure (3.9) The synthetic record after the application of predictive deconvolution in the transform domain.

Notice that the majority of multiple energy has been removed and the primary events preserved.
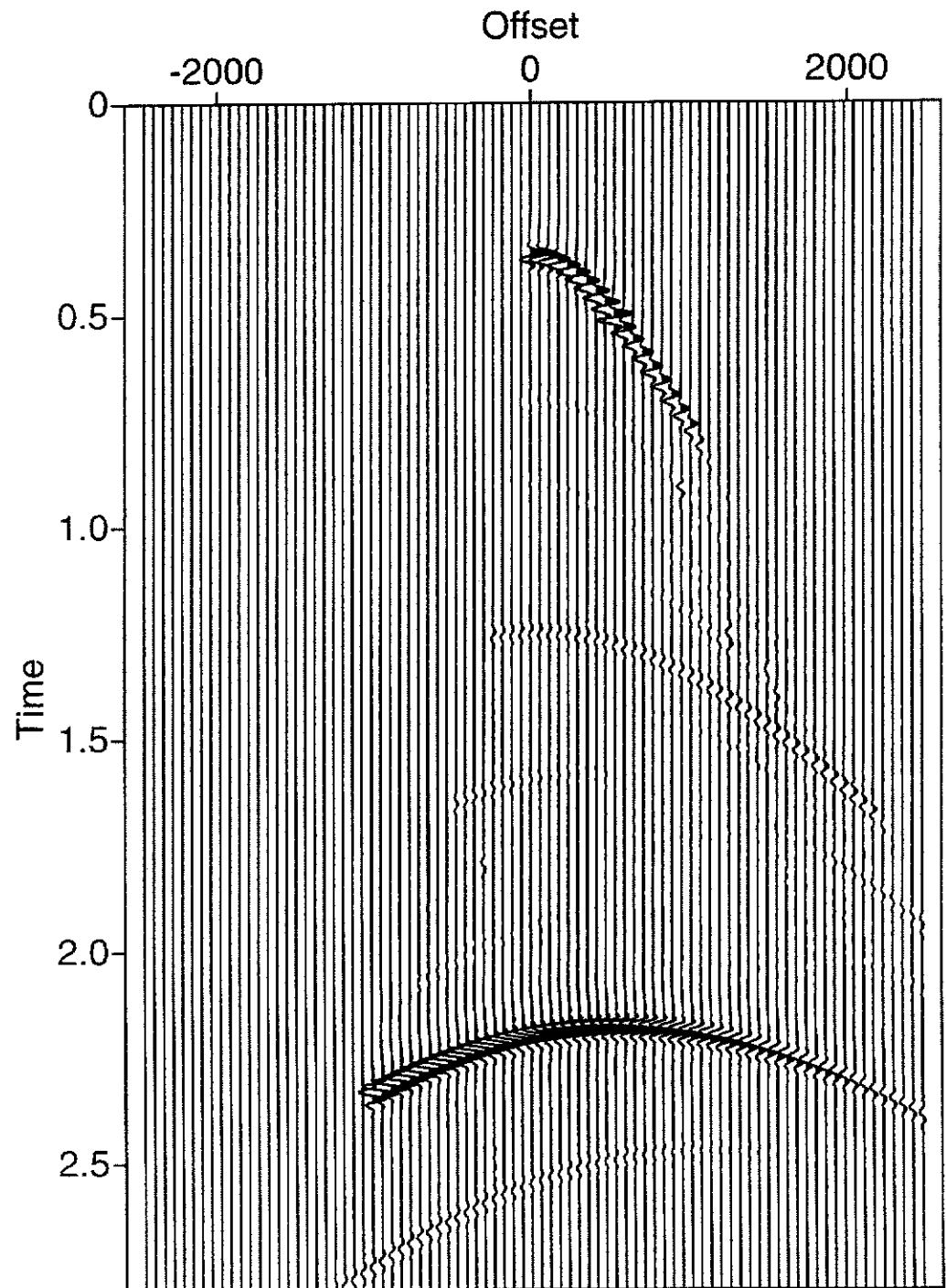
Figure (3.10)   *The synthetic record after the application of predictive deconvolution in the transform domain, followed by the inverse transforms.*
Firstly notice that an apparent mute has been applied to the data. This illustrates the extent of the radial traces. Secondly notice that the majority of multiple energy has been removed and the primary events preserved.

Figure (3.11) shows the effect of applying predictive deconvolution directly to the shot record without the application of MMO and ISR. This figure illustrates that predictive deconvolution is not a suitable tool for attenuating long period multiples pre-stack without some form of preconditioning because of the lack of stationarity of the primary/multiple wave trains. The multiples have not been removed, artifacts have been created, and the subtle primary event at 1.3 seconds obliterated. A comparison of Figures (3.10) and (3.11) demonstrates how effective the multiple attenuation process has been made by the new preconditioning transforms; MMO and ISR.

Conversely autoconvolution is a good tool for predicting longer period multiples. As shown in Chapter (2.4), the trace needs to be autoconvolved the same number of times as there are orders of multiples. This means that the longer the period of the multiples to be removed, the fewer autoconvolutions that are necessary to attenuate the surface-related multiples.
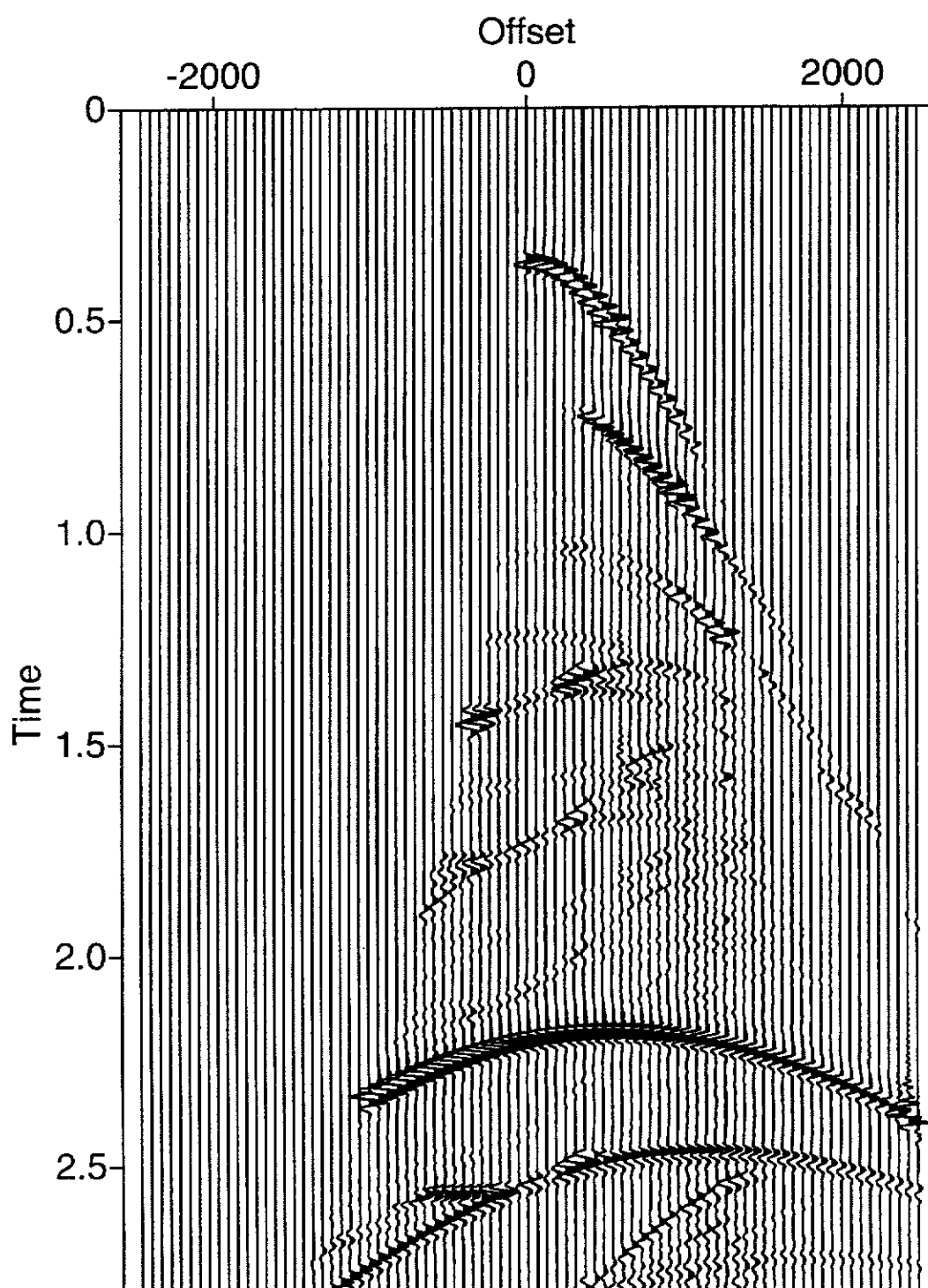
Figure (3.11)   *The synthetic record after the application of predictive deconvolution without first applying the preconditioning transforms.*

This figure illustrates that predictive deconvolution is not a suitable tool for removing long period multiples without preconditioning. The multiple energy has generally not been removed, artefacts have been created and the subtle primary at 1.3 seconds obliterated.

3.5 Summary

The mathematics of a two step forward and inverse transformation process, applicable to both shot records and CMP gathers has been derived. Based on a new generalised expression for the travel times of multiple reflections in a water layer with a dipping floor, a new transform known as the MMO transform has been created. In this new domain, water layer reverberations appear as periodic events. Based on the stretch produced by the MMO transform, a re-sampling process known as the ISR transform has been devised to create traces in which water layer multiples are not only periodic but stationary. These new transforms therefore produce pseudo zero offset traces.

The application of these two preconditioning transforms to a prestack synthetic data set with multiple reflections from a dipping sea floor, and water layer peg-leg reflections, was successfully tested. Predictive deconvolution applied in this domain significantly attenuated the multiple events and left the primary reflections unaltered.

After inverse transformation, the input traces to the transform are recovered satisfactorily. A mute zone may be observed indicating the extent of the ISR traces. It is the processors choice as to how many and the position of the ISR traces, and hence the placement of the "mute" zone.

The process developed and tested on synthetic data in this chapter, will fit conveniently into conventional processing sequences. Modules for this have been coded in the Colorado School of Mines, SU format. The only additional information required in the

trace headers is the water velocity, average sea floor dip for each shot, and the zero offset water bottom reflection time. This is easily done, enabling the transformation process to proceed rapidly and efficiently.

Following successful development and testing on synthetic data, the process needs to be applied and tested on field data. In Chapter (4), two test lines from regions with significant multiple energy, are processed and the results are compared with more conventional techniques.

Case Studies

Two case studies are presented from areas where the existence of seismic multiples has made interpretation difficult. The first is from the Perseus Gas Field, Dampier sub basin, where the water depths are relatively shallow and the overburden is made up mostly of carbonates. Mapping horizons between wells and quantitative interpretation studies have been compromised due to interference from multiples (David De Pledge of Woodside Offshore Petroleum, pers. comm.). So it was decided to test the effectiveness of the new wavefield transformation approach on data from this problem area.

Six comprehensive tests on this dataset will be shown. Several attenuation approaches in the MMO/ISR domain will be applied along with standard predictive deconvolution and the Radon Demultiple technique. Other tests were carried out but are unable to be released due to confidentiality restrictions imposed by sponsors.

The second study is on data from the South Perth Basin. This area has deep-water bottom multiple problems. There is a dipping sea floor between 500 and 700 milliseconds in two-way time. The multiples present include both simple and peg leg water bottom multiples. The contractor processing of this dataset involved two

phases (1995 and 1996) and included FK demultiple, gapped deconvolution, wave equation demultiple and Radon Demultiple processes.

These two data sets are complementary, having different water layer geometry and geology. Thus they will serve to demonstrate the applicability and performance of the MMO/ISR transforms on Western Australian datasets exhibiting representative seismic multiple problems.

4.1 Preliminary comments on the practical application of the MMO and ISR transforms to field data.

The first step before the application of the MMO/ISR transforms is the derivation of the water bottom model. Firstly, a near trace gather is formed and the water bottom picked. From these times, the zero offset time is estimated using the non-dipping NMO equation and a water velocity of 1500 m/sec.

A plane dipping layer is fitted to the depth converted, zero offset times, for each shot record. The estimated dip (of the plane layer) together with the zero offset time are then entered into each trace header.

Following the application of MMO, the missing near offset traces are reconstructed in the CMP domain. A parabolic Radon Transform is applied to the first 500m of offsets and the missing traces are reconstructed by the inverse transform.

Split spread data is generally required for the application of the ISR transform. Reciprocity is invoked to deal with the single sided marine records. The data is duplicated and the duplicated set has its source and receiver locations interchanged, thereby creating the necessary "split spread" traces artificially.

4.2 Multiple attenuation over the Perseus Gas Field [1]

The Perseus gas field lies between Goodwyn and North Rankin, which are two large gas/condensate fields in the permit WA-28-P. It is an ideal area for testing new algorithms because the geology of the area is well understood due to many years of studies by teams of geoscientists using data from dozens of wells drilled in the vicinity. In all, six different multiple attenuation techniques and combinations of techniques were applied to a subset of line 1743 from the East Dampier 3D Survey, passing through the Perseus-3A well. Other wells in the area were not available for this thesis. The zero offset VSP from Perseus-3A served to assess objectively the quality of the multiple attenuation.

Background

The Perseus field is a structural high forming the north-western margin of the Dampier Sub-basin, which is part of the Carnarvon Basin of North-Western Australia. The reservoir of the field is composed of Bathonian shallow marine sandstones within a complex structural/stratigraphic trap. The reservoir section subcrops the Upper Jurassic-Lower Cretaceous "Main Unconformity" (MU) in the Searipple Graben, a structural low separating the Triassic reservoirs of the Goodwyn and North Rankin gas fields.

The Lower Cretaceous Muderong Shale forms the main regional top seal. The Lower Jurassic Athol Formation forms the seat seal for the Perseus trap and

---

[1] Unfortunately, there are no public references for this case study. My knowledge stems from my employment at Woodside Offshore Petroleum Pty. Ltd. and access to proprietary data which remains confidential.

subcrops the Main Unconformity northwest of North Rankin, defining the eastern edge of Perseus and separating the two fields. The Muderong Shale (top seal) is overlain by Lower Cretaceous - Tertiary shelfal carbonates.

The main features of line 1743, relevant to this study, are highlighted in Figure (4.1). A larger amplitude horizontal multiple event runs through the reservoir section. This event can be clearly seen towards the bottom of the VSP comparison panel in later figures (e.g. Figure 4.3). The other dominant multiple energy appears on the right of the section where the dipping events are actually the primary events and the horizontal events are the multiples. This is known from another well intersecting this geology on an adjacent line. Interval velocities decrease beneath the Main Unconformity (2.1 to 2.2 secs). In analysing the results the events to note are the flat, high amplitude multiple event which runs through the reservoir section and the dipping events on the right of the section.

The processing sequence

In any seismic processing sequence there are many possible steps from shot records to final sections. No multiple attenuation process can be considered in isolation from the whole sequence. Most demultiple techniques are best applied in the pre-stack domain, but their effectiveness is judged on the final output post stack. In the results that follow, every attempt has been made to vary only the method of multiple removal, so that valid comparisons between various methods may be made. Table (4.1) describes the overall processing sequence that was applied to the data.
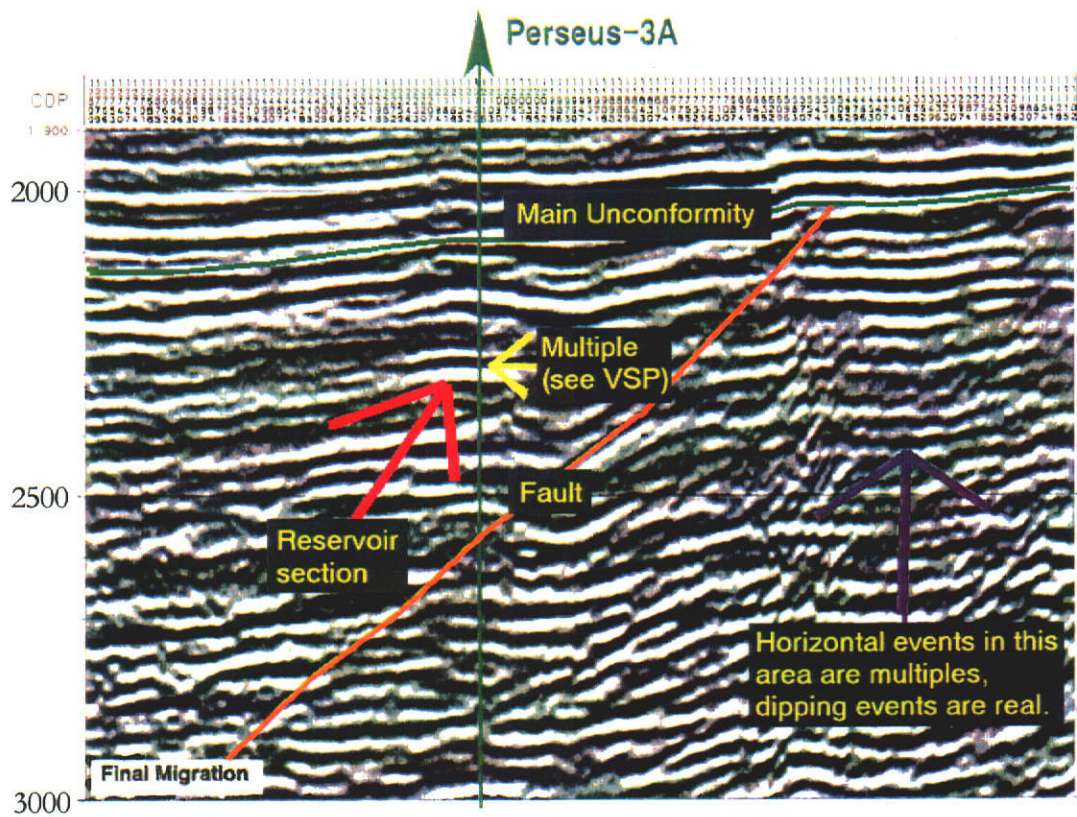
Figure (4.1) A portion of line 1743 from the East Dampier 3D survey.

This portion of line has a time range from 1900 to 3000 msecs and contains the Perseus-3A well. The Main Breakup Unconformity (MU) is indicated by the green interpretation. The reservoir section as indicated, pinches out above and to the right of the pink arrow, against MU and the orange fault. The yellow arrow indicates a large multiple, which runs through the reservoir section. This multiple is clearly seen towards the bottom of the VSP comparison panel in Figure 4.3. The purple arrow on the right of the section indicates another reservoir section. This is the flank of the North Rankin Gas Field. Surprisingly the dipping events are the real events and the horizontal events are multiples.

4.3 Deeper water multiples, Offshore Western Australia

The second case study is line 2594 from the Naturalist Survey in permit WA-227-P, offshore Perth Basin. This line was chosen because it represented data with longer period multiples, which have been troublesome to remove by commercially available techniques.

Background

The Perth Basin is essentially a north south trending half graben, bounded on the west by the Leeuwin Block (Figure 4.9). The top of the Leeuwin Block can be seen at around one second on the left of the section. The right edge of the Block is indicated by the steep reflection and termination of the Permian events. The basin formed in response to rifting along the western margin of Australia from the Late Carboniferous until continental breakup in the Early Cretaceous.

Following rifting in the Permian a stable tectonic environment ensued with a predominantly fluvial deltaic succession being deposited during the Triassic through to the Middle Jurassic. These sediments consist of interbedded sandstones, siltstone, claystone and coals. During the Neocomian, further rifting resulted in the separation of the Australian and Indian plates. During this stage uplifting, tilting and erosion of the Permian sediments took place. Hence these sediments are the basis of the dipping reflectors seen below the Main Unconformity, to the east of the Leeuwin Block (Eddy Buckovic of Woodside Offshore Petroleum, pers. comm.).
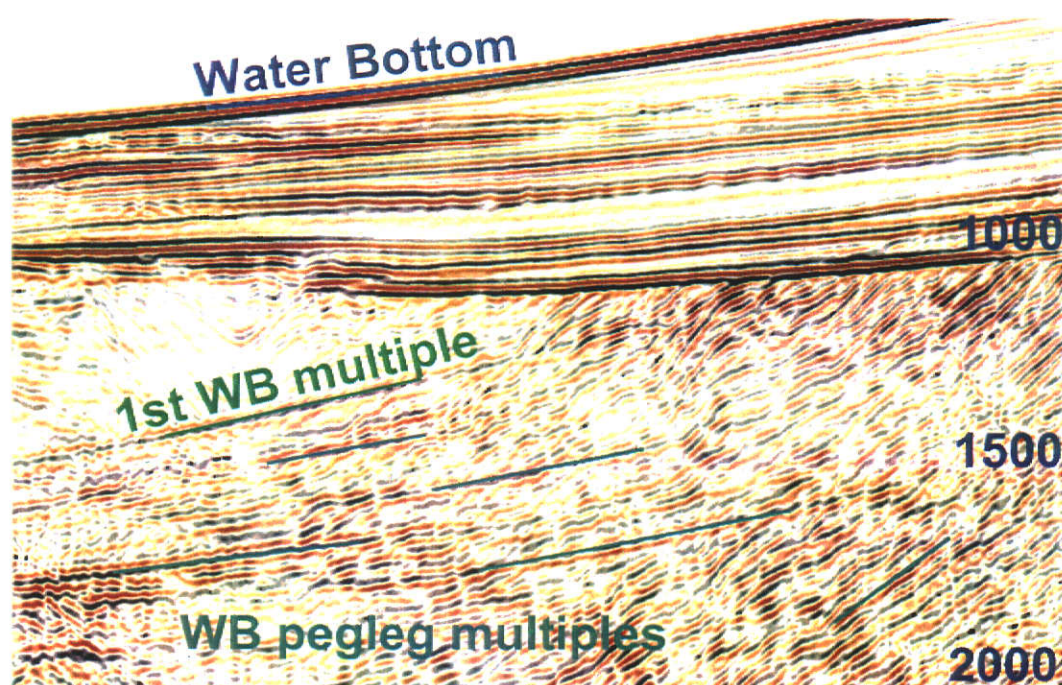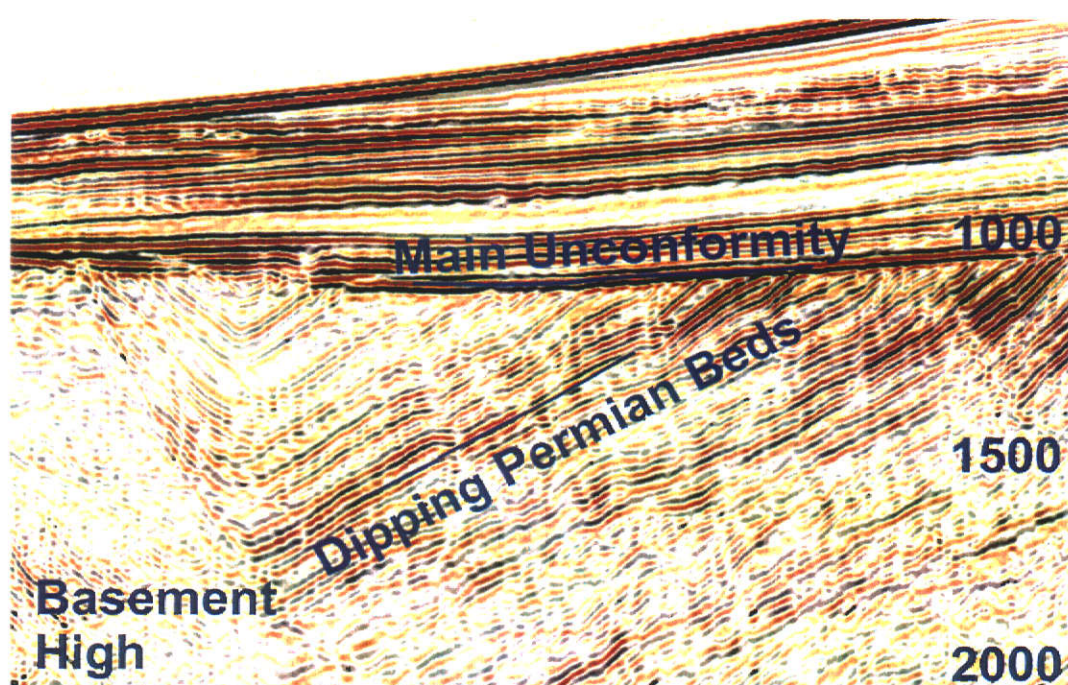
Figure (4.9a)

Figure (4.9b)

Figure (4.9) A comparison of line 2594 before and after multiple attenuation.

Figure (4.9a) shows the section with no multiple attenuation applied. Below the Main Unconformity the section is dominated by water bottom multiples. After attenuation of the multiples (Figure (4.9b)) the true geology can be seen.

The Warnbro Group was deposited immediately above the Neocomian Unconformity (Main Unconformity) and consists of marine to non-marine mixed clastics. These were followed by the marine sediments of the Coolyene Group. Mixed estuarine to marine conditions persisted throughout the Tertiary to the present day.

Without any specific demultiple procedure the imaging below the Main Unconformity is poor and contaminated with water bottom multiples (Figure (4.9a)), making structural and stratigraphic interpretation difficult.

The processing sequence

The overall processing sequence applied to this dataset is very similar to that applied in the Perseus case study. It is described in Table (4.3). The aim was to produce a dataset suitable for MMO/ISR/autocon. The water bottom model was derived in the manner described in Chapter (4.1).

Next, geometry was assigned to the trace headers. This involved the normal geometry settings as well as shot and receiver station numbers to allow the easier use of reciprocity, later in the flow. The standard resample to 4 msec was step 2. The data was then band pass filtered to what was considered to be the useful bandwidth (6-12-70-90 hz corner frequencies). Shot and Channel consistent scaling was again necessary as amplitude plots demonstrated shot and channel consistent variations in amplitudes. Velocity analysis was conducted every 1 km in order to apply normal

#	PROCESS	DISCUSSION
1	Identing	Assign geometry to the trace headers
2	Resample to 4 msec	
3	Trace editing	Kill noisy traces
4	Bandpass filtering	6-12-70-90 Hz
5	Shot / Channel consistent scaling	
6	Velocity analysis	Every kilometre
7	NMO	With 100% velocity field
8	Shot FK	Polygon cut which is approximately equates to +/- 3000 m/s
9	Sort to common offset gathers	
10	Trace interpolation	Insert one trace between each 2
11	Sort to common receiver gathers	
12	Receiver FK	Polygon cut which is approximately equates to +/- 3000 m/s
13	Sort to common midpoint gathers	
14	Split data into offset distributions	
15	Extrapolate gathers to zero offset	
16	Inverse NMO	
16	Merge and sort to common shot	
17	Form split spread data using reciprocity	
18	MMO/ISR preconditioning	
19	Autoconvolution	3 autoconvolutions were performed
20	Inverse MMO/ISR	
19	Velocity analysis	Every kilometre
20	DMO	Kirchhoff implementation of dip move out
21	PreSTM	Kirchhoff implementation of pre-stack time migration
22	Stack	
23	Zero phasing/Deabsorption	

Table (4.3) Processing sequence for line 2594 from the Naturalist survey.

moveout to the gathers prior to shot FK. A mild shot FK filter was applied purely to reduce incoherent noise.

Given the 25 m shot interval and 12.5 m group interval, in order to form split spread data with regular spacial sampling, it is necessary to interpolate shots. This was achieved in the common offset domains by interpolating one new trace between each pair of original traces. Again, the interpolation was done using proprietary software.

Now that the shot and receiver intervals are the same, the data can be sorted to common receiver domain and the same FK filter as used on the shots, applied to reduce noise further.

Near offset traces were then synthesized in the same manner as described earlier. Split spread gathers were then formed (as described in Chapter (4.1)).

MMO/ISR/autocon was applied at this stage in the processing flow. Three autoconvolutions per trace were performed. Derivation of the inverse wavelet was achieved using proprietary software.

Following the demultiple tests, a fairly standard processing flow was applied, including Kirchhoff DMO and pre stack time migration, in order to produce the final sections on which performance evaluations may be made.

Figure (4.10) shows the shape of the radial traces for a water bottom at 500 msec and a dip of two degrees (approximately parameters applicable to this dataset). Notice that although pseudo "split spread" gathers needed to be formed, not all of the negative offsets were needed.

Results and discussion

Figure (4.11) shows a migrated stack of the data with no multiple attenuation applied. The water bottom simple and pegleg multiples are clearly visible, dominating the dipping Permian reflectors below the Main Unconformity.

Figure (4.12) is the original contractor-produced section where gapped deconvolution and FK demultiple were applied to attenuate the multiples, but did not have the benefit of pre-stack time migration. Multiple energy clearly remains in the section when compared with Figures (4.13) and (4.14). A high amplitude water bottom peg-leg multiple can be clearly seen at around 1750 msec on the left of the section crossing the interface between the Permian Beds and the basement. The "wormy" appearance is probably caused by damage done to the primary events by the harsh FK demultiple procedure. In addition, the imaging of events below the Main Unconformity should not be compared with Figures (4.13) and (4.14) because these latter sections have had pre-stack time migration applied to them.

Figure (4.13) shows some recent contractor reprocessing of the data which included wave equation multiple attenuation, gapped deconvolution and Radon Demultiple followed by pre-stack time migration. The multiples are more effectively removed

Offset

| -3000 | -2000 | -1000 | 0 | 1000 | 2000 | 3000 |
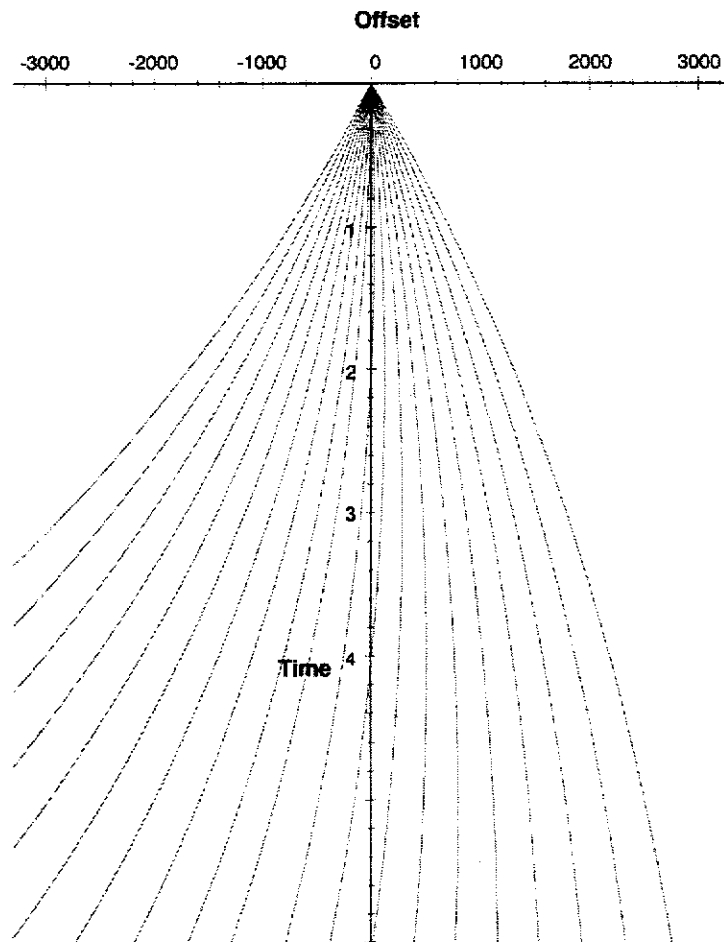
Time

Figure (4.10): Isostretch curves for a typical shot record from line 2594, Naturaliste Survey.

Curves representing a sample of the paths of the Iso-Stretch Radial Traces for a water bottom primary zero offset time of 500 msec and dipping sea floor of two degrees.

than in the original processing. However the "wormy" appearance below the Main Unconformity is still evident, indicating that primary energy has been attenuated along with the multiple energy. The imaging below the main unconformity is better than in Figure (4.12).

Figure (4.14) gives the migrated section to which the MMO/ISR/autocon procedure has been applied. As can be clearly seen, the water bottom multiples, both the simple and the peg leg multiples, have been attenuated. The attenuation of the multiples has allowed better velocity picking and hence better migration and stacking of the data. The edge of the Leeuwin block on the left of the section is well imaged down to around four seconds. The dipping events terminate at the edge of the Leeuwin Block. The events below the Main Unconformity are more continuous and the fault pattern is much clearer. Smaller faults in the dipping beds to the right of the fault are now visible.

The four sections had similar processing flows apart from the differences mentioned above.
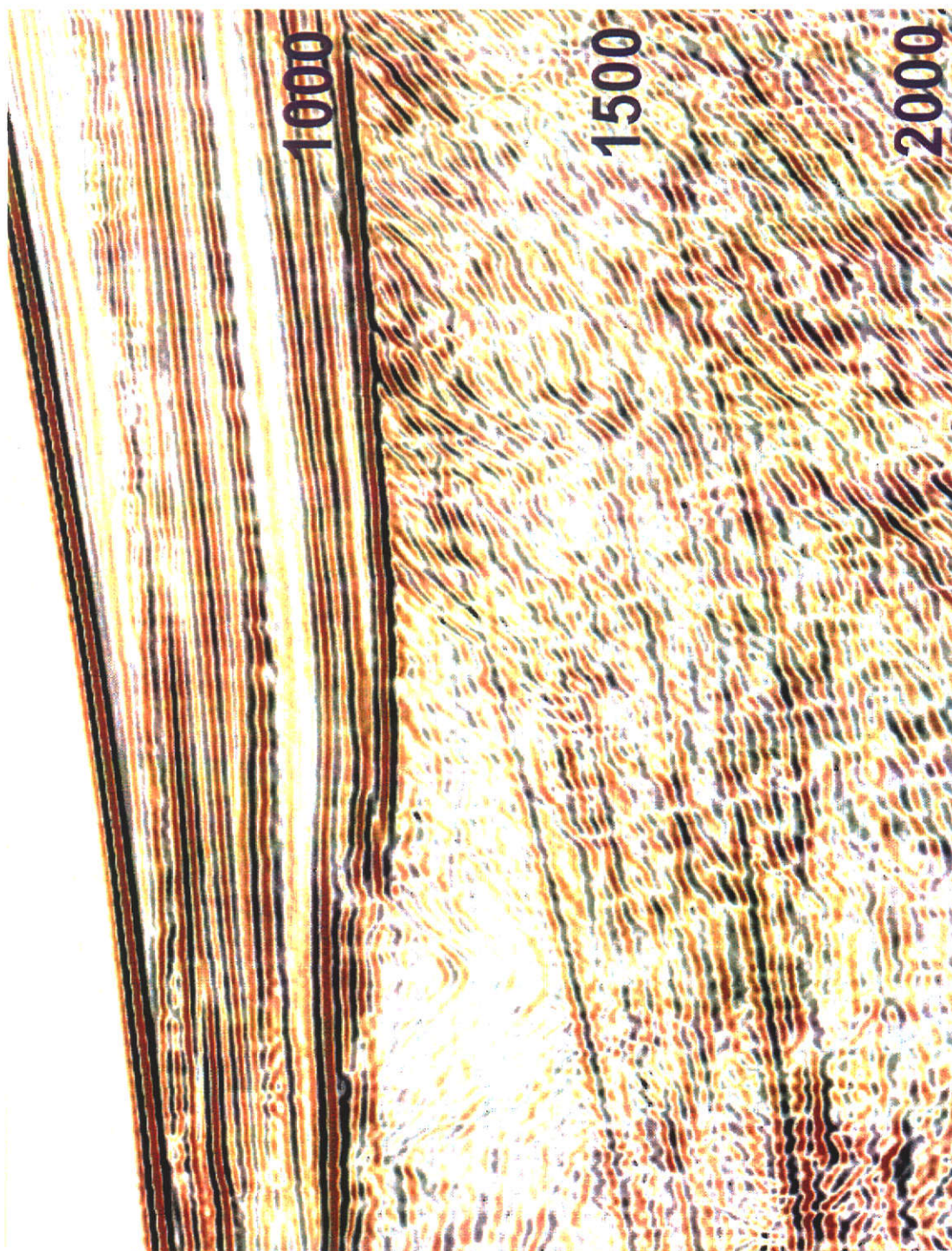
Figure (4.11) Line 2594 with no demultiple procedures applied.
It is riddled with water bottom multiples, both simple and pegleg events.
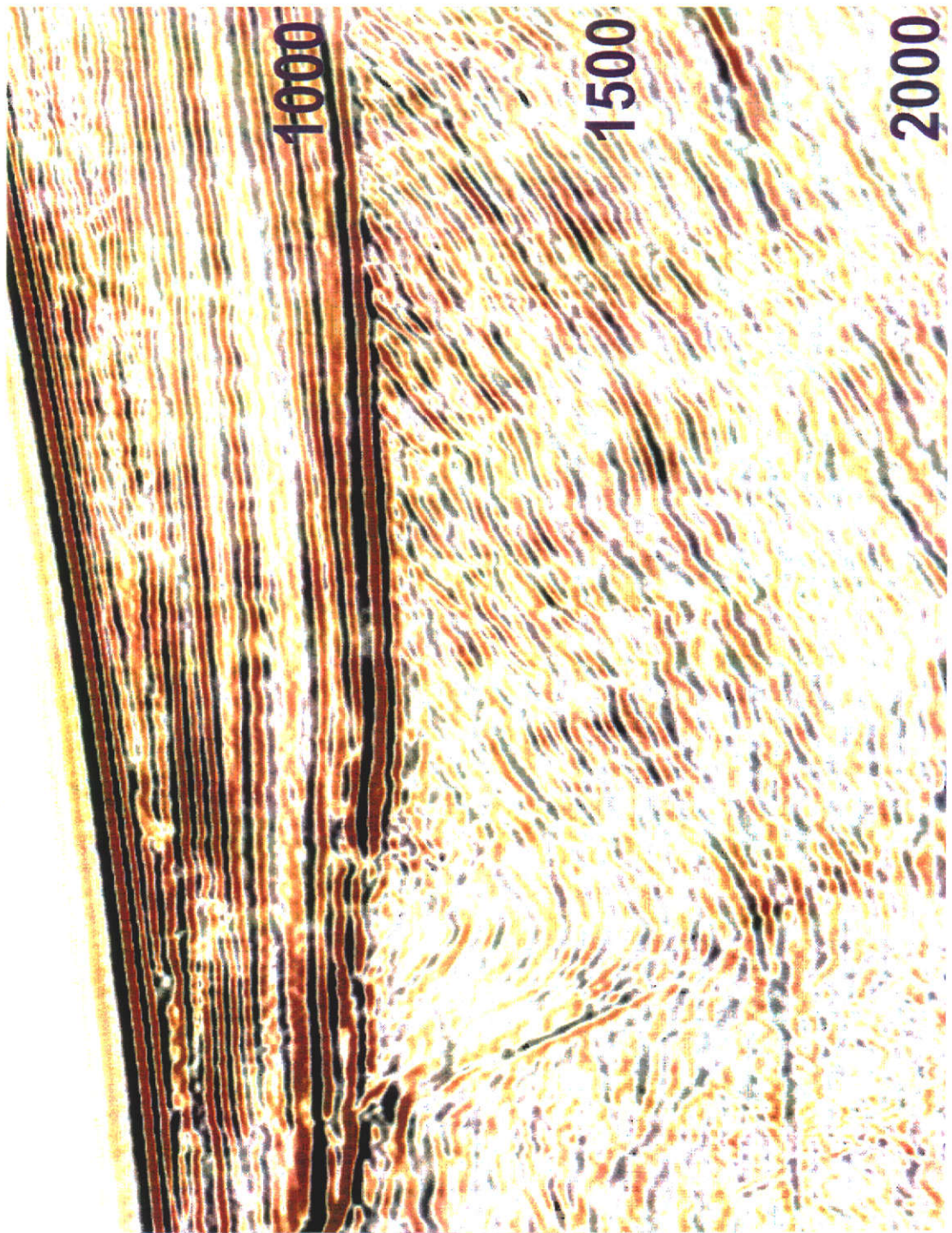
Figure (4.12) The original contractor processing of Line 2594.
The multiple energy has been reasonably attenuated. However multiple energy is still evident and the imaging of the primary energy is poor.
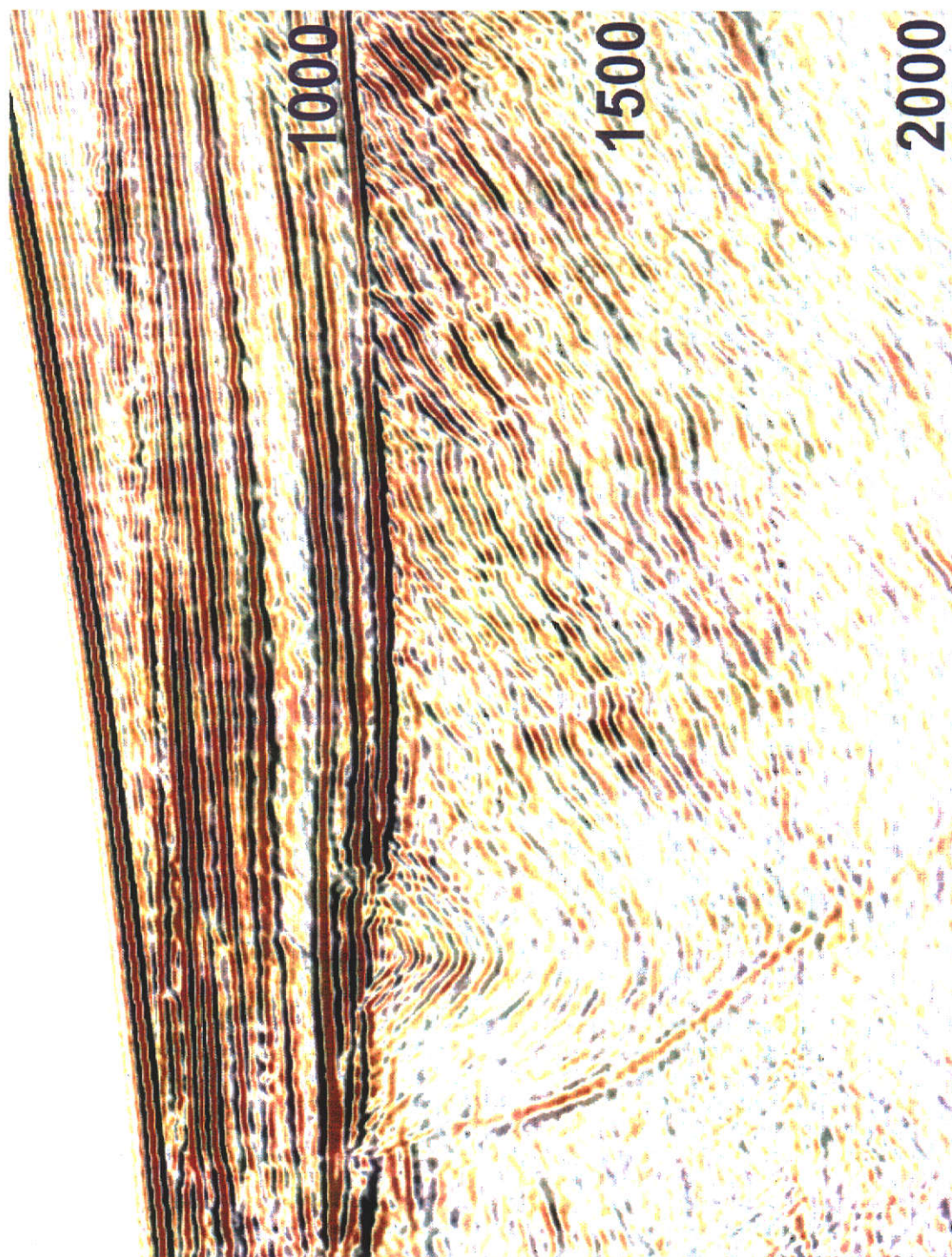
Figure (4.13) Line 2594 with the demultiple sequence; WEMA, gapped deconvolution and Radon.
The multiples here have been well attenuated. However the primary events have not been well preserved.
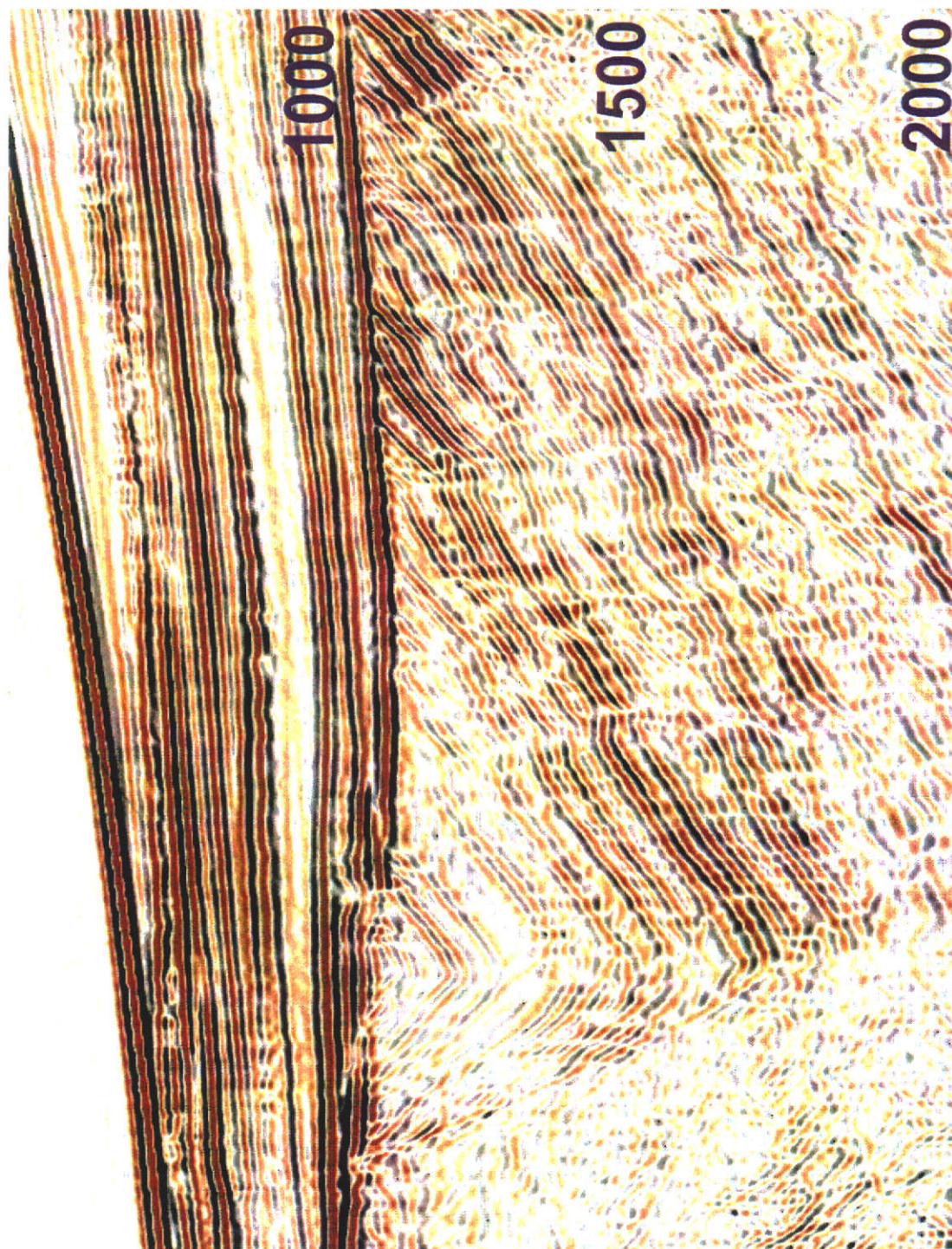
Figure (4.14) The MMO/ISR preconditioning transforms followed by autoconvolution.
The multiples have been nicely attenuated, and just as importantly the primary events have been well preserved.

Summary

The new preconditioning transforms have been applied to Line 2594 from the Naturalist Survey. The MMO/ISR and autoconvolution results have been compared with two separate contractor results. They have been found to be superior in both multiple attenuation and in the preservation of the primary events.

The comparison is not perfect as the processor and the processing sequence (and parameters) varied between each test. The results though qualitative, provide convincing evidence of the effectiveness of the new pre-conditioning techniques developed in this thesis.

It has been found that the transforms are quite robust with respect to the water bottom model. The main result of having the model not quite correct is that the introduced period of the multiples changes. The multiples do lose periodicity, but at a slower rate than the change in their period.

The aim of the preprocessing steps taken was to produce a dataset suitable for testing a range of demultiple techniques. Step 1 was the identing or assigning the acquisition geometry specifications to the headers. This involved the normal geometry settings as well as shot and receiver station numbers to allow the easier use of source-receiver reciprocity, required later in the processing sequence. The standard resample to 4 msec was step 2. This is done in order to save computer time. It still allows a maximum Nyquist Frequency of 125 Hz. Next it was necessary to kill noisy traces. Noisy traces were defined as having amplitudes that were approximately 10 times that of the surrounding traces. The data was then band pass filtered to what was considered to be the useful bandwidth of the data (5-10-60-85 Hz corner frequencies).

Shot and Channel consistent scaling was necessary as amplitude plots demonstrated shot and channel consistent variations in amplitudes. Each trace was scaled so that its amplitudes statistically fitted in with surrounding traces. Velocity analysis was conducted every 650 m in order to apply normal moveout to the gathers prior to shot domain FK filtering. A mild shot FK filter was applied purely to reduce incoherent noise.

Given the 50 m shot interval and 12.5 m group interval, it was necessary to interpolate new shot records (in order to form split spread data with regular spatial sampling). This was achieved in the common offset domain by interpolating three new traces between each pair of original traces. This interpolation was done using Shell proprietary software held by Woodside Offshore Petroleum.

#	PROCESS	DISCUSSION
1	Identing	Assign geometry to the trace headers
2	Resample to 4 msec	
3	Trace editing	Kill noisy traces
4	Bandpass filtering	5-10-60-85 Hz
5	Shot / Channel consistent scaling	
6	Velocity analysis	Every 650 metres
7	NMO	With 100% velocity field
8	Shot FK	Polygon cut which is approximately equates to +/- 3000 m/s
9	Sort to common offset gathers	
10	Trace interpolation	Insert 3 traces between each 2
11	Sort to common receiver gathers	
12	Receiver FK	Polygon cut which is approximately equates to +/- 3000 m/s
13	Sort to common midpoint gathers	
14	Split data into offset distributions	
15	Extrapolate gathers to zero offset	
16	Inverse NMO	
16	Merge and sort to common shot	
17	Form split spread data using reciprocity	
18	DEMULTIPLE tests	
19	Velocity analysis	Every 650 metres
20	DMO	Kirchhoff implementation of dip moveout
21	PreSTM	Kirchhoff implementation of pre-stack time migration
22	Stack	
23	Zero phasing/deabsorption	
24	Noise Reduction	

Table (4.1)   Processing sequence for the Perseus dataset.

After making the shot and receiver intervals the same, the data was sorted to the common receiver domain and the same FK filter as used on the shots, was applied to reduce noise further.

Near offset traces were synthesized and split spread data formed in the manner described in Chapter (4.1). The data at this stage was now comprised of fully populated split spread shot records, well prepared as common input for all of the tests.

Next in the sequence the demultiple tests were conducted. The procedures evaluated are shown in Table (4.2). Abbreviated references (in *Italics*) to the test procedures defined in Table (4.2) will be used in the text of this thesis for convenience.

TEST ABREVIATION	TEST EXPLANATION	FIGURE NUMBER
No Demult	No specific demultiple, stacking demultiple only	4.3
GD	Gapped deconvolution; 350 msec filter, 72 msec gap, approx 2 sec design windows	4.4
Radon	Radon Demultiple	4.5
GD Radon	Gapped deconvolution followed by Radon Demultiple	4.6
MMO/ISR/autocon	MMO/ISR preconditioning before autoconvolution based multiple attenuation	4.7
MMO/ISR/GD	MMO/ISR preconditioning followed by gapped deconvolution in the transform domain	4.8

Table (4.2)   The six demultiple procedures tested on the Perseus dataset.

For the control dataset, the demultiple step was bypassed all together: the data went straight into the migration procedures.

For the first demultiple test, gapped deconvolution (*GD*) was applied in the shot domain. An active filter length of 350 msec was used, with a 72 msec gap. Two design windows were used of about 2 seconds in length. Seven traces were used to

design the filter for the centre trace. These were the final parameters chosen after a significant amount of parameter testing.

The *Radon* test used a moveout range (P range) from −300 msec to 2000 msec at 4000 metres offset. Six hundred P traces were modelled. Several mutes were tested but the best results were obtained by muting from −300 to 70 msec, bringing the multiples back to the x-t domain and removing the modelled multiples from the input CMP gather. For the *GD-Radon* test the best *GD* data were then processed with the best *Radon* test parameters.

The *MMO/ISR/autocon* test used 3 convolutions (thus the amplitudes were predicted correctly for three orders of multiples). The wavelet processing and adaptive removal was done with proprietary software.

The *MMO/ISR/GD* test used a 350 msec active filter length and a 72 msec gap. Windows of three seconds duration, were used for the design and application of the filters. Slightly better results were obtained this way, rather than using the full trace length.

Velocities used in the general processing sequence were picked at 650 meter intervals on the *MMO/ISR/autocon* dataset and checked on the *GD* data. In this way a single velocity function, to be used for all tests, was derived. The *MMO/ISR/autocon* dataset was chosen for the velocity analysis because i) The *MMO/ISR/autocon* procedure does not rely on velocity information and ii) velocities could be picked

unambiguously following *MMO/ISR/autocon*. This velocity function was used during the application of the *Radon* even though the profile could not be picked as accurately on the *Radon* or the *No Demult* data.

Finally Kirchhoff DMO and pre-stack time migration (PreSTM) were applied to all data sets. Following stacking, the data was transformed to zero phase. The VSP trace from the Perseus 3A well was then used to judge objectively the various demultiple results. A re-datuming shift of 12 msec (down) was applied to the VSP trace to obtain the best fit to the seismic traces on all of the 2D tests. Different mutes were applied to the traces implicitly by the various demultiple procedures (this is illustrated on the gather displays), but this is not considered critical to the final results: however, identical mutes were applied after DMO and again after migration.

Description of Montages

The results are presented in a series of montages where all displays, trace scaling and so forth are identical. This comprehensive set of displays is designed to simplify the evaluation of the various multiple attenuation procedures. Figure (4.2) illustrates the layout of the montages and will be referred to during this description. Panel A is a portion of a migrated section. Obviously it is vital that the final migrated section be pleasing to the interpreter. The events present need to represent true geological boundaries. Panels B and C are a semblance and a CMP gather respectively. These are from the closest location to the well on which velocities were picked. The ability

Panel C

Panel F

Panel B

Panel E
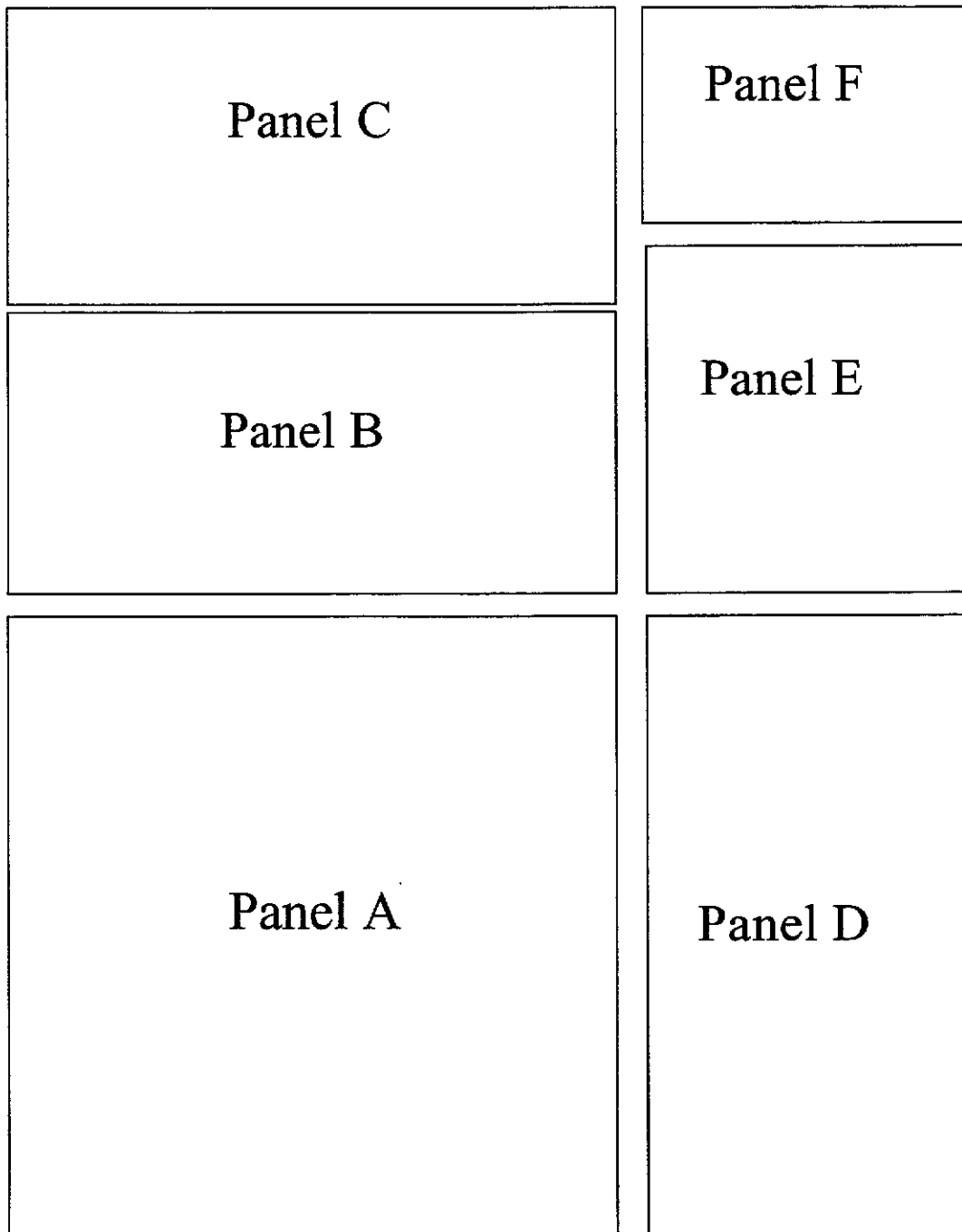
Panel A

Panel D

Figure (4.2) Montage layout (Figures (4.3) to (4.8)).

Panel A is a portion of the seismic section. Panels B and C are a semblence plot and gather from near the well location. Panel D is the autocorelation of the portion of seismic data in Panel A. Panel E is a VSP comparison through the reservoir section. Panel F is the amplitude and phase spectrum through the reservoir section.

unambiguously pick velocities is vital to the success of any processing project. Hence evaluation of the ability of a multiple attenuating procedure to enhance velocity picking is important. The velocity profile used throughout this study is displayed on the semblance display. The time range for Panels A, B and C is from 1900 to 3000 msecs.

Panel D is a one sided autocorrelation. It was calculated from the portion of data displayed in Panel A. The process of autocorrelation determines the amount of periodic energy present and hence is an important diagnostic tool.

Panel E is a wiggle trace display where the centre trace is the VSP trace from the Perseus-3A well, and the eight surrounding traces are from the seismic data, either side of the well. The nature of the VSP experiment allows VSP data to be virtually free of multiple energy. Hence the closer the data resembles the VSP trace, the better the attenuation of multiples has been. A correlation coefficient between the VSP trace and the closest surface seismic trace, is therefore, a quantitative measure as to the effectiveness of the multiple attenuating routines. A correlation coefficient was calculated over the reservoir section of this data, after the application of a long window AGC, and is displayed above Panel E. As mentioned previously a large amplitude multiple event is visible on the eight surrounding traces (especially prior to multiple attenuation) between 2250 and 2300 msecs.

Finally Panel F is the amplitude and phase spectra through the reservoir section. It is important to ascertain the effect that a multiple attenuation procedure has had on the

bandwidth of data. In addition, seismic multiples can also cause notching of the amplitude spectrum and hence their effective removal results in the removal of the notches.

Results and Discussion

The results will be discussed by comparing attributes of single panels over all of the tests. Abbreviated names and figure numbers will be used to refer to the various tests. A listing of these is available in Table (4.2).

The dominance of the dipping events in the final sections, varies widely from test to test. They are most evident on the *MMO/ISR/autocon* section (Figure 4.7).

In the center of the section (CDP 11900, 2400 msec) is a high amplitude dipping event (Figure (4.3)). Most of the test results contain conflicting dips near the top of this event. On some of the sections (eg. the *GD* section, Figure (4.4)), the dipping event appears to be pinching out against a flatter event. This interpretation is inconsistent with the current geological interpretation. *MMO/ISR/autocon* (Figure (4.7)) shows the best results (subjectively judged by an interpreter), with the beds thinning to the right but not pinching out. This detail is difficult to see on the A4 montages. It was described by a stratigrapher on the full size plots.

The best seismic to VSP match through the reservoir section (2000 to 2200 msec), by visual inspection is with *MMO/ISR/autocon (Figure (4.7))*, on the other sections the match deteriorates just above 2300 msec at a localised event which is absent on the

VSP trace. This is a high amplitude flat event on the seismic section, thought to be a water bottom peg leg. Only the MMO/ISR data (autocon and gapped decon) have significantly attenuated this event, as can be seen on the VSP comparison (Figures (4.7) and (4.8)).

The correlation coefficient (CC), has been calculated over the interval from 1800 to 2500 msec. The best correlation plot was obtained with the *MMO/ISR/GD* (0.82) (Figure (4.8)) method followed by *MMO/ISR/autocon* (0.81) (Figure (4.7)). The other methods in the range 0.6 to 0.7 were *No Demult, GD, and Radon (Figures (4.3), (4.4) and (4.5) respectively)*. The remaining tests had values in the range 0.7 to 0.75. The combination *GD - Radon Demultiple* (Figure (4.6)), which is often used in production processing, had a correlation coefficient of just 0.73.

MMO/ISR/autocon (Figure 4.7) was the most effective at removing the water bottom event from the autocorrelation. Because of the velocity inversion below the Main Unconformity, *Radon* (Figure (4.5)) was not expected to work particularly well, as confirmed by the results.

The displayed CDP gather is located near the well location. The dipping noise, evident on most of the gather displays, was attenuated by *MMO/ISR/autocon*, however the *MMO/ISR/autocon* gather is very noisy (Figure (4.7)). This noise is still evident on the final display. More post stack processing for noise reduction on the *MMO/ISR/autocon* data would typically be applied.

The most significant observation from the semblance display is related to the *Radon* test which has a stair/case appearance (Figure (4.5)). The resolution is not improved in comparison to the *No Demult* result (Figure (4.3)).

The *MMO/ISR/GD* data (Figure (4.8)) has the broadest spectrum over the target time range and the MMO/ISR/autocon (Figure (4.8)) data the narrowest, with reduced high frequencies. This drop in bandwidth is not visually evident on the section.
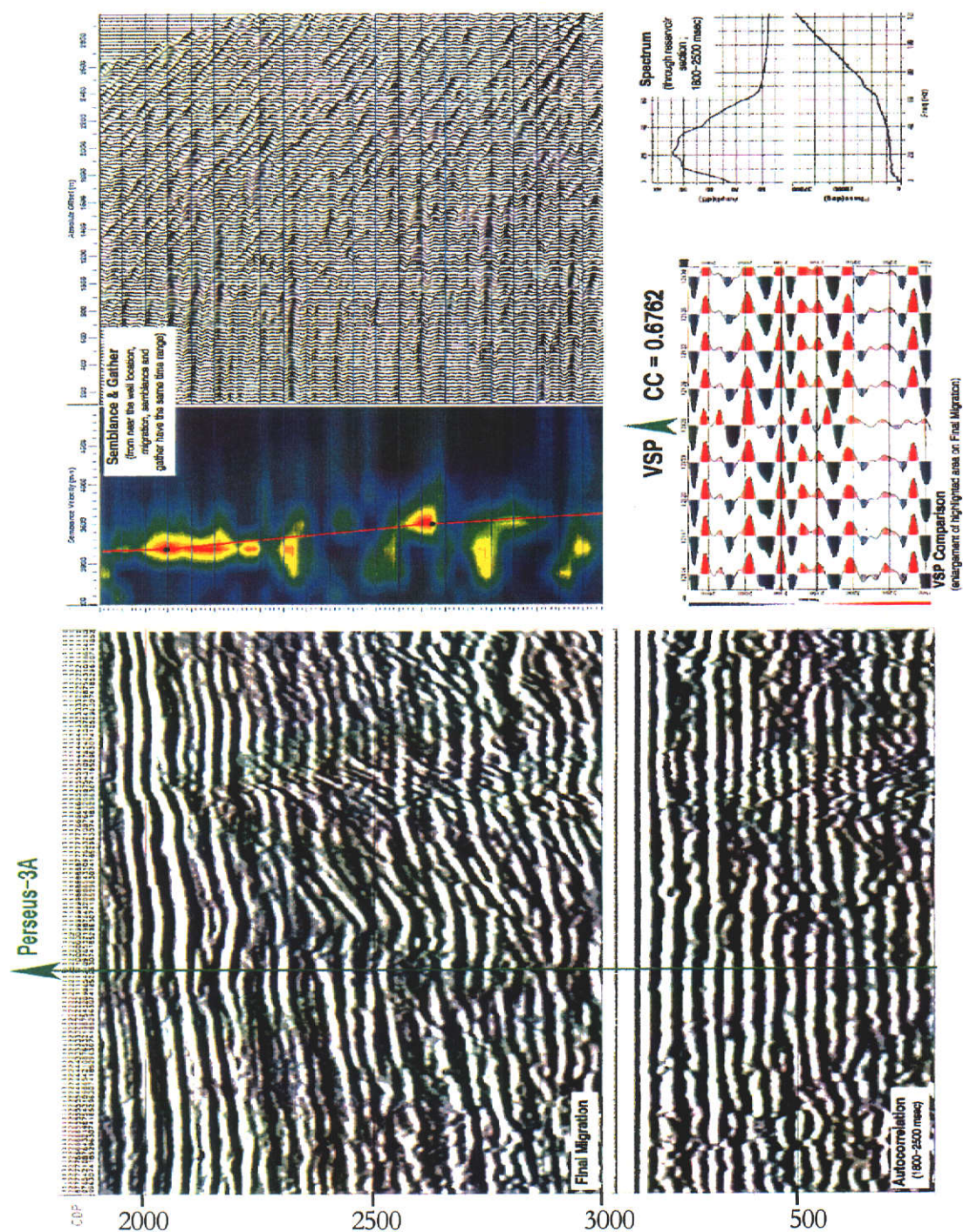
Figure (4.3) No specific demultiple procedure – the control.
Low correlation coefficient. Significant multiple energy as shown on the seismic data, autocorrelation and VSP comparison.
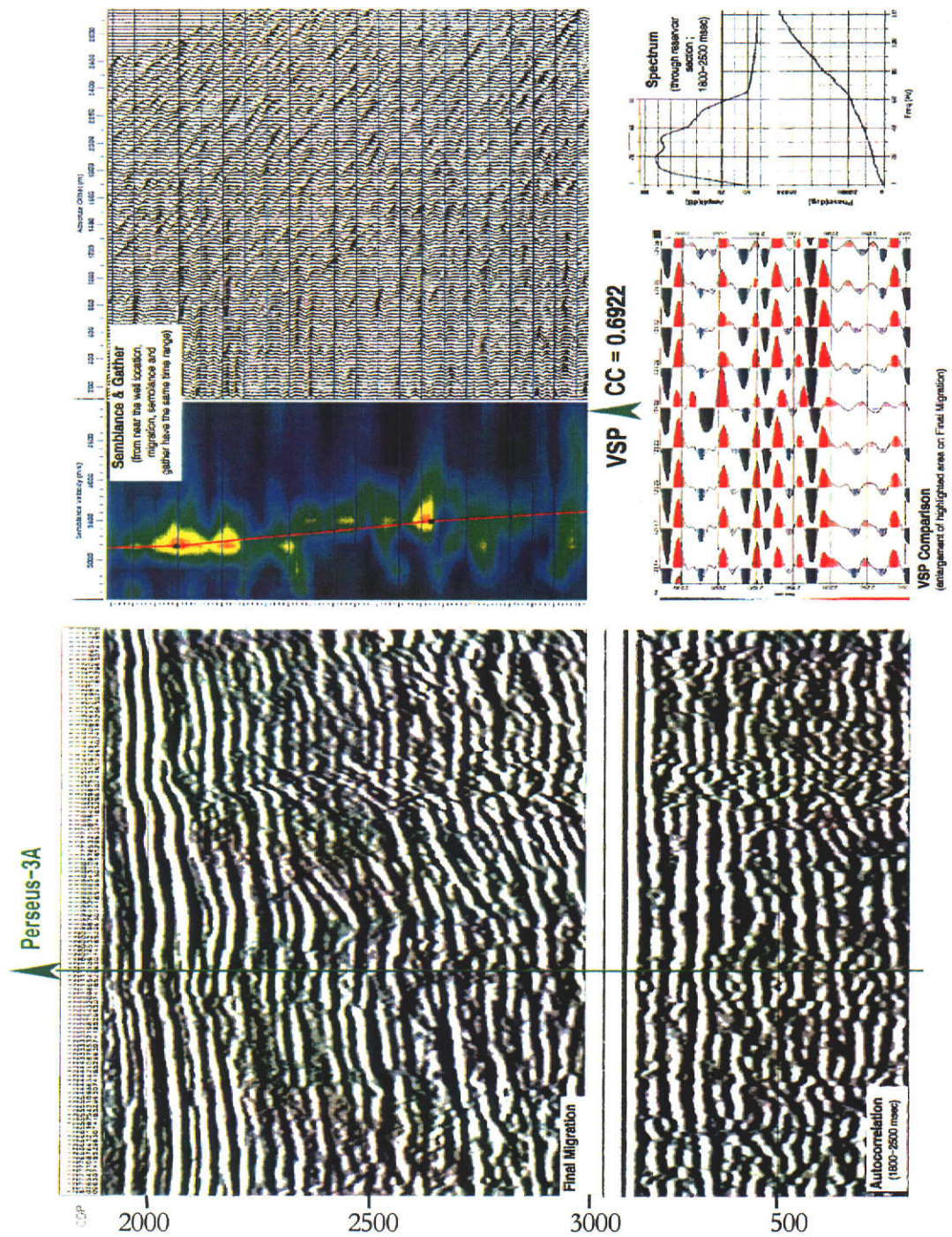
Figure (4.4) Gapped deconvolution in x-t domain.

A reasonable job. Velocity picking is improved. The Correlation Coefficient is still fairly low. Multiples are not very well attenuated.
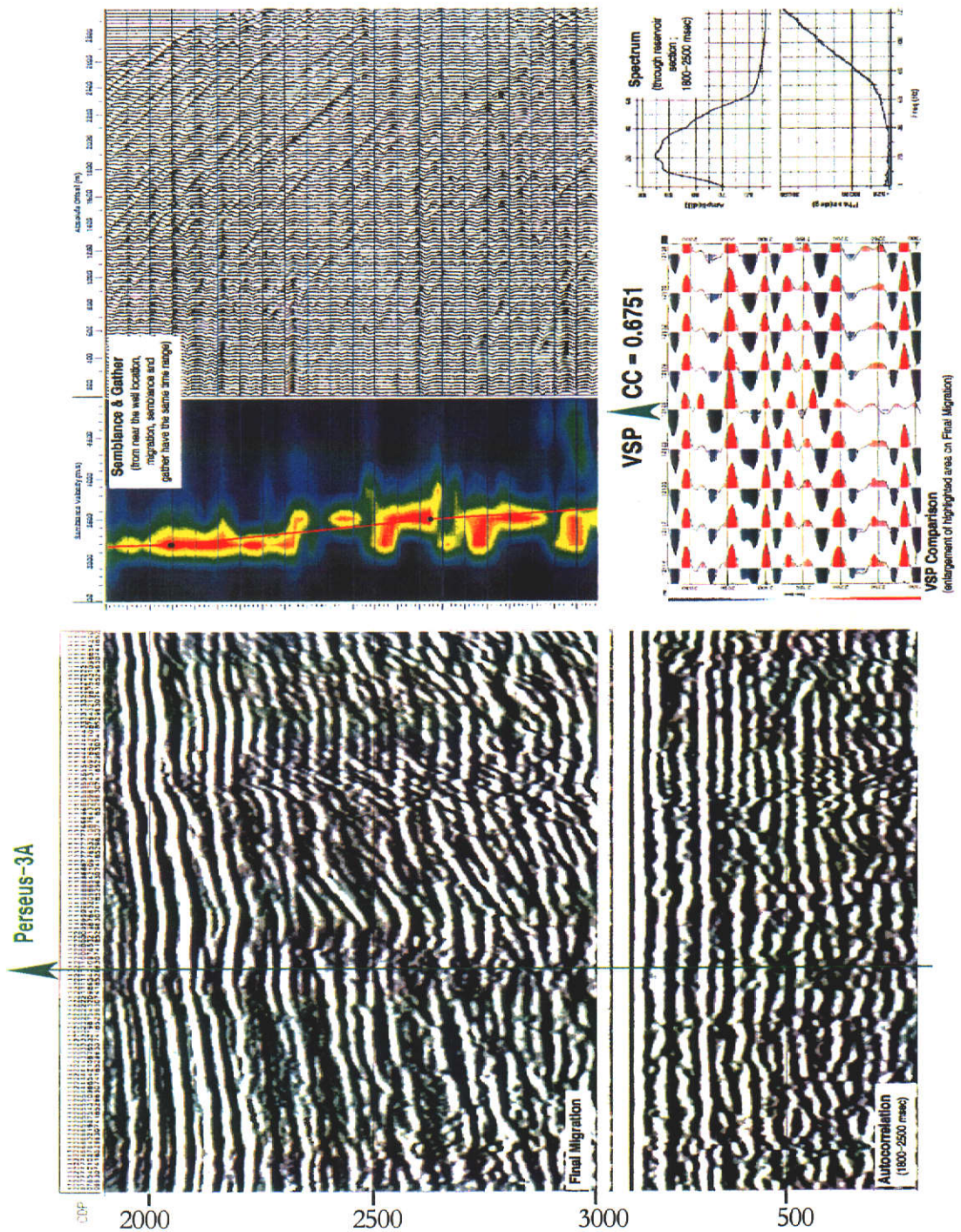
Figure (4.5) Data with Radon Demultiple applied to it.
Velocity picking is ambiguous. Correlation coefficient is low. Multiples are not very well attenuated.
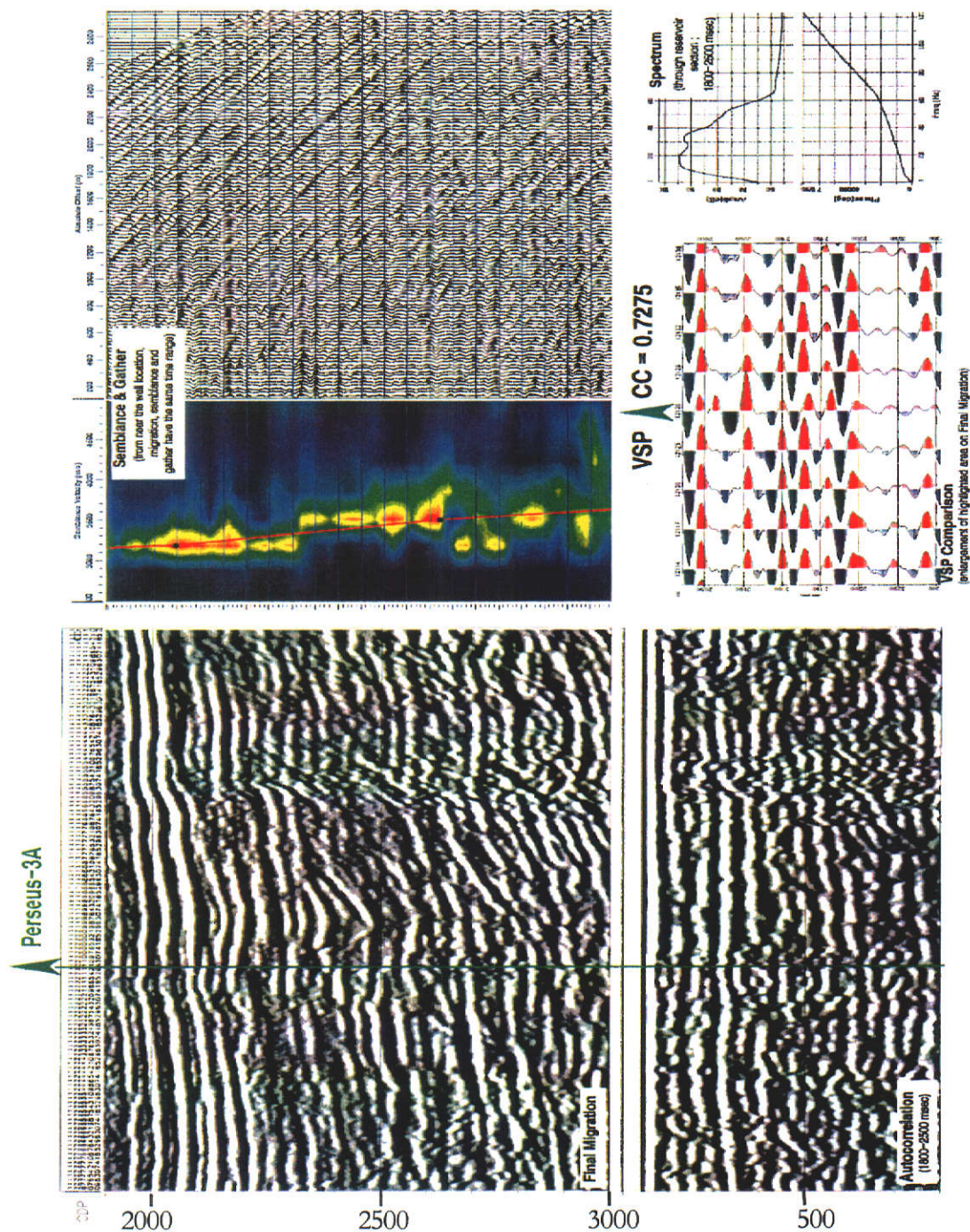
Figure (4.6) The result after the application of gapped deconvolution followed by Radon Demultiple.

The semblence is not improved over GD alone. The Correlation Coefficient is low. Multiples are not very well attenuated.
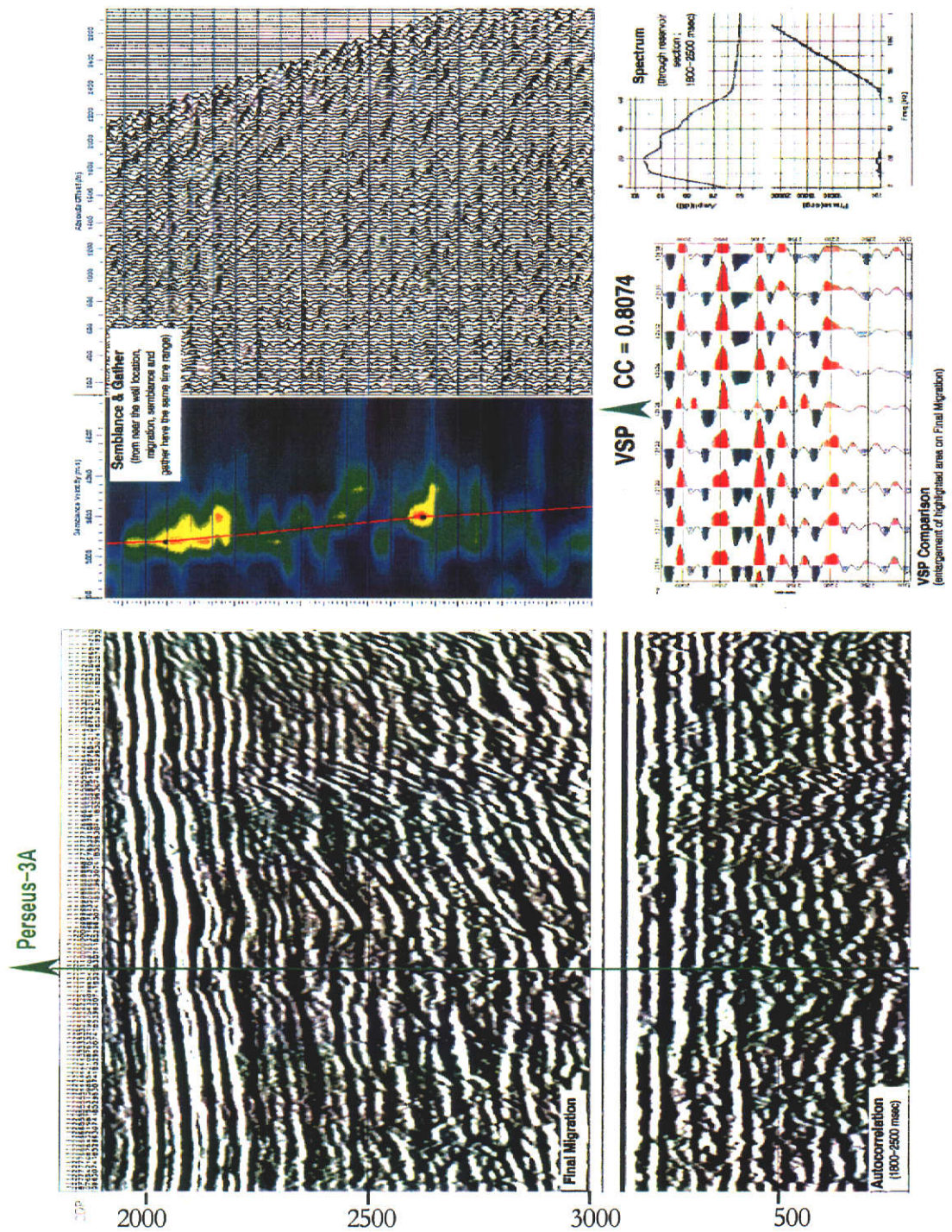
Figure (4.7) The result of autoconvolution in the MMO/ISR domain.

This is the result that the interpreters favour. The dipping energy on the right of the section is fairly strong. The correlation coefficient is the second highest of all the tests. The velocity picking is unambiguous.
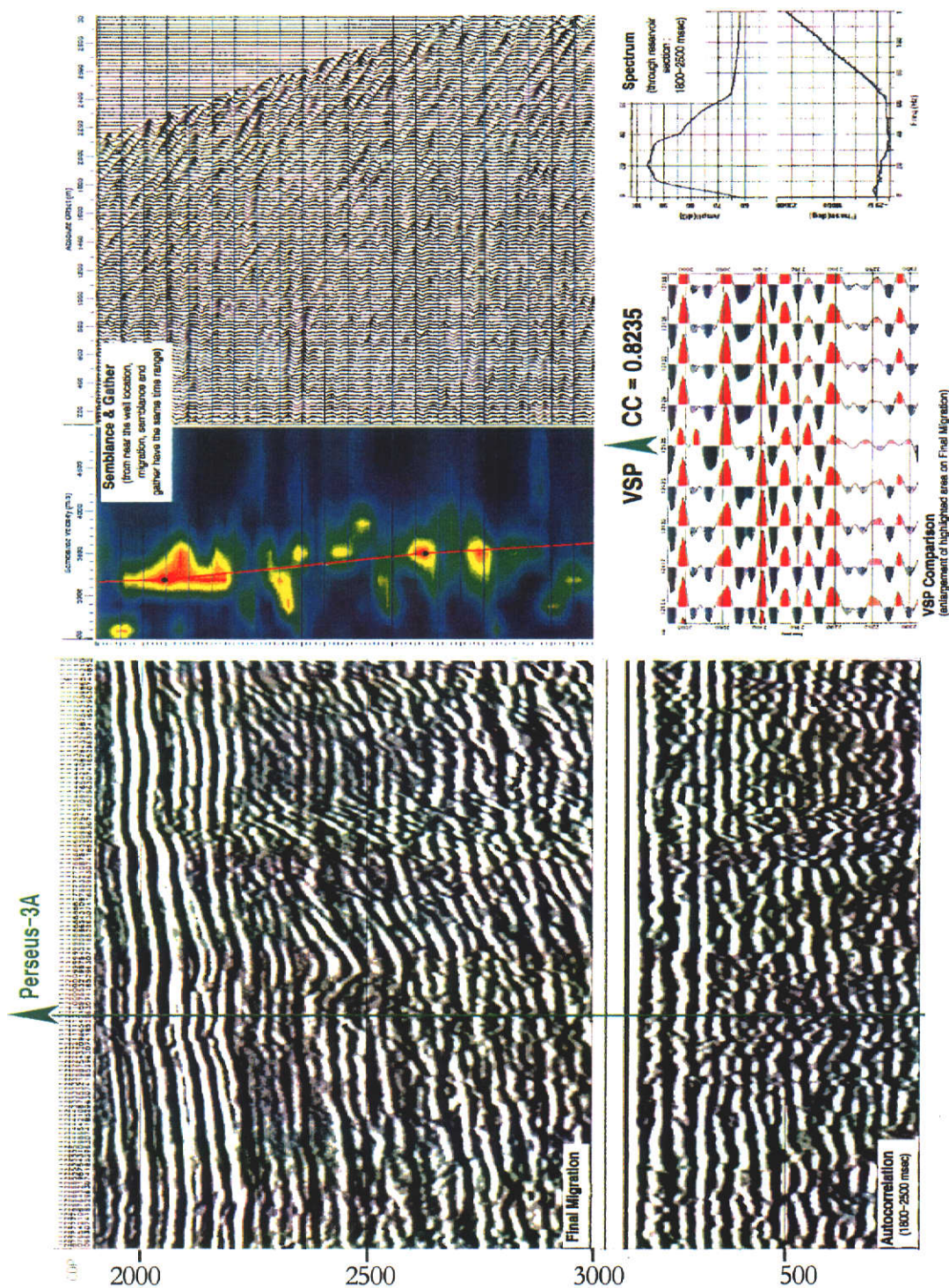
Figure (4.8) The result of gapped deconvolution in the MMO/ISR domain.

This procedure has the highest correlation coefficient with the VSP. The dipping events on the right of the section are fairly strong. The gather is not as noisy as that of MMO/ISR/autocon. Overall a very good result.

Summary

The best results were attained by using demultiple techniques in the MMO/ISR domain. A comprehensive set of tests has been displayed and compared in order to judge the effectiveness of the MMO/ISR preconditioning procedure. These tests included:

- No specific demultiple procedure (stack only) – control data.

- Gapped deconvolution in the x-t domain.

- Radon demultiple.

- Gapped deconvolution followed by Radon Demultiple.

- MMO/ISR preconditioning followed by autoconvolution.

- MMO/ISR preconditioning followed by gapped deconvolution.

The Perseus data set is complex, and the multiple attenuation task here is very problematic. Differences in performance between the multiple attenuation methods are subtle but significant. The MMO/ISR/autocon results were judged to be the best both subjectively, after inspection by Woodside Interpreters familiar with the area, and objectively when matched against a VSP from the Perseus 3A well (it had the second highest correlation coefficient - MMO/ISR/GD had the highest).

This first case study shows that the new pre-conditioning transforms enable a more effective removal of multiple energy than standard techniques.

Conclusions and Recommendations

In Chapter (1) we noted the characteristics of an ideal demultiple technique which will perform effectively under Western Australian conditions:

- requires no velocity model,
- removes the multiples early in the processing sequence,
- works in shallow water depths,
- preserves primary reflection amplitudes,
- and is affordable.

A new pair of transforms have been developed; the MMO and ISR transforms. These transforms can precondition pre-stack data, for both horizontal and dipping sea floors, so that it resembles zero offset traces from a 1D earth. The water layer multiples are made periodic and their wavelets stationary (constant spectral content) down each pre-stack trace.

After data preconditioning with MMO/ISR, the water bottom multiples are well prepared for attenuation using either predictive deconvolution or autoconvolution. Predictive deconvolution is more suitable for removing shorter period multiples.

Autoconvolution is more suited to the removal of longer period multiples in the MMO/ISR domain.

The new preconditioning procedure developed is a major advance in achieving the objectives of multiple attenuation. It is a simple procedure, which has been shown to be effective on both synthetic and field data. It is readily incorporated into any commercial processing sequence.

The results of the new techniques have been tested on both synthetic and field data and found to be consistently better than other commercially available techniques. Both simple water bottom multiples and water bottom peg leg multiples have been attenuated.

The assumptions of the procedures are:

- the sea floor is linear and consistent over the spread length,
- the dataset is truly a 2D dataset.

Few parameters are required and they are easily determined to the required accuracy.

Two major recommendations for future work have arisen: 1) further research to continue the work to generalise the preconditioning MMO and ISR transforms to 3D; 2) extensive work on further testing the routines on field data from different geological settings to reveal the full extent of commercial applicability.

References

Alam, A. and Austin, J., 1981, Multiple suppression using slant stacks: Tech. Rept., Western Geophysical Company.

Anstey, N. A., 1966, The sectional autocorrelogram and the sectional retrocorrelogram: Geophys. Prosp., 14, 389-411.

Backus, M. M., 1959, Water reverbations – their nature and elimination: Geophysics, 24, 233-261.

Benoliel, S. D., Schneider, W. A. and Shurtleff, R. N., 1987, Frequency wavenumber approach of the τ-p transform: Some applications in seismic data processing: Geophys. Prosp., 35, 517-538.

Berkhout, A. J. 1987, Applied seismic wave theory: Elsevier Science Publ. Co., Inc.

Bernth, H. and Sonneland, L., 1983, Wavefield extrapolation techniques for prestack attenuation of water reverberations: 53rd Ann. Internat. Mtg., Soc. Explor. Geophys., Expanded Abstracts, 264-265.

Berryhill, J. R. and Kim, Y. C., 1986, Deep-water peg legs and multiples: Geophysics, **49**, 2177-2184.

Born, M. and Wolf, E., 1964, Principles of optics: New York, Pergamon Press.

Calvert, A. J., 1990, Ray-tracing-based prediction and subtraction of water-layer multiples: Geophysics, **55**, 443-451.

Carrion, P. M., 1986, A layer-stripping technique for suppression of water-bottom multiple reflections: Geophys. Prosp., **34**, 330-342.

De Pledge, D. R. and Uren, N. F., 1993, Practical application of the event prediction method of multiple attenuation on marine seismic data: Dept Expl. Geophys., Curtin University of Technology internal report, SPS / 586 / 1993 / EG22.

Diebold, J. B. and Stoffa, P. L., 1981, The traveltime equation, tau-p mapping, and inversion of common midpoint data: Geophysics, **46**, 238- 254.

Downie, S. P., Hartley, B. M. and Uren, N. F., 1995, Interactive attenuation of seismic multiples in the radial domain: Expl. Geophys., **26**, 486-492.

Dragoset, W. H. and Jericevic, Z., 1997, Some remarks on surface multiple attenuation: Geophysics, **63**, 772-789.

Embree, P., Burg, J. P. and Backus, M. M., 1963, Wide-band velocity filtering – The pie-slice process: Geophysics, **28**, 948-974.

Foster, D. J. and Mosher, C. C., 1992, Suppression of multiple reflections using the Radon transform: Geophysics, **57**, 386-395.

Gibson, B. and Larner, K., 1984, The Predictive deconvolution and the zero-phase source: Geophysics, **49**, 379-397.

Graul, M., 1998, Deconvolution: Short Course Notes.

Haase, A. B., 1992, Slope data water-bottom multiple attenuation: Geophys. Prosp., **40**, 403-428.

Hampson, D., 1986, Inverse velocity stacking for multiple elimination: Can. Soc. Expl. Geophys., **22**, 44-55.

Hardy, R. J. J. and Hobbs, W. H., 1991, A strategy for multiple suppression: First Break, **9**, 139-144.

Hartley, B. M. and Lamont, M. G., 1996, Some mathematical relationships amongst seismic surface multiple reflections: Curtin University of Technology internal report, SPS 669 / 1996 / EG 62.

Hartley, B. M., 1998, Calculation of Take-off and Arrival Angles of Seismic Signals for Source and Receiver for Water Bottom Seismic Muliples and Relations to MMO and ISR Transforms: Curtin University of Technology internal report, SPS 698 / 1998 / EG 77.

Haskey, P. and Ashdown, J., 1991, Transform techniques applied to the attenuation of long period multiples: Expl. Geophys., 22, 165-168.

Kappus, M. E., Harding, A. J. and Orcutt, J. A., 1990, A comparison of tau-p transform methods: Geophysics, 55, 1202-1215.

Kneib, G. and Bardan, V., 1997, 3D targeted multiple attenuation: Geophys. Prosp., 45, 701-714.

Kunetz, G., 1961, Essai d'analyse de traces seismiques: Geophys. Prosp., 9, 312-341.

Kunetz, G. and Fourmann, J. M., 1968, Efficient deconvolution of marine seismic records: Geophysics, 33, 412-423.

Lamont, M. G. and Uren, N. F., 1995, A method for the removal of long period surface related multiples: Expl. Geophys., 26, 477-481.

Lamont, M. G. and Uren, N. F., 1997, Multiple elimination using wavefield transformations off the coast of Western Australia: The APPEA Journal, 777-785.

Levin, F. K., 1971, Apparent velocity from dipping interface reflections: Geophysics, 36, 510-516.

Levin, S. A., 1987, Deconvolution with spatial constraints: Ph.D. thesis, Stanford University.

Levin, F. K. and Shah, P. M., 1977, Pegleg multiples and dipping reflectors: Geophysics, 42, 957-981.

Lokshtanov, D. and Sagehaug, A., 1995, Multiple suppression by deconvolution in the tau-p domain: Presented at the 57th Mtg., EAGE, Glasgow, Scotland.

Loewenthal, D., Lu, L., Robertson, R. and Sherwood, J., 1974, The wave equation applied to migration and water bottom multiples: Presented at the 36th Mtg., Eur. Assn. Expl. Geophys.

Manin, M. and Spitz, S., 1995, 3-D extraction of a targeted multiple: 65th Ann. Internat. Mtg., Soc. Expl. Geophys., Expanded Abstracts, 1468-1469.

Marfurt, K. J., Schneider, R. V. and Mueller, M. C., 1996, Pitfalls of using conventional and discrete radon transforms on poorly sampled data: Geophysics, 61, 1467-1482.

Mayne, W. H., 1962, Common reflection point horizontal data stacking techniques: Geophysics, 27, 927-938.

Mayne, W. H., 1967, Practical considerations in the use of common reflection point techniques: Geophysics, 32, 225-229.

McGillem, C. D. and Cooper, G. R., 1991, Continuous & discrete signal & system analysis: Saunders College Publishing, third edition.

Morley, L., 1982, Predictive techniques for marine multiple suppression: Ph.D. dissertation, Stanford University.

Morley, L. and Claerbout, J., 1983, Predictive deconvolution in shot-receiver space: Geophysics, 48, 515-531.

Peacock, K. L. and Treitel, S., 1969, Predictive deconvolution: Theory and Practice: Geophysics, 34, 155-169.

Riley, D. C. and Claerbout, J. F., 1976, 2-D multiple reflections: Geophysics, 41, 592-620.

Robinson, E. A., (1984), Seismic inversion and deconvolution, Part A: Classical Methods: Geophysical Press, London, Amsterdam.

Russell, B., Hampson, D. and Chun, J., 1990, Part 2: Noise elimination and the Radon transform: The Leading Edge, 31-37.

Schoenberger, M., 1996, Optimum weighted stack for multiple suppression: Geophysics, 61, 891-901.

Schneider, W. A., Prince, E. R. and Giles, B. F., 1965, A new data-processing technique for multiple attenuation exploiting differential normal moveout: Geophysics, 30, 348-362.

Sheriff, R. E., 1991, Encyclopedic dictionary of exploration geophysics: Soc. Expl. Geophys., 2nd Ed., 154-155.

Silverman, D. and Sparks, N. R., 1965, Some experiments on multiple reflection cancellation: Geophysics, 30, 1085-1093.

Sinton, J. B., Ward, R. W. and Watkins, J. S., 1978, Suppression of long-delay multiple reflections by predictive deconvolution: Geophysics, 43, 1352-1367.

Smith, W. O., 1958, Recent underwater surveys using low frequency sound to locate shallow bedrock: Geol. Soc. America Bull., 69, 69-98.

Taner, M. T., 1980, Long-period sea-floor multiples and their suppression: Geophys. Prosp., 28, 30-48.

Taner, M. T., O'Doherty, R. F. and Koehler, F., 1995, Long period multiple suppression by predictive deconvolution in the x-t domain: Geophys. Prosp., 43, 433-468.

Taylor, H. L., Banks, S. C. and McCoy, J. F., 1979, Deconvolution with ℓ_1 norm: Geophysics, 44, 39-52.

Thorson, J. R. and Claerbout, J. R., 1985, Velocity-stack and slant-stack stochastic inversion: Geophysics, 50, 2727-2741.

Treitel, S., Gutowski, P. R. and Wagner, D. E., 1982, Plane-wave decomposition of seismograms: Geophysics, 47, 1375-1401.

Tsai, C. J., 1985, Use of autoconvolution to suppress first-order, long-period multiples: Geophysics, 50, 1410-1425.

Verschuur, D. J., 1991, Surface related multiple elimination, an inversion approach: Ph.D. thesis, Delft University of Technology.

Watson, R. J., 1965, Decomposition and suppression of multiple reflections: Geophysics, 30, 54-71.

Wiggins, J. W., 1988, Attenuation of complex water-bottom multiples by wave-equation-based prediction and subtraction: Geophysics, 53, 1527-1539.

Yang, M., 1989, Multiple suppression by optimized fold reduction: Geophysics, **54**, 1448-1454.

Yergin, D., 1996, The prize the epic quest for oil: Simon & Schuster.

Yilmaz, O., 1987, Seismic data processing: Soc. Expl. Geophys., Tulsa.

Zhou, B. and Greenhalgh, S. A., 1994, Wave-equation extrapolation-based multiple attenuation: 2-D filtering in the *f-k* domain: Geophysics, **59**, 1377-1391.

Appendix A

Curtin University of Technology

SCHOOL OF PHYSICAL SCIENCES

SOME MATHEMATICAL RELATIONSHIPS AMONGST SEISMIC SURFACE MULTIPLE REFLECTIONS

By

B.M. Hartley
Department of Exploration Geophysics
[hartley@geophy.curtin.edu.au]

and

M. Lamont
Woodside Petroleum
1 Adelaide Terrace, Perth, WA

28 March, 1996.

Abstract

Seismic exploration is one of the principal techniques used in the search for oil and gas. The technique involves the analysis of echoes which are reflected in the earth following the generation of a characteristic signal at the surface. Energy will be reflected from geological interfaces many times. The primary reflection is the desired signal but this will always be accompanied by multiple reflections. When the multiple reflections have amplitudes similar to the deeper primary events they need to be removed during processing.

When seismic exploration is conducted at sea, the presence of a hard sea floor and a highly reflective air-water interface combine to produce strong reverberations within the water layer. These multiple reflections from the sea-bed appear to arrive from deeper layers than the reflecting surface and can intefere with the interpretation of the interesting layers at depth. A number of techniques can be used to identify and attenuate these multiples but it is necessary to understand the mathematical relationships between them in order to deal with them.

The simple relationships between multiples are known but some techniques of seismic analysis require more advanced analysis to extract meaningful data from seismic record with multiple reflections. As some of the mathematical relationships are complex the symbolic mathematical package Maple can be used to solve the equations and plot the results.

In this paper we describe the basic equations for multiple surface seismic reflections and derive some useful mathematical relationships which may assist in processing and interpretation of seismic data containing multiple reflections.

1. INTRODUCTION

When conducting seismic exploration at sea the presence of a strongly reflecting sea floor combined with the reflective sea-air interface has the effect of producing strong multiple reflections within the sea layer. These strong multiple reflections result in signals in the seismic record which appear to arrive from a greater depth than the sea floor and can confuse or obscure reflected signals from real structures at the same apparent depth.

At sea a recording cable containing hydrophones at equal spacings, is towed behind a ship. A seismic source, also towed behind the ship, is fired automatically by the navigation system. This helps ensures that the shot points and the hydrophone positions at the instant of firing, maintain a constant geometry. Data obtained in this way is known as the shot record. In seismic exploration a series of shot records is taken with the source and receivers in different locations.

The shot record represents the data as it is gathered in the field and is thus the raw data for seismic interpretation. The source-receiver distance is termed the offset and geophones record the reflected waves at various values of offset. The source and the receivers are coincident when the offset is zero but this is an unrealisable condition. When the source and the receiver are not coincident instrumental and geometrical factors can influence the recording of the signal. It is sometimes necessary to transform or re-sample data along suitable lines with constancy in a particular parameter in order to eliminate such effects.

The seismic record comprises the digitised signals recorded from each geophone following the generation of the signal at the surface. For each geophone the time series of the recorded signal is termed a trace, but the term may also be used for different lines constructed on the seismic record or following its transformation to different coordinates.

The derivations of the equations describing reflections from a sloping sea floor in a shot record resulting from a signal originating at the sea surface are well established [7][6]. These are known as the time-distance relationships.

$$t_n^2 = \frac{t_{0p}^2}{\sin^2 \alpha} \sin^2 n\alpha + \frac{x^2}{v^2} - \frac{2xt_{0p}}{v \sin \alpha} \sin^2 n\alpha \tag{1}$$

where t_n is the travel time of the ray reflected n times from the sea floor, t_{0p} is the two way travel time perpendicular to the sea floor, from the origin of the signal at the surface, α is the angle of slope of the sea floor, x is the distance along the surface of the sea to the point of arrival of the signal and v is the velocity of sound in the medium [1].

The above equation represents a set of hyperbolae which are asymmetric about the t

A2

axis. These hyperbolae represent what is called the shot record of seismic data.

It has been found to be advantageous in seismic interpretation to form a representation of the data in which the source and the receiver are coincident. Such a representation, is known as the Common Mid Point or CMP stack. A CMP stack for a given point is formed by selecting traces which have equal magnitudes of offset for the source and the receiver, but have opposite sign. Summing such traces following travel time correction, enhances common features in the seismic record and overcomes difficulties of having the source of seismic signal and the receiver at the same location. If the reflecting layer is horizontal the CMP representations have a common reflecting point directly below the source. If, however the reflecting layer is sloping the CMP representation only approximates a reflection from a common point below the signal source [7].

Multiple reflections in CMP representations have a parallel mathematical form to those for the shot record [7]

$$t_n^2 = \frac{t_{0p}^2}{\sin^2 \alpha} \sin^2 n\alpha + \frac{x^2}{v^2} \cos^2 n\alpha. \tag{2}$$

Again this equation represents a set of hyperbolae but these are symmetrical about the t axis. The symbols have the same meaning as for equation 1 except that t_{0p} is the travel time to the sea floor from the mid point between the source and the receiver.

2. NORMALISATION OF EQUATIONS

It will be useful in the later analysis to normalise and simplify equations 1 and 2. This can be achieved by defining new variables which give convenient scalings for the axes. For the shot record (equation 1) we define new variables

$$
\begin{aligned}
l &= 2t_n \sin \alpha / t_{0p} \\
\chi &= 2x \sin \alpha / t_{0p} v
\end{aligned}
\tag{3}
$$

and for the CMP gather (equation 2

$$
\begin{aligned}
l &= t_n \sin \alpha / t_{0p} \\
\chi &= x \sin \alpha / t_{0p} v
\end{aligned}
\tag{4}
$$

We can also replace $n\alpha$ with θ and then the equation for the shot records becomes;

$$l^2 = 4\sin^2 \theta + \chi^2 - 4\chi \sin^2 \theta, \tag{5}$$

A3

and for the CMP representation;

$$l^2 = \sin^2 \theta + \chi^2 \cos^2 \theta. \tag{6}$$

As with equations 1 and 2 these equations represent sets of hyperbolae now in parameter θ. These equations are now normalised. For the shot record and the CMP gather the family of hyperbolae now intersect at the pinch out point at $\chi = 1, l = 1$ These are shown in Figures 1 and 2. For the shot record hyperbolae only the functions in the first two quadrants are shown. There are of course similar hyperbolae in the third and fourth quadrants, which are the mirror images of the ones in the first two quadrants. It is noted that the hyperbolae from the shot record are asymmetrical about the l axis.

The hyperbolae for the CMP representation of the multiples are symmetrical about the l axis and are shown plotted in the first quadrant in Figure 2.

In further analysis we will work with the normalised equations for mathematical convienience but will make the appropriate substitutions to reform equations in familiar terms

Maple code for plotting the curves of Figures 1 and 2 is included below.

```
#Plot CMP Hyperbolae
restart:
eqn:=T^2=(t[0]^2*sin(n*alpha)^2)/sin(alpha)^2 +x^2*cos(n*alpha)^2:
alpha:=arcsin(s):
L:=sqrt(rhs(eqn)):
t[0]:=s:n:=theta/alpha:
L:=subs(theta=psi/15,L):
Hyper:=[x,L,x=0..1]$psi=0..15:
plot(Hyper,0..1,0..1,color=BLACK, thickness=1);
#Plot Shot Record Hyperbolae
restart:
eqn:=T^2=(t[0]^2*sin(n*alpha)^2/sin(alpha)^2 + x^2
- 2*t[0]*x*sin(n*alpha)^2/sin(alpha)):
alpha:=arcsin(s):
L:=sqrt(rhs(eqn)):
t[0]:=s:n:=theta/alpha:
L:=subs(theta=psi/15,L):
```

```
Hyper:=[x,L,x=-1..1]$psi=0..15:
plot(Hyper,-1..1,0..2,color=BLACK, thickness=1);
```

3. MULTIPLE MOVEOUT

In seismic processing, time series analysis is an important means to assist in untangling the useful data from the noise and unwanted signals. Multiple reflections from the sea floor would be more easily recognised if they occurred at regular periodic intervals. If this were the case they would be amenable to removal by autoconvolution and/or predictive deconvolution techniques [2]. In general, however, multiple reflections do not occur periodically and a transformation of the data may be required in order to achieve periodicity.

Where the sea floor has zero slope, multiple reflections in the shot record and in the CMP representations of the data are periodic along straight lines radiating from the origin [8]. It is therefore possible to transform the data into a space where the multiples are periodic by resampling the data along those straight line radial traces. Where the sea floor has non zero slope the periodicity is lost.

It is, however, possible to rescale the data in a number of ways which will produce periodicity. One such way is to employ a technique termed multiple move out (MMO) [5]. MMO renders the multiple reflections from the sea floor as a set of horizontal events which are equally spaced. Uniform periodicity is thereby gained in all traces. Following MMO, time domain radial traces are also evidently periodic with differing periods along the different radials.

The MMO transform can be obtained by separating the term $\theta = n\alpha$ from equation 5 above. So;

$$\theta = n\alpha = \arcsin\left(1/2\sqrt{\frac{(l^2 - \chi^2)}{1 - \chi}}\right) \tag{7}$$

If we now make the substitutions from equations 3 into the above we get the MMO transformation equations in terms of the variables used in equation 1 i.e.

$$\theta = n\alpha = \arcsin\left(\sin(\alpha)\sqrt{\frac{t_n^2 v^2 - x^2}{t_{0p} v \left(t_{0p} v - 2 x \sin(\alpha)\right)}}\right) \tag{8}$$

A5

In the limit where $\alpha = 0$ the above equation simplifies to;

$$n = \sqrt{\frac{t_n^2 v^2 - x^2}{t_{0p}^2 v^2}}$$

(9)

{Simplify this} These equations can be shown to be the same as those derived by Lamont and Uren [5]. They are applied by considering any point in the x, t_n space of the shot record. For each such point we calculate new values of χ from equations 3 and θ or $n\alpha$ from 8. If the values of t_{0p} and α have been correctly assigned the multiple events will appear periodically on a plot of χ versus θ, at integral multiple values of α, or of n if $\alpha = 0$.

Similar transforms can be derived for the CMP representations using equation 6 and solving for $\theta = n\alpha$ gives

$$\theta = n\alpha = \arcsin\left(\sqrt{\frac{(l^2 - \chi^2)}{1 - \chi^2}}\right)$$

(10)

Making the substitution from equation 4 we get the MMO equations for a CMP gather in term of the symbols commonly used in geophysics.

$$\theta = n\alpha = \arcsin\left(\sin(\alpha)\sqrt{\frac{-t^2 v^2 + x^2}{x^2 (\sin(\alpha))^2 + t_{0p}^2 v^2}}\right)$$

(11)

{Simplify this} In the limit of $\alpha = 0$ the transformation for the CMP representaion is the same as for the shot record given in equation 9 above.

4. ISO-STRETCH CURVES

Whilst the MMO transformation makes the multiple reflections equally spaced horizontal events it introduces differential stretch into the traces [6]. This means that signals in the seismic record will be distorted and, therefore, will only exactly match the signals in other parts of the record where the amount of stretch is the same. Stretch makes autoconvolution and predictive deconvolution ineffective.

To overcome this it would be useful to resample the data by following the curves of equal stretch whilst maintaining the periodicity obtained through the MMO transformation. Such resampling is a common technique in seismic processing and effectively transforms the record into a space which exhibits the properties which are required.

Two representations of the 'iso-stretch' curves are possible. One drawn on the seismic record before the MMO transformation and the other following the MMO transformation. The curves of iso-stretch are those curves in which the rate of change of l with changing values of n is constants. We can therefore start with equation 7 and differentiate with respect to l. We equate this differential with a constant C, square the equation and solve for χ^2. This yields an equation for constant values of stretch in terms of the normalised variables χ and l.

The equation for the iso-stretch curves represented on a seismic shot record before MMO is applied is

$$l^2 = \frac{C^2 \left(l^2 - \chi^2 + 2\chi\right)^2}{(4\,C^2 - 1)} \tag{12}$$

in the normalised coordinates defined above, or

$$t^2 = 4\frac{\left(\dfrac{x^2 \sin(\alpha)}{t_{0p} v^2} - \dfrac{t^2 \sin(\alpha)}{t_{0p}} - \dfrac{x}{v}\right)^2 C^2}{(4\,C^2 - 1)} \tag{13}$$

in the coordinate system of the original shot record. These should be compared with equations 5 and 1 respectively.

The iso-stretch curves so derived are shown in Figure 3 overlayed on the hyperbolae of the shot records. The differentiation and plotting are most easily done by employing a symbolic mathematics package such as Maple and a code for performing this manipulation and plotting is as follows.

```
restart:
eqn:=1=sqrt(4*sin(theta)^2+x^2-4*x(sin(theta)^2):
solve(eqn,theta):
Thet:=sort("[1]):
dTdl:=diff(Thet,1):
solnx:=solve(dTdl^2=C^2,x):
Isostretch1:=[solnx[4],1,l=0..lrange]:
Isostretch2:=[solnx[2],1,l=0..lrange]:   # Choose the two
solutions which give curves in the correct quadrants
ShotCurve:=[x,sqrt(rhs(eqn)),x=0..xrange]:
xrange:=1:lrange:=1:
```

```
C:=1/(2*sin(2*theta)):
#Makes diagram symmetric about y=1-x (not hard to prove)
theta:=(Pi/48)*j:
#Pick some nice values of theta to plot with
L:=ShotCurve $ j=1..11:
# Prepare to plot Shot Curves
G1:=Isostretch1 $ j=1..11:
G2:=Isostretch2 $ j=1..11:
# Prepare to plot Isostretch Curves
plot({G1,G2,L},0..xrange,0..lrange,color=BLACK);
# Below:  Maple proof that the diagram can be made symmetric
(and that C=1/(2*sin(2*theta)) is the correct value to do it.
theta:='theta':  C:='C':
fn1:=ShotCurve[2]:
fn2s:=Isostretch[1]:
fn2:=1-subs(y=1-x,fn2s):
# This reflects the curve x=fn2s(y) around the line y=1-x
fn1=fn2:
# Let's solve this.  If the soln doesn't depend on x,
# it means the diagram can be made symmetric.
sqrq("):
addq(",-op(")[2]):
collect(",x):
solve("):
# We ignore the x=1 case, and also the case where C is negative.
Thus the solution is
C=sqrt(1/(sin(theta)^2*cos(theta)^2))/4:
# Which if sin(theta) and cos(theta) are positive, becomes
C=1/(4*sin(theta)*cos(theta)):
# Which is
C=1/(2*sin(2*theta)):
```

The iso-stretch curves drawn in Figure 3 have values of $C = 1/2\sin(2\theta)$. These values of C are chosen to illustrate the symmetry of the shot record hyperbolae and the iso-stretch curves. It can be shown that they are in fact the same curves but reflected about

the line $\chi = 1 - l$. We can demonstrate that the equations are the same and derive the parameterisation in C required to make them appear the same by using Maple. A demonstration and derivation is as shown above.

The alternative representation is to plot the curves of iso-stretch on the multiple traces following the MMO transformation. Such a plot is shown as figure 4. Again this is most conveniently done using a package such as Maple and the code used to generate the figure is given below.

```
restart:
eqn:=l = sqrt(4*sin(theta)^2+x^2-4*x(sin(theta)^2):
dldThet:=diff(rhs(eqn,theta)):
Stretch:=solve(dldtheta^2=C^2,x):
Isostretch1:=[Stretch[1],theta,theta=0..Pi/2]:
Isostretch2:=[Stretch[2],theta,theta=0..Pi/2]:
C:=j/10:
Graf1:=Isostretch1 $j=1..18:
Graf2:=Isostretch2 $j=1..18:
plot({Graf1,Graf2},x=0..1,theta=0..1.5,color=BLACK);
```

The iso-stretch curves as calculated and plotted above have the functional form

$$\chi = 1 + \frac{C \sin 2\,\theta \sqrt{4 - C^2} - C^2 \cos(2\,\theta)}{C^2 + 2 \, \cos(4\,\theta) - 2} \tag{14}$$

when drawn in the coordinate system following MMO. In this instance the equation is a function of θ. This can be put in terms of the order of the multiple and the angle of dip by remembering that $n\alpha = \theta$. The functions so generated are universal for all values of α and it is simply a matter of normalising the curves to utilise the universal equations

Similar transformations may be used in the CMP representations of seismic data.

The method of finding the equations for the isostretch curves in the CMP representations is the same as for the shot records. We start with equation 10 and differentiate with respect to l. This is equated to a constant and solved for χ. After simplification the equation for the iso-stretch curves is

$$l^2 = C^2 \left(l^2 - 1\right) \left(\chi^2 - l^2\right) \tag{15}$$

for the normalised coordinate system before MMO is applied (Figure 5)and is

$$t_n{}^2 = \left(\frac{t_n{}^2\left(\sin(\alpha)\right)^2}{t_0{}^2} - 1\right)\left(-t_n{}^2 + \frac{x^2\left(\sin(\alpha)\right)^2}{t_0{}^2 v^2}\right)C^2 \tag{16}$$

in the unnormalised system represented by equation 2.

These equations should be compared with equations 6 and 2 respectively.

Figures 5 shows the isostretch curves for the CMP representations superimposed on the hyperbolae which represent the multiple reflections. Maple code to derive this solution and to plot it is given below.

```
restart:
eqn:=1=sqrt(sin(theta)^2+x^2*cos(theta)^2):
solve(eqn,theta):
Thet:=sort("[1]):
dTdl:=diff(Thet,l):
solnx:=solve(dTdl^2=C^2,x):
Isostretch:=[solnx[2],l,l=0..lrange]:
CMPCurve:=[x,rhs(eqn),x=0..xrange]:
xrange:=1:lrange:=1:
C:=1/sin(theta):
theta:=(Pi/24)*j:
#Pick some nice values of theta to plot with
L:=CMPCurve $ j=1..11:   # Prepare to plot CMP Curves
G:=Isostretch $ j=1..11:   # Prepare to plot Isostretch Curves
plot({G,L},0..xrange,0..yrange,color=BLACK,numpoints=1001);
```

For the coordinate system following MMO we start with equation 6 and differentiate it with respect to θ. After solving for χ and simplification the isostretch curves are

$$\chi^2 = 1 + \frac{2\,C^2\left(\cos(\theta)\right)^2 - 2\,C\sqrt{\left(\sin(2\,\theta)\right)^2 + \left(\cos(\theta)\right)^4 C^2}}{\left(\sin(2\,\theta)\right)^2} \tag{17}$$

Figure 6 shows the form of these isostretch curves following MMO. A Maple routine for deriving the above equation and for plotting the isostretch curves is given below.

```
restart:
eqn:=1=sqrt(sin(theta)^2+x^2*cos(theta)^2):
```

```
dldThet:=diff(rhs(eqn),theta):
solnx:=solve(dldThet^2=C^2,x):
Isostretch:=[solnx[3],theta,theta=0..Pi/2]:
xrange:=1:lrange:=1:
C:=j/10:
Graf:=Isostretch $ j=1..10:  # Prepare to plot Isostretch Curves
plot({Graf,L},x=0..xrange,theta=0..1.5,color=BLACK,numpoints=1001);
```

5. RADIAL TRACES

As indicated above, a transformation of seismic data to the radial trace domain can often assist in processing by restoring periodicity and improving the effectivness of auto-convolution or predictive deconvolution methods. For a sea floor with zero dip, radial traces intersect the multiple reflections periodically. With non-zero slope of the sea floor that periodicity is lost. It would be useful to recover that periodicity whilst retaining other properties of the radial traces.

In the case of dipping sea floor the radial traces must be curved to preserve periodicity of the multiples and are, therefore, not true radials. Periodicity can be obtained by following curves which trace out an equal distance along the traces for equal changes in the parameter n, the multiple order being followed. The case for CMP gathers will be treated first in this section as the mathematical manipulation is simpler. This method of tracing radials has been used by Downie for analysing CMP gathers [3].

A method of finding the solution for those radial traces is to first express the equation of the multiple reflections in parametric form. We start with equation 6 for the normalised CMP multiples and express it as a pair of equations in parameter $\tau(\theta)$, a function of θ.

$$l = \tau(\theta),$$
$$\chi = \frac{\sqrt{\tau(\theta)^2 - \sin^2\theta}}{\cos\theta}. \tag{18}$$

We can then express the square of the length of a vector in the l, χ space as

$$\left|\frac{d\kappa}{d\theta}\right|^2 = \left(\frac{d\chi}{d\theta}\right)^2 + \left(\frac{dl}{d\theta}\right)^2. \tag{19}$$

This vector must have a constant value C^2 for small changes in θ and we can form a

A11

differential equation in θ, $\tau(\theta)$, C and $\dfrac{dt}{d\theta}$. This equation can be solved using a symbolic mathematics package such as Maple.

The Maple code for solving and plotting the radials is included below and the curves generated are presented as Figure 7 superimposed on the CMP hyperbolae.

```
restart:
x:=sqrt(tau(theta)^2-sin(theta)^2)/cos(theta);
dxdn:=diff(x,theta);
l:=tau(theta);
dldn:=diff(l,theta);
dcdn2:=dldn^2+dxdn^2-C^2;
des:=solve(dcdn2,diff(tau(theta),theta));
Order:=8;
soln:=dsolve(des[1]=diff(tau(theta),theta),tau(0)=0,
tau(theta),series);
save soln,'tsoln2a';
```

and for plotting them

```
restart:
# Set up the shot hyperbolae to be plotted
eqn:=l=sqrt(sin(theta)^2+x^2*cos(theta)^2):
L:=subs(theta=alpha/10,rhs(eqn)):
Hyper:=[x,L,x=0..1]$alpha=1..7:
read 'tsoln2a':
# Read in the Solution from the previous Maple Session
tau(theta):=convert(rhs(soln),polynom):
limit:=array([1.0,1.0,1.0,1.0,1.2,1.2,1.2,1.2]):
# Some limits on the plotting range are required
x:=sqrt(tau(theta)^2-sin(theta)^2)/cos(theta):
l:=tau(theta):
C:=sqrt((tan(psi)^2+1)/(tan(psi)^2-1)):
psi:=(45+5.0*(ran))*Pi/180:
P:=[x,l,theta=0..limit[ran]]$ran=1..8:
plot({P,Hyper},offset=0..1.0,time=0..1.0,numpoints=1001,color=BLACK);
```

The solution to the differential equation which results from the above analysis is

$$\tau(\theta, C) = \frac{\sqrt{C^2+1}}{\sqrt{2}} \left(\theta - \frac{(3\,C^2-1)\,\theta^3}{12\,(C^2+1)} - \frac{(141\,C^6 - 71\,C^4 - 21\,C^2 - 33)\,\theta^5}{1440\,(C^2-1)\,(C^2+1)^2} \right.$$
$$\left. - \frac{(1713\,C^{10} - 5559\,C^8 + 7590\,C^6 - 6218\,C^4 + 105\,C^2 + 1473)\,\theta^7}{120960\,(C^2-1)^2\,(C^2+1)^3} \right). \quad (20)$$

The solution was limited to terms of order 7 by the capabilities of Maple to handle long expressions.

With the solution for $\tau(\theta)$ given above we need to draw lines on the hyperbolae of the CMP gather and follow those lines for different values of take off angle.

We therefore need to know the relationship between take off angle and the constant C. This can be found by calculating the value of $dl/d\chi$ at the origin. Again this can be done by employing Maple and a code which calculates this is given below

```
restart:
read 'tsoln2a':
tau(theta):=convert(rhs(soln),polynom):
x:=sqrt(tau(theta)^2-sin(theta)^2)/cos(theta):
l:=tau(theta):
dxdt:=diff(x,theta):
dldt:=diff(l,theta):
dldx:=limit(dldt/dxdt,theta=0):
simplify(");
```

We find the following expressions

$$\tan(\psi) = \frac{\sqrt{C^2+1}}{\sqrt{C^2-1}}, \quad (21)$$

or

$$C = \frac{\sqrt{\tan(\psi)^2+1}}{\sqrt{\tan(\psi)^2-1}}, \quad (22)$$

where ψ is the take off angle measured from the χ axis.

It is noted that the method given here and described in more detail in [4] does not give accurate results for values of l and χ for all values of the angle of take-off from the origin. Where the take off angle is close to $\pi/2$ the solutions obviously deviate from the

A13

criterion of equal path lengths for equal changes in the value of θ. The importance of the errors due to the approximation can only be judged by applying the method to real data but the accuracy of the theoretical approximation can be found readily.

The Maple code to plot the error in series solution due to its truncation is given below

```
restart:
read 'tsoln2a':
lim:=array([2.0,1.97,1.97,1.90,1.86,1.9,1.9,1.9]):
tau(theta):=convert(rhs(soln),polynom):
l:=tau(theta):
x:=sqrt(tau(theta)^2-sin(theta)^2)/cos(theta):
dldt:=diff(l,theta):
dxdt:=diff(x,theta):
Kappa:=dldt^2+dxdt^2:
C:=sqrt((tan(psi)^2+1)/(tan(psi)^2-1)):
psi:=(45+5.0*(ran))*Pi/180:
Plot:=[theta,(Kappa/C^2-1)*100.0,theta=0..lim[ran]]$ran=1..8:
plot({Plot},'Theta (Radians)' = 0..0.5,'Percentage Error'
= -0.1..0.4,numpoints=1001,color=BLACK);
```

The errors which result from the application of this radial trace method are shown in Figure 8. This shows the percentage error in the approximation for values of θ from 0 to 0.5 and for take off angles between 85 degrees and 50 degrees. It is noted that the error is less than 0.1% for values of θ less than about 0.15 radians or 8 degrees. This is equivalent to over eight reflections from a sea floor dipping at one degree. In most practical situations the dip of the sea floor is less than 2 degrees and the approximation is expected to be valid up to about the fourth multiple for take off angles up to 85 degrees with higher accuracy at lower take off angles. The errors are plotted with the same range of values of take-off angle as for Figure 7 and so the two diagrams can be compared. The error departs from zero at the smallest value of θ for the largest value of take off angle of 85 degrees.

It can also be seen from Figure 7 that some areas of the seismic record are inaccessible for radial traces which start at the origin. This is particularly the case for near offset traces which cannot become part of a radial trace which starts at the origin. Part of the seismic record is thus lost to the processing using these radial traces.

In some cases the seismic record may be scaled by a constant factor in the time offset axes corresponding to changes in velocity of wave propagation or some other scaling factor. In any event it may be advantageous to plot radials on axes which are not normalised as they are in the above analysis. In this case the radials can still be drawn and will still be curved.

The analysis of the radials follows the same algorithm as before and the differential equation can be solved as before. The Maple code to find the solutions is included below. It is noted that there is only a small change from the code used to solve the normalised CMP gather.

```
restart:
x:=sqrt(tau(theta)^2-sin(theta)^2)/cos(theta):
dxdn:=diff(x,theta):
l:=tau(theta):
dldn:=diff(l,theta):
dcdn2:=K^2*dldn^2+dxdn^2-C^2:
des:=solve(dcdn2,diff(tau(theta),theta)):
Order:=6:
soln:=dsolve(des[1]=diff(tau(theta),theta),tau(0)=0,
tau(theta),series);
save soln,'tsoln2ka';
```

The solution to these equations is given below

$$
\tau(\theta, C, K) = \frac{\sqrt{C^2 + 1}}{\sqrt{K^2 + 1}} \left(\theta - \frac{(3\,C^2 - 2\,K^2 + 1)\,\theta^3}{6\,(K^2 + 1)\,(C^2 + 1)} \right.
$$
$$
\left. - \frac{\left[\begin{array}{l} \left(\left(156\,K^2 - 15\right) C^6 + \left(-236\,K^4 + 203\,K^2 - 38\right) C^4 \\ + \left(84\,K^6 - 228\,K^4 + 126\,K^2 - 3\right) C^2 + 3\,K^2 + 48\,K^6 - 84\,K^4\right) \end{array} \right] \theta^5}{360\,(K^2 + 1)^2\,(C^2 + 1)^2\,(C^2 - K^2)} \right). \qquad (23)
$$

With the small modification the series solution was limited by the capabilities of Maple to terms of order 5.

The application of this method in the unnormalised space, usually inhabited by geophysicists, can be readily achieved. Use is again made of the normalising equations 4. A value of C is chosen and a value of θ at which the coordinates t_n and x are to be calculated remembering that $\theta = n\alpha$. If a scaling factor K is to used this need to be chosen. The

values of C, θ and K are substituted into equation 20 or 23. A value of $\tau(\theta)$ is then calculated. From equations 4 we calculate the value of t_n, knowing the other parameters v, α and $t_0 p$. The value of x can then be determined from the inversion of equation 2 i.e.

$$\frac{x^2}{v^2} = \frac{t_n{}^2}{(\cos(n\alpha))^2} - \frac{4\,t_0 p^2\,(\sin(n\alpha))^2}{(\cos(n\alpha))^2\,(\sin(\alpha))^2} \tag{24}$$

The radial trace method can also be investigated for the shot records using the same method of analysis as for the CMP representation. In this case the parametric equations are;

$$
\begin{aligned}
l &= \tau(\theta), \\
\chi &= 2\sin(\theta)^2 \pm \sqrt{4\sin(\theta)^4 + \tau(\theta)^2 - 4\sin(\theta)^2}.
\end{aligned} \tag{25}
$$

Solution of the radial trace problem follows precisely the method use with the CMP representation except that two solutions of the radials must be kept as the system is not symmetrical.

The Maple code for solving the shot record radials is given below

```
restart:
eqn:=1^2=4*sin(theta)^2+x^2-4*x*sin(theta)^2:
l:=tau(theta):
x[1]:=simplify(solve(eqn,x)[1],radical):
x[2]:=simplify(solve(eqn,x)[2],radical):
dldt:=diff(l,theta):
dxdt:=diff(x[2],theta):
dcdt2:=dldt^2+dxdt^2-C^2:
des:=solve(dcdt2,diff(tau(theta),theta)):
Order:=7:
soln[1]:=dsolve(des[1]=diff(tau(theta),theta),tau(0)=0,
tau(theta),series):
dxdt:=diff(x[1],theta):
dcdt2:=dldt^2+dxdt^2-C^2:
des:=solve(dcdt2,diff(tau(theta),theta)):
soln[2]:=dsolve(des[1]=diff(tau(theta),theta),tau(0)=0,
tau(theta),series):
save soln,'shotradsol';
```

and the approximate solution is

$$\tau(\theta, C) = \frac{\sqrt{C^2 + 4}}{\sqrt{2}} \left(\theta \pm \frac{\sqrt{2}\sqrt{C^2 - 4}\theta^2}{C^2 + 4} - \frac{4\left(3C^2 + 5\right)\theta^3}{3\left(C^2 + 4\right)^2} \right.$$

$$\mp \frac{\sqrt{2}\left(C^6 - 16C^4 - 26C^2 - 64\right)\theta^4}{3\sqrt{C^2 - 4}\left(C^2 + 4\right)^3}$$

$$+ \frac{56\left(2C^8 - 10C^6 + 41C^4 - 57C^2 - 84\right)\theta^5}{45\left(C^2 - 4\right)\left(C^2 + 4\right)^4}$$

$$\left. \pm \frac{2\left(3C^{12} - 412C^{10} + 2582C^8 - 17560C^6 + 15876C^4 + 7680C^2 + 12288\right)\sqrt{2}\theta^6}{135\left(C^2 - 4\right)^{3/2}\left(C^2 + 4\right)^5} \right) \quad (26)$$

The upper positive or negative signs give the solution for the problem formulated with positive sign of the radical and the lower signs are appropriate for the solution with the negative sign in the radical in equation 24.

The solution of the equations with scaling factor K on the l axis is

$$\tau(\theta, C, K) = \frac{\sqrt{C^2 + 4}}{\sqrt{K^2 + 1}} \left(\theta \pm \frac{2\sqrt{C^2 - 4K^2}\theta^2}{\left(C^2 + 4\right)\sqrt{K^2 + 1}} \right.$$

$$- \frac{8\left(2K^2C^2 + 4K^2 + 1C^2 + 1\right)\theta^3}{3\left(C^2 + 4\right)^2\left(K^2 + 1\right)}$$

$$\mp \frac{2\left(\begin{array}{l} 16K^4C^4 - K^2C^6 + 32K^4C^2 + 16K^2C^4 \\ -C^6 + 64K^4 + 28K^2C^2 + 64K^2 - 8C^2 \end{array} \right)\theta^4}{3\left(K^2 + 1\right)^{3/2}\left(C^2 + 4\right)^3\sqrt{C^2 - 4K^2}}$$

$$\left. + 16\frac{\left[\begin{array}{l} 48K^6C^6 - 10K^4C^8 - 96K^6C^4 + 72K^4C^6 \\ -14K^2C^8 + 384K^6C^2 - 192K^4C^4 + 13K^2C^6 - 4C^8 + 384K^6 \\ +576K^4C^2 - 264K^2C^4 + 7C^6 + 768K^4 \\ -156K^2C^2 - 22C^4 + 24K^2 - 6C^2 \end{array} \right]\theta^5}{45\left(C^2 + 4\right)^4\left(K^2 + 1\right)^2\left(4K^2 - C^2\right)} \right) \quad (27)$$

where the sign relationship is as described above.

The relationship between the constant C and the take off angle ψ is

$$\tan\psi = \frac{\sqrt{C^2 + 4}}{\sqrt{C^2 - 4K^2}}, \quad (28)$$

or

$$C = \frac{2\sqrt{K^2 \tan(\psi)^2 + 1}}{\sqrt{\tan(\psi)^2 - 1}}. \tag{29}$$

The Maple codes to calculate these relationships follow the ones for the CMP representations.

Figure 9 is the overlay of the shot record radials on the shot record hyperbolae.

Figure 10 is a diagram of the errors caused by making a power series approximation to the 'radial' curve. The errors shown in Figure 10 are positive for the solution with the positive sign in the radical and the ones with negative error are for the negative sign in the radical of equation 20. The Maple codes for plotting the Figures 9 and 10 is included below.

```
restart:
eq:=1^2=4*sin(theta)^2+x^2-4*x*sin(theta)^2:
x[1]:=simplify(solve(eq,x)[1],radical):
x[1]:=subs(l=ln,x[1]):
x[2]:=simplify(solve(eq,x)[2],radical):
x[2]:=subs(l=lp,x[2]):
read 'shotradsol':
C:=2*sqrt((tan(psi)^2+1)/(tan(psi)^2-1)):
psi:=(45+5*ran)*Pi/180:
lp:=convert(rhs(soln[1]),polynom):
ln:=convert(rhs(soln[2]),polynom):
P:=[x[1],ln,theta=0..Pi/2]$ran=1..8:
N:=[x[2],lp,theta=0..Pi/2]$ran=1..8:
plot(Hyper,N,P,offset=-1.0..1.0,time=0.0..2.0,color=BLACK,
numpoints=1001);
```

and for the errors

```
restart:
eqn:=1^2=4*sin(theta)^2+x^2+4*x*sin(theta)^2:
read 'shotradsol':
limit:=array([0.5,1.0,1.0,1.0,1.0,1.0,1.0,0.2]):
C:=2*sqrt((tan(psi)^2+1)/(tan(psi)^2-1)):
psi:=(45+5.0*(ran))*Pi/180:
```

```
xsol:=solve(eqn,x):
tau(theta):=convert(rhs(soln[1]),polynom):
l:=tau(theta):
dldt:=diff(l,theta):
dxdtp:=diff(xsol[1],theta):
Kappap:=dldt^2+dxdtp^2:
Plotp:=[theta,(Kappap/C^2-1)*100.0,theta=0..limit[ran]]$ran=1..8:
tau(theta):=convert(rhs(soln[2]),polynom):
l:=tau(theta):
dldt:=diff(l,theta):
dxdtn:=diff(xsol[2],theta):
Kappan:=dldt^2+dxdtn^2:
Plotn:=[theta,(Kappan/C^2-1)*100.0,theta=0..limit[ran]]$ran=1..8:
plot(Plotp,Plotn,'Theta (Radians)' = 0..0.5,'Percentage Error'
= -1.0..1.0,numpoints=1001,color=BLACK);
```

The conversion to the unnormalised space represented by equation 1 follows precisely the path described for the case of the CMP representation. Use would be made of equations 3 and the inversion of 1 in terms of x i.e.

$$\frac{x^2}{v^2} = \frac{t_n{}^2}{(\cos(n\alpha))^2} - \frac{4\,t_0p^2\,(\sin(n\alpha))^2}{(\cos(n\alpha))^2\,(\sin(\alpha))^2}. \tag{30}$$

As shown above the series solution method does not give accurate results at values of θ above particular values determined by the take-off angle. Significant deviations from the expected curves can be seen in Figures 7 and 9 and the deviations are most evident when the take-off angle is close to $\pi/2$. It is possible to avoid some of these problems by solving the differential equations numerically and this can be done by the Runge-Kutta method included in the Maple package. A Maple code which solves the equation by a numerical method is included below.

```
restart:
eqn:=L=sqrt(sin(theta)^2+x^2*cos(theta)^2):
L:=subs(theta=alpha/10,rhs(eqn)):
Hyper:=[x,L,x=0..1]$alpha=1..7:
x:=sqrt(tau(theta)^2-sin(theta)^2)/cos(theta):
dxdn:=diff(x,theta):
```

A19

```
l:=tau(theta):
dldn:=diff(l,theta):
dcdn2:=dldn^2+dxdn^2-C^2:
des:=solve(dcdn2,diff(tau(theta),theta)):
points:=1000:
num:=8:
phi:=(45+5.0*ran)*Pi/180;
constants:=array([(sqrt((tan(phi)^2+1)/(tan(phi)^2-1)))
$ran=1..num]):
psi:=array([(n)$n=0..points]):
psi:=map((x)->x/points,psi):
jj:=1:
for jj to num do
C:=constants[jj]:
slope:=sqrt((C^2+1)/2):
sol[jj]:=dsolve(des[1]=diff(tau(theta),theta),tau(0)=psi[1],
D(t)(0) = slope,tau(theta),type=numeric, method = rkf45,value=psi):
od:
jj:=1:
for jj to num do
B[jj]:=array(1..2*points);
for ii to points+1 do
theta:=sol[jj][2,1][ii,1]:
tau(theta):=sol[jj][2,1][ii,2]:
B[jj][2*ii-1]:=evalf(l):
B[jj][2*ii]:=evalf(x):
od:
od:
plot(B[m]$m=1..8,Hyper,time=0..1,offset=0..1,
color=BLACK,numpoints=1000);
```
and for the shot record radials
```
restart:
eqn:=L=sqrt(4*sin(theta)^2+x^2-4*x*sin(theta)^2):
L:=subs(theta=alpha/10,rhs(eqn)):
```

A20

```
Hyper:=[x,L,x=-1..1]$alpha=1..7:
x:=2*sin(theta)^2+sqrt(4*sin(theta)^4+tau(theta)^2-4*sin(theta)^2):
dxdn:=diff(x,theta):
l:=tau(theta):
dldn:=diff(l,theta):
dcdn2:=dldn^2+dxdn^2-C^2:
des:=solve(dcdn2,diff(tau(theta),theta)):
points:=1000:
num:=8:
phi:=(45+5.0*ran)*Pi/180:
constants:=array([evalf(2*(sqrt((tan(phi)^2+1)/(tan(phi)^2-1))))
$ran=1..num]):
psi:=array([(n)$n=1..points]):
psi:=map((x)->x/points,psi):
jj:=1:
for jj to num do
C:=constants[jj];
slope:=sqrt((C^2+4)/2);
sol[jj]:=dsolve(des[1]=diff(tau(theta),theta),tau(0)=psi[1],D(t)(0)
= slope,tau(theta),type=numeric, method = rkf45,value=psi):
od:
jj:=1:
for jj to num do
B[jj]:=array(1..2*points);
for ii to points do
theta:=sol[jj][2,1][ii,1]:
tau(theta):=sol[jj][2,1][ii,2]:
B[jj][2*ii-1]:=evalf(x):
B[jj][2*ii]:=evalf(l):
od:
od:
theta:='theta':tau(theta):='tau(theta)':C:='C':
x:=2*sin(theta)^2-sqrt(4*sin(theta)^4+tau(theta)^2-4*sin(theta)^2):
dxdn:=diff(x,theta):
```

```
l:=tau(theta):
dldn:=diff(l,theta):
dcdn2:=dldn^2+dxdn^2-C^2:
des:=solve(dcdn2,diff(tau(theta),theta)):
points:=1000:
num:=8:
phi:=(45+5.0*ran)*Pi/180:
constants:=array([evalf(2*(sqrt((tan(phi)^2+1)/(tan(phi)^2-1))))
$ran=1..num]):
psi:=array([(n)$n=1..points])
psi:=map((x)->x/points,psi):
jj:=1:
for jj to num do
C:=constants[jj];
slope:=sqrt((C^2+4)/2);
sol[jj]:=dsolve(des[1]=diff(tau(theta),theta),tau(0)=psi[1],D(t)(0)
= slope,tau(theta),type=numeric, method = rkf45,value=psi):
od:
jj:=1:
for jj to num do
A[jj]:=array(1..2*points);
for ii to points do
theta:=sol[jj][2,1][ii,1]:
tau(theta):=sol[jj][2,1][ii,2]:
A[jj][2*ii-1]:=evalf(x):
A[jj][2*ii]:=evalf(l):
od:
od:
plot({A[m]$m=1..8,B[m]$m=1..8,Hyper},time=-1..1,offset=0..2,
color=BLACK,numpoints=1000);
```

Because of the nature of the $[l, \chi, \theta]$ surface at the origin the Runge-Kutta process is unstable precisely at that point. It is therefore necessary to start the numerical integration a short distance from the origin. If results very close to the origin are required it is best to use the series solution. The Runge-Kutta solution is satisfactory when the solution is

started at a point some distance from the origin. A satisfactory nearly complete solution may be obtained by using the series solution method close to the origin and changing to the numerical method at a suitable point probably beyond the first reflection from the sea floor. The result of a Runge-Kutta numerical solution would be a tabulation of values of l and χ for different values of C, θ and K. If analytical values were required, interpolation could be achieved through, for example, fitting splines to the tabulation. Conversion to the un-normalised space follows the methods described in considering the application of the series solutions.

6. TIME BASIS RADIAL TRACES

It is mathematically simpler, and may be theoretically preferable, to construct 'radial' traces on the basis of the times of arrival of multiple reflections from the sea floor. If this method is preferred the concept is that at a particular value of offset x the time taken to receive the primary reflection is t_1. The 'radial' trace can be drawn such that the time to the first multiple is twice the time for the primary reflection i.e. $t_2 = 2\,t_1$. We need to find the values of offset at which that relationship holds in general as $t_n = n\,t_1$.

In the shot record this can be found from equation 1 by substituting $t_n = n\,t_1$ and solving for x. Transformation to the normalises coordinate system yields parametric equations for the 'time radials'. These are given below for the shot record

$$l = K\theta,$$
$$\chi = 2\sin(\theta)^2 \pm \sqrt{4\sin(\theta)^4 + K^2\theta^2 - 4\sin(\theta)^2}, \tag{31}$$

and for the CMP gather

$$l = K\theta,$$
$$\chi = \frac{\sqrt{K^2\theta^2 - \sin(\theta)^2}}{\cos(\theta)}. \tag{32}$$

Thes equations can be found directly from equations 5 and 6. Conversion of these equations to un-normalised space follows substitution by equations 3 and 4 and of $\theta = n\alpha$.

Time basis radials for the shot records and CMP gathers are plotted in Figures 13 and 14 and the Maple code which calculates and plots these is given below.

For the shot record:

```
restart:
eqn:=l^2=4*sin(theta)^2+x^2-4*x*sin(theta)^2:
```

A23

```
l:=K*theta:
xval[1]:=simplify(solve(eqn,x)[1],radical):
xval[2]:=simplify(solve(eqn,x)[2],radical):
dldt:=diff(l,theta):
dxdt:=diff(xval[1],theta):
dldx:=dldt/dxdt:
slope:=tan(psi)=limit(dldx,theta=0):
Konst:=solve(slope,K):
K:=Konst[1]:
psi:=(45+5.0*ran)*Pi/180:
Plotp:=[xval[1],K*theta,theta=0..Pi/2]$ran=1..8:
Plotn:=[xval[2],K*theta,theta=0..Pi/2]$ran=1..8:
plot({Plotp,Plotn},offset=-1..1,time=0..2,color=BLACK,
numpoints=1001);
```

and for the CMP gather

```
restart:
eqn:=l^2=sin(theta)^2+x^2*cos(theta)^2:
l:=K*theta:
xval:=solve(eqn,x):
dldt:=diff(l,theta):
dxdt:=diff(xval[2],theta):
dldx:=dldt/dxdt:
slope:=tan(psi)=limit(dldx,theta=0):
Konst:=solve(slope,K):
K:=Konst[2]:
psi:=(45+5.0*ran)*Pi/180:
Plotg:=[xval[2],K*theta,theta=0..Pi/2]$ran=1..8:
plot({Plotg},offset=0..1,time=0..1,color=BLACK,numpoints=1001);
```

7. INCIDENCE AND TAKE-OFF ANGLES

Instrumental effects due to non-isotropic detection in geophones or non-isotropic source characteristics can influence the shape of the detected waveform. Some of the instrumental variables can be eliminated if the incidence angle of the signal at a detector or the take-off angle from a source can be kept constant. It is useful therefore, in investigating multiples,

to define traces along lines of equal angle, either of arrival at the detector or take-off from the source.

It can be shown that the equations of the curves for equal angles of take-off from the source are identical to the isostretch curves derived above and given in equation 12. Constuction of isostretch curves will therefore automatically follow curves of equal take-off angle.

The equations for equal angle of incidence at the detector are given below.

Before MMO is applied

$$\frac{b - \sqrt{b^2 - x^2 + 2\,x}}{x - 2} = \frac{\sqrt{1 + b^2} + \sqrt{b^2 + 1 - l^2}}{l} \tag{33}$$

and after MMO is applied

$$\theta = \arccos\left(\sqrt{-\frac{x^2 - 4\,x + 4}{2\,x - 4 - 2\,b^2 + 2\,b\sqrt{b^2 - x^2 + 2\,x}}}\right) \tag{34}$$

Maple code which can be used to derive and plot the curves of equal angle is included below.

```
# For equal incidence angle at the detector
restart:
eqn1:=L^2=4*r^2*sin(n*alpha)^2/sin(alpha)^2+X^2-
4*r*X*sin(n*alpha)^2/sin(alpha):
eqn1n:=l^2=4*sin(theta)^2+x^2-4*x*sin(theta)^2:
xsol:=solve(eqn1n,x):
AP[1]:=d*tan(phi+alpha):AP[2]:=RP[2]*tan(phi+alpha):
RP[2]:=d-X*sin(alpha):
PP[12]:=AP[1]+AP[2]:
X*cos(alpha)=PP[12]:
Xval:=simplify(solve(",X)):
Xval:=subs(d=r*sin(n*alpha)/sin(alpha),alpha=n*alpha,Xval):
alpha:=Pi/150:
n:='n':phi:=Pi*j/15:r:=1:
eqn1a:=subs(X=Xval,eqn1):
evalf(sqrt(rhs(eqn1a))):
xrange:=1/sin(alpha):yrange:=2*xrange:
```

```
plot([Xval,sqrt(rhs(eqn1a)),n=0..40]$j=1..15,
x=-xrange..xrange,l=0..yrange,color=BLACK,
scaling=CONSTRAINED,thickness=1);
alpha:='alpha':phi:='phi':
xval:=Xval*sin(alpha)/r:
xval:=subs(n*alpha=theta,xval):
xval:=subs(cos(theta)*cos(phi-theta)+sin(phi-theta)*sin(theta)
=cos(2*theta-phi),"):
combine(xval,trig):
eqn1na:=subs(x=xval,eqn1n):
lval:=sqrt(rhs(eqn1na)):
phi:=Pi*j/15:
ReceivePlot:=[xval,lval,theta=0..Pi/2]$j=1..15:
plot([xval,lval,theta=0..Pi/2]$j=1..15,x=-1..1,l=0..2,
color=BLACK,thickness=1,scaling=CONSTRAINED,numpoints=1001);
# For equal take-off angles from the source
restart:
eqn1:=L^2=4*r^2*sin(n*alpha)^2/sin(alpha)^2+X^2-
4*r*X*sin(n*alpha)^2/sin(alpha):
eqn1n:=l^2=4*sin(theta)^2+x^2-4*x*sin(theta)^2:
xsol:=solve(eqn1n,x):
AP[1]:=d*tan(phi-alpha):AP[2]:=RP[2]*tan(phi-alpha):
RP[2]:=d-X*sin(alpha):
PP[12]:=AP[1]+AP[2]:
X*cos(alpha)=PP[12]:
Xval:=simplify(solve(",X)):
Xval:=subs(d=r*sin(n*alpha)/sin(alpha),alpha=n*alpha,Xval):
alpha:=Pi/150:
n:='n':phi:=Pi*j/15:r:=1:
eqn1a:=subs(X=Xval,eqn1):
evalf(sqrt(rhs(eqn1a))):
xrange:=1/sin(alpha):yrange:=2*xrange:
plot([Xval,sqrt(rhs(eqn1a)),n=0..40]$j=1..15,
```

A26

```
x=-xrange..xrange,l=0..yrange,color=BLACK,
scaling=CONSTRAINED,thickness=1);
alpha:='alpha':phi:='phi':
xval:=Xval*sin(alpha)/r:
xval:=subs(n*alpha=theta,xval):
xval:=subs(cos(theta)*cos(phi-theta)+sin(phi-theta)*sin(theta)
=cos(2*theta-phi),"):
combine(xval,trig):
eqn1na:=subs(x=xval,eqn1n):
lval:=sqrt(rhs(eqn1na)):
phi:=Pi*j/15:
ReceivePlot:=[xval,lval,theta=0..Pi/2]$j=1..15:
plot([xval,lval,theta=0..Pi/2]$j=1..15,x=-1..1,l=0..2,
color=BLACK,thickness=1,scaling=CONSTRAINED,numpoints=1001);
# This shows that the isostretch curves are the same as the
curves of constant take-off angle from the source
C:='C':phi:='phi':
expand(xval^2):
subs(sin(phi)=1/(K^2+1)^(1/2),cos(phi)=K/(K^2+1)^(1/2),"):
xeqn:=x^2=simplify(");
```

The curves of equal incident angle are shown in figure 15 drawn before MMO is applied. It is noted that these curves are ellipses and are symmetric about the line $l = \chi - 1$. The curves for equal take-off angle from the source are not shown as they are identical to the isostretch curves for the shot record. This fact may be useful in analysing shot records for multiples as the source term will be constant along the lines of equal stretch and so any anisotropy of the source will be constant along those curves and assist with autocorrelation and auto deconvolution.

Figure 16 show curves of constant angle of incidence at the detector on a space transformed using the MMO equations for shot records (equation 7).

8. CONCLUSION

A number of interesting mathematical relationships have been derived for seismic multiple surface reflections. The usefulness of some of the mathematical relationships needs to be tested on real data from field surveys. The work has also shown the usefulness

of the symbolic mathematics package Maple in looking at some of the relationships and rendering them into simple form.

9. ACKNOWLEDGMENTS

References

[1] M Born and E Wolf. *Principles of Optics*. Pergamon Press, New York, 1964.

[2] D R De Pledge and N. F. Uren. Multiple suppression by event prediction and subtraction. In *Society of Exploration Geophysicists, 62nd Annual International Meeting and Exposition, New Orleans*, pages 1089–1092, 1992.

[3] S P Downie, B M Hartley, and N F Uren. Interactive attenuation of seismic multiples in the radial domain. *Exploration Geophysics.*, 26:486–492, 1995.

[4] Bruce M Hartley. The construction of radial traces in common mid point representation of seismic data with multiple surface reflections and a sloping sea floor. *Submitted for Publication in Geophysical Prospecting*, 1996.

[5] M G Lamont and N F Uren. Multiple moveout. Technical Report SPS 609/1993/EG 30, Curtin University of Technology, School of Physical Sciences, Department of Exploration Geophysics, 1993.

[6] M G Lamont and N F Uren. A method for the removal of long period surface related multiples. *Exploration Geophysics*, 26:477–481, 1995.

[7] F. K. Levin. Apparent velocity from dipping interface reflections. *Geophysics*, 36(3):510–516, 1971.

[8] M. T. Taner. Long period sea-floor multiples and their suppression. *Geophysical Prospecting*, 28:30–48, 1980.

Figure 1. Shot Record Hyperbolae
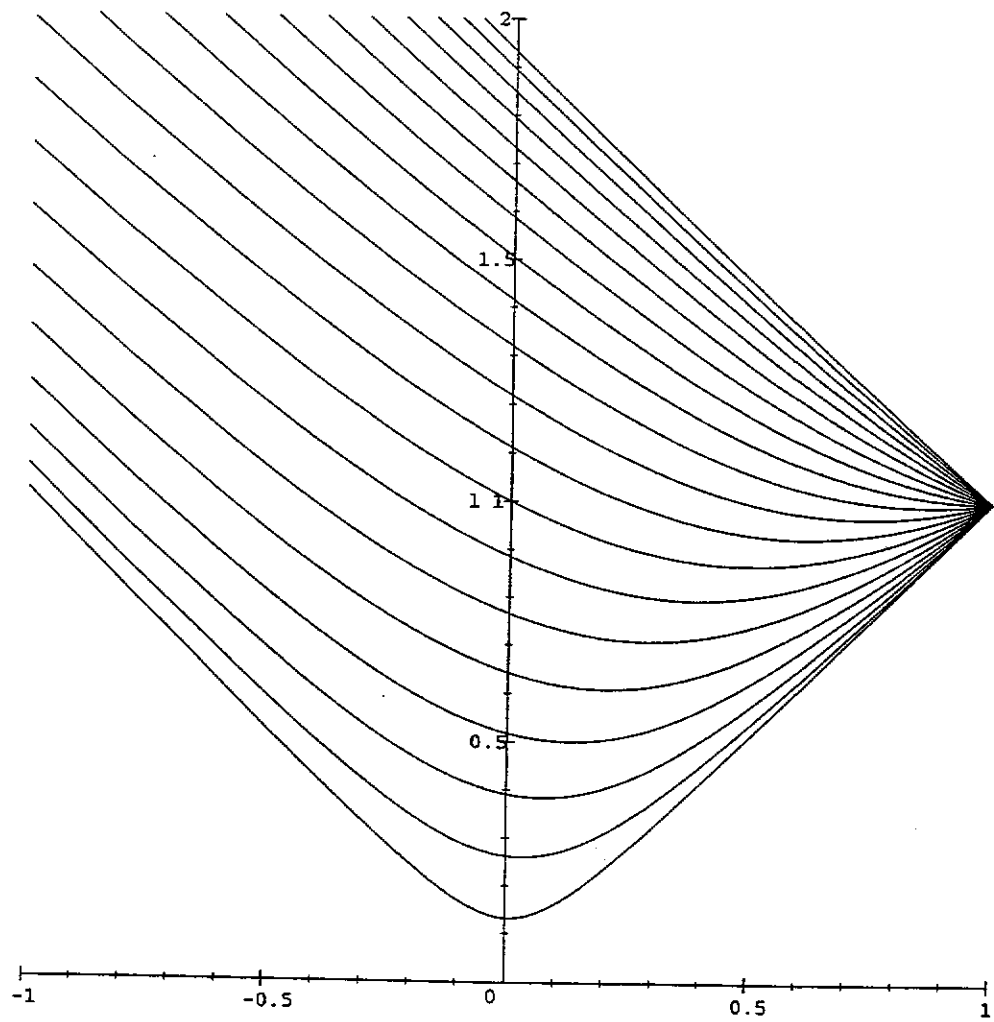
Figure 2. CMP Hyperbolae
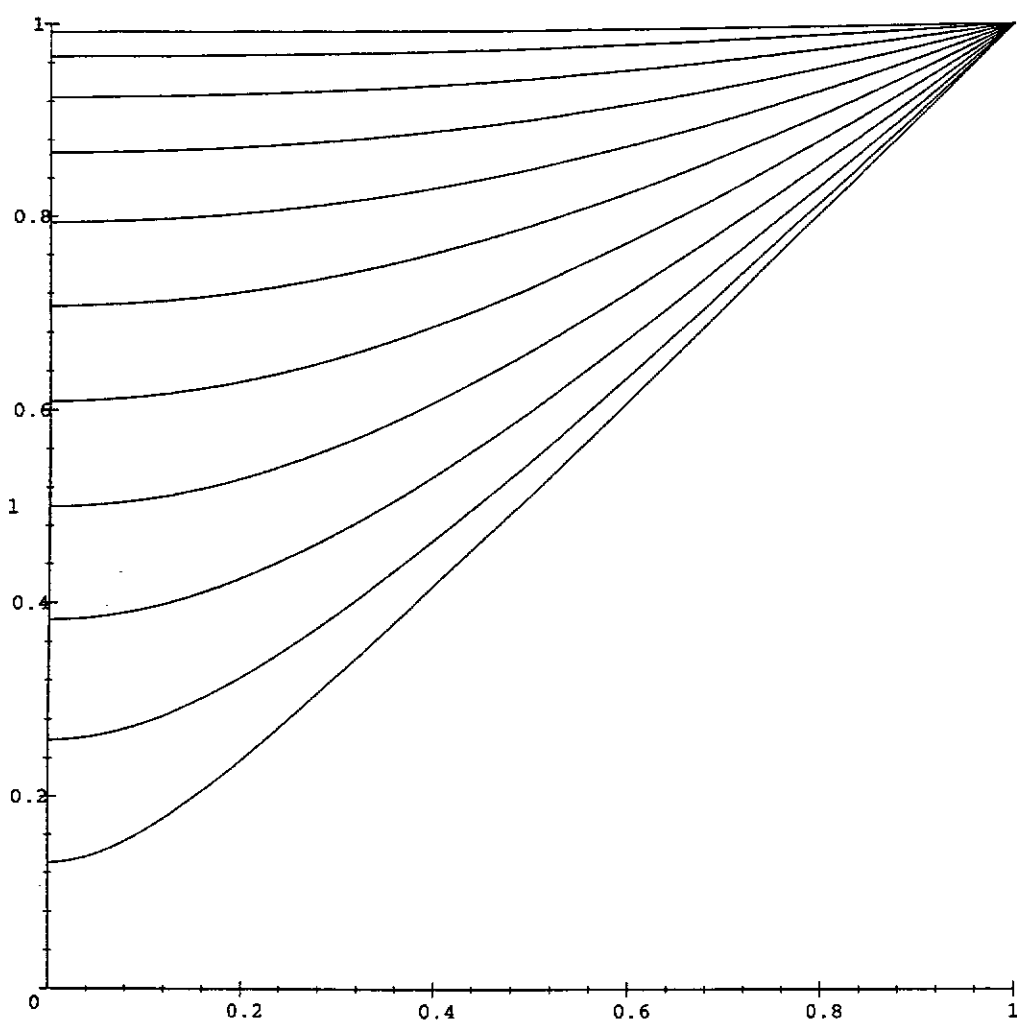
Figure 3. Isostretch Curves on Shot Record Hyperbolae
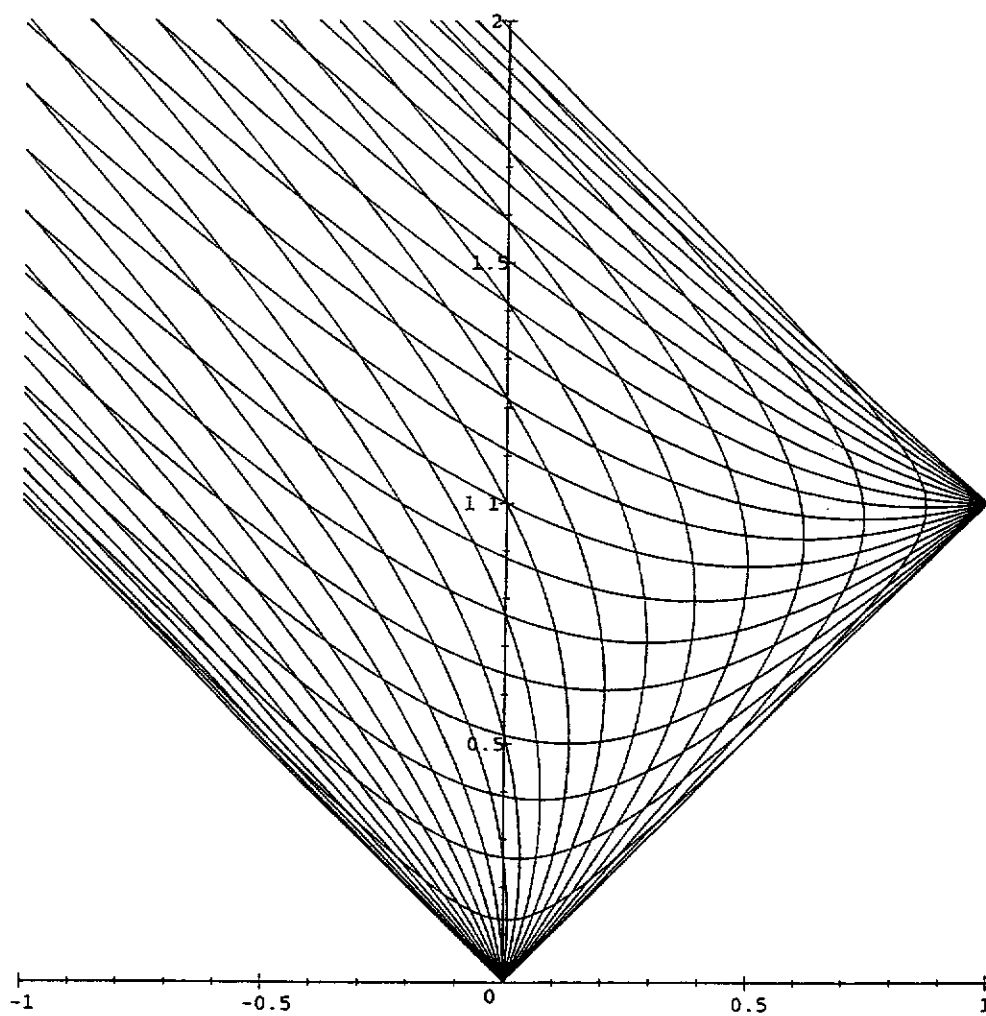
Figure 4. Shot Record Isostretch Curves After MMO
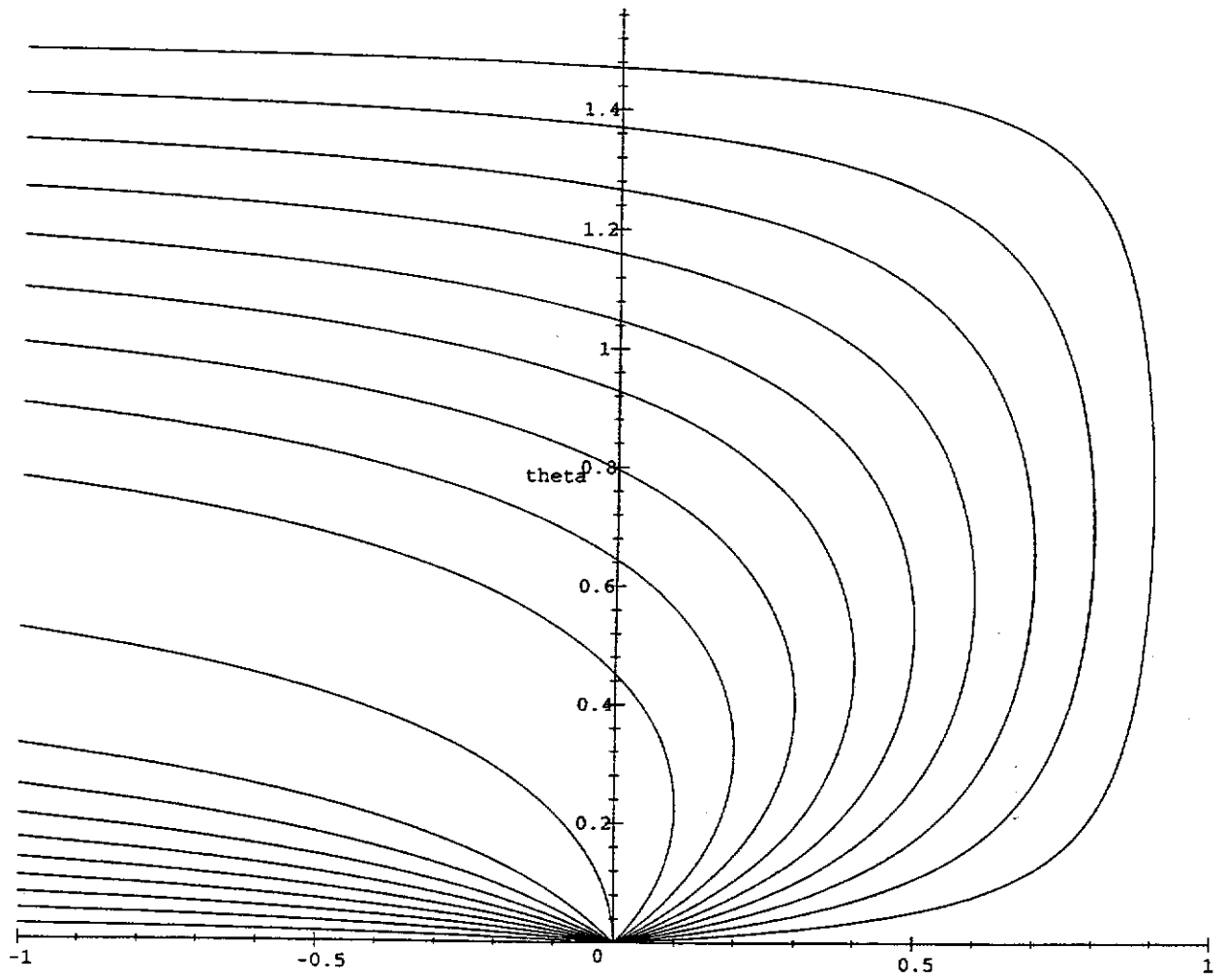
Figure 5. Isostretch Curves on CMP Hyperbolae
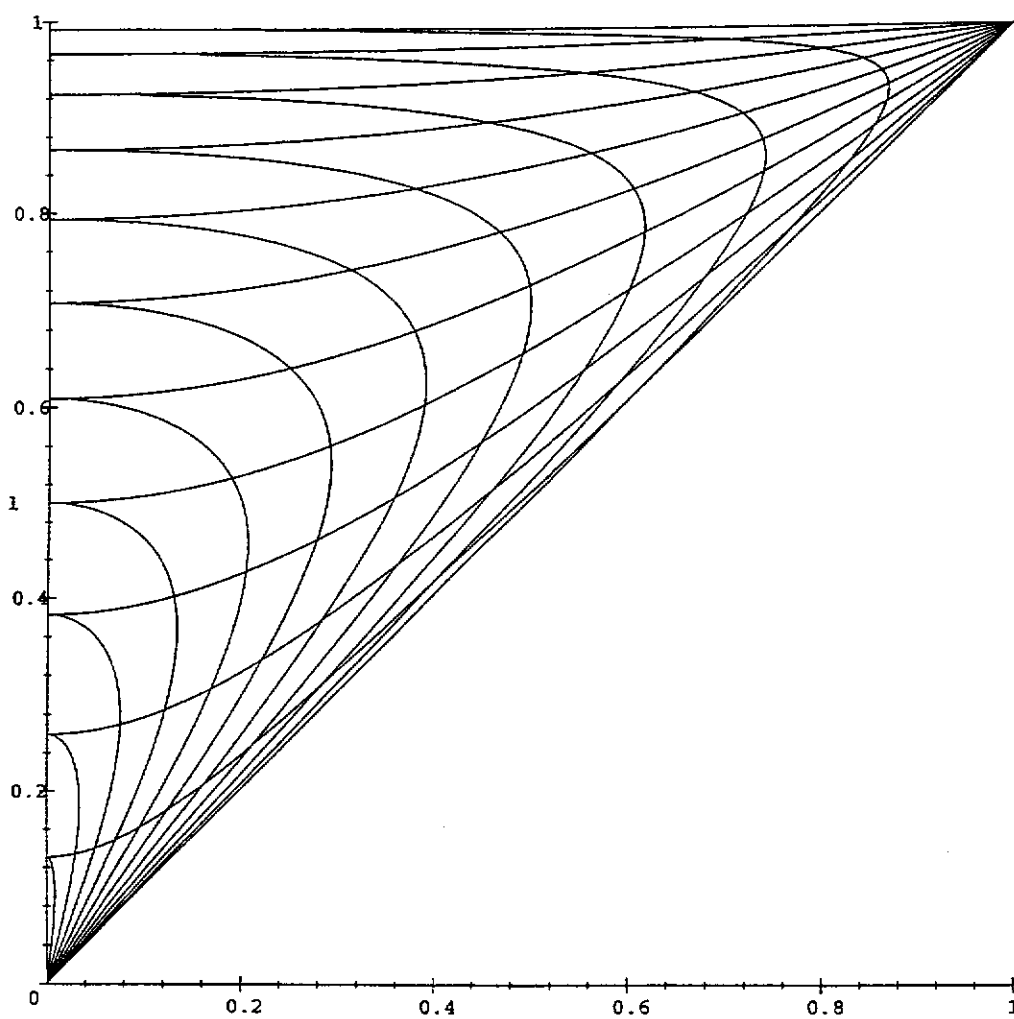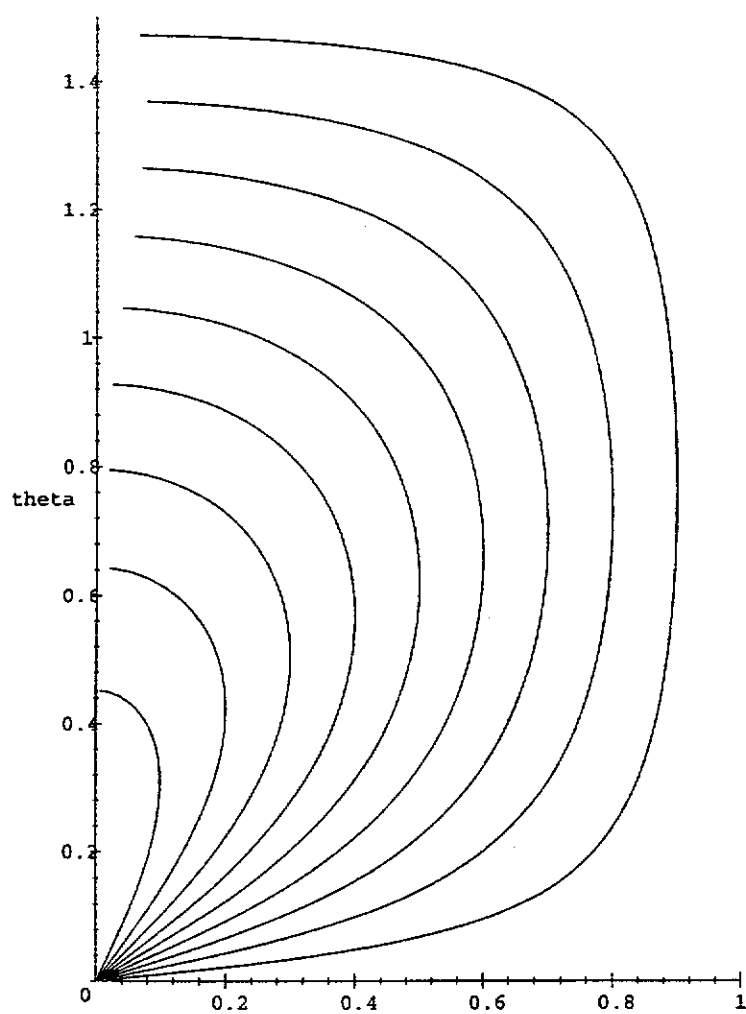
Figure 6. CMP Isostretch Curves After MMO
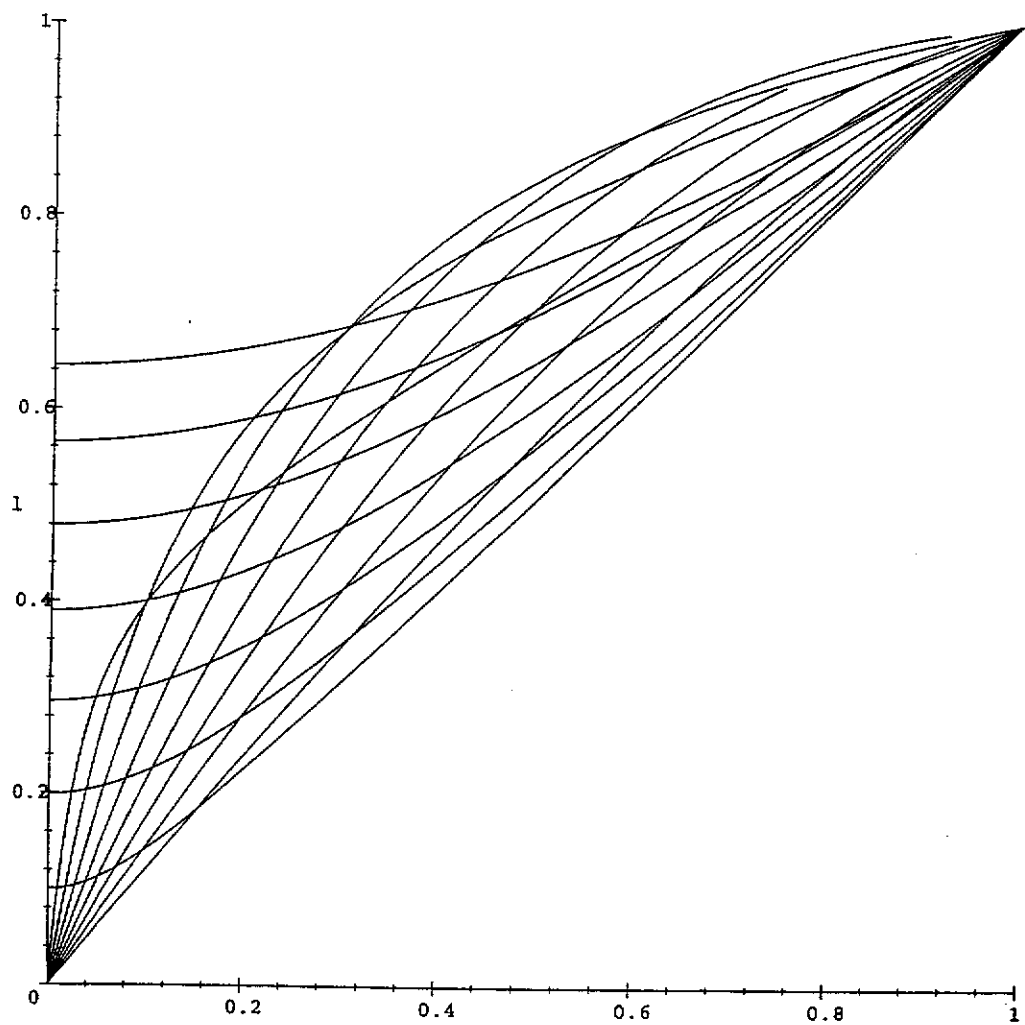
Figure 7. Radial Traces on CMP Hyperbolae

Figure 8. Percentage Error in CMP Radial Traces

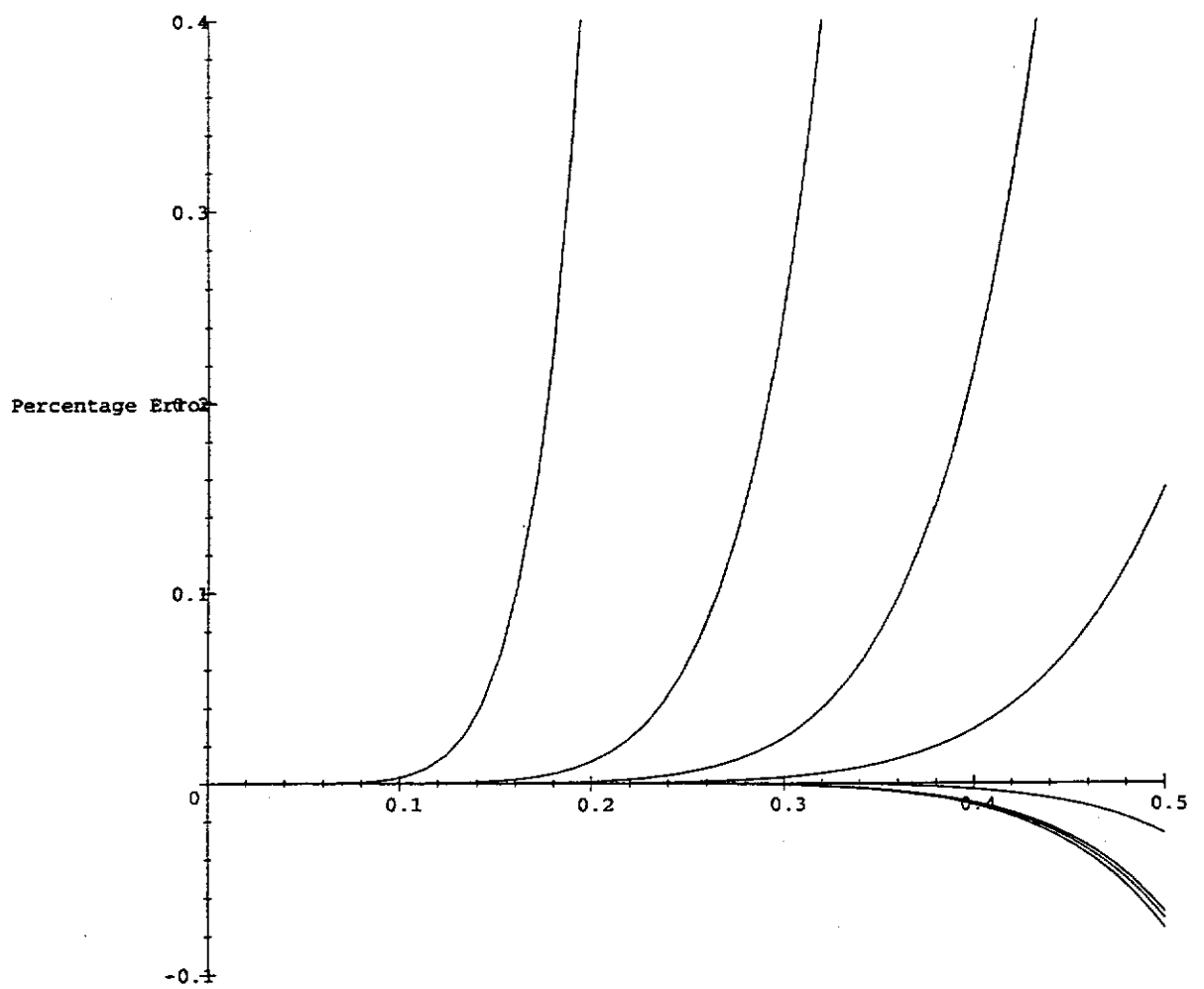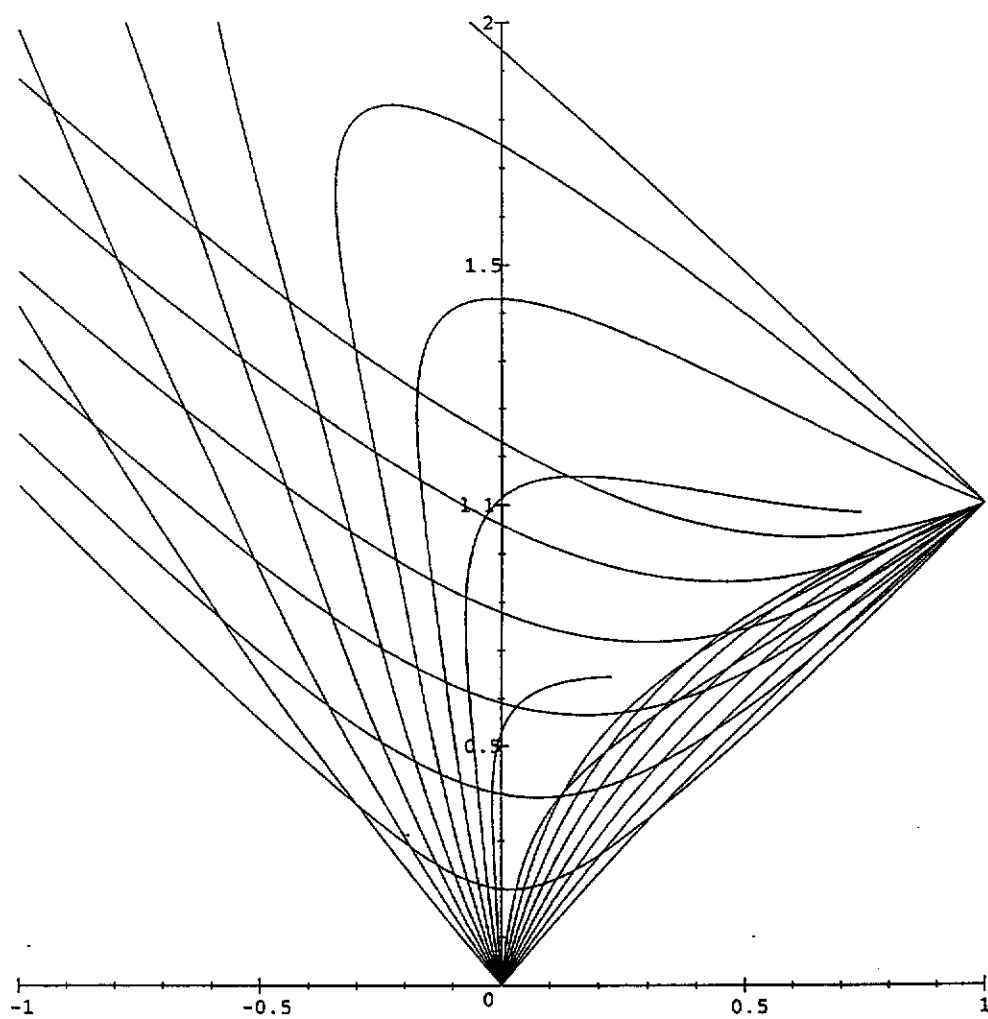Figure 9. Radial Traces on Shot Record Hyperbolae
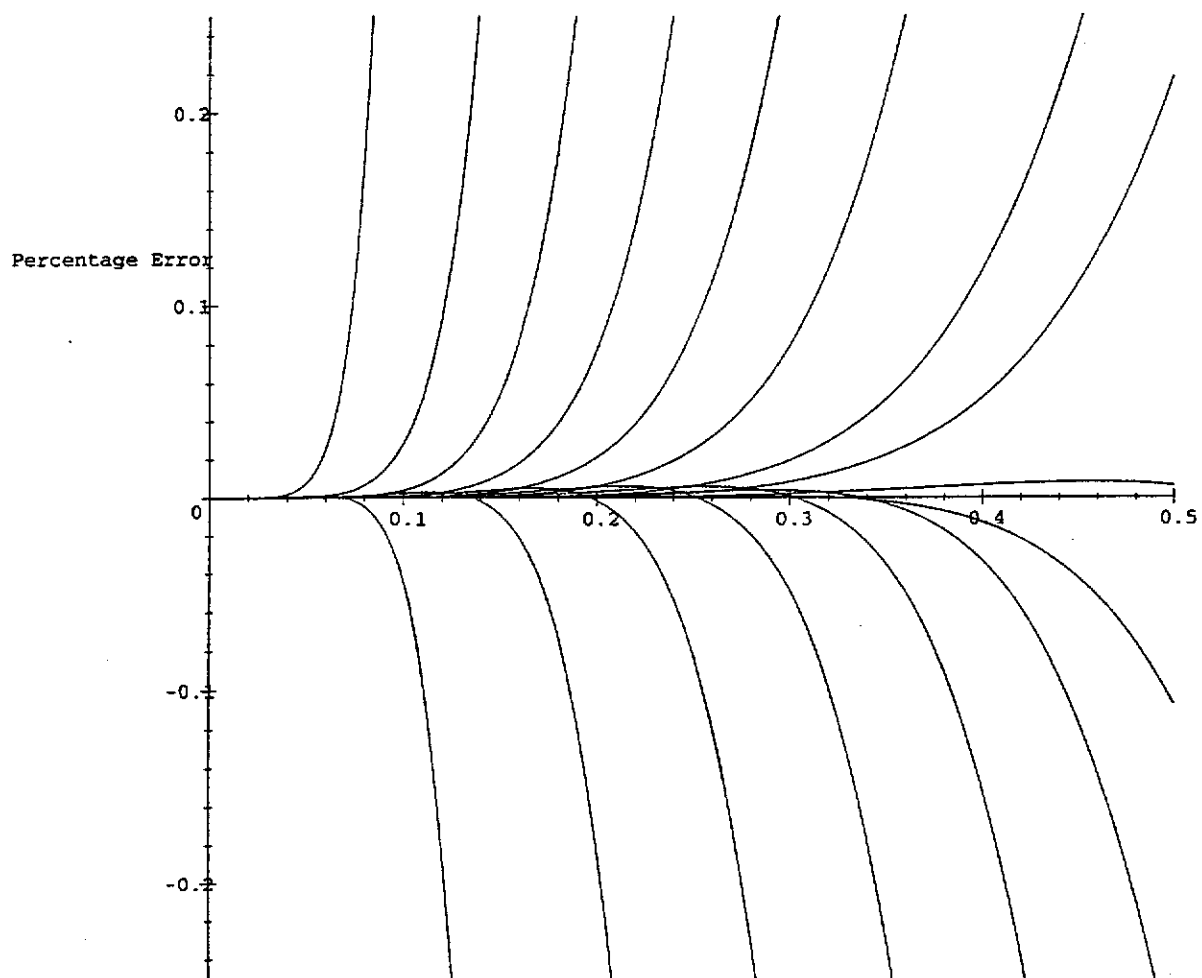
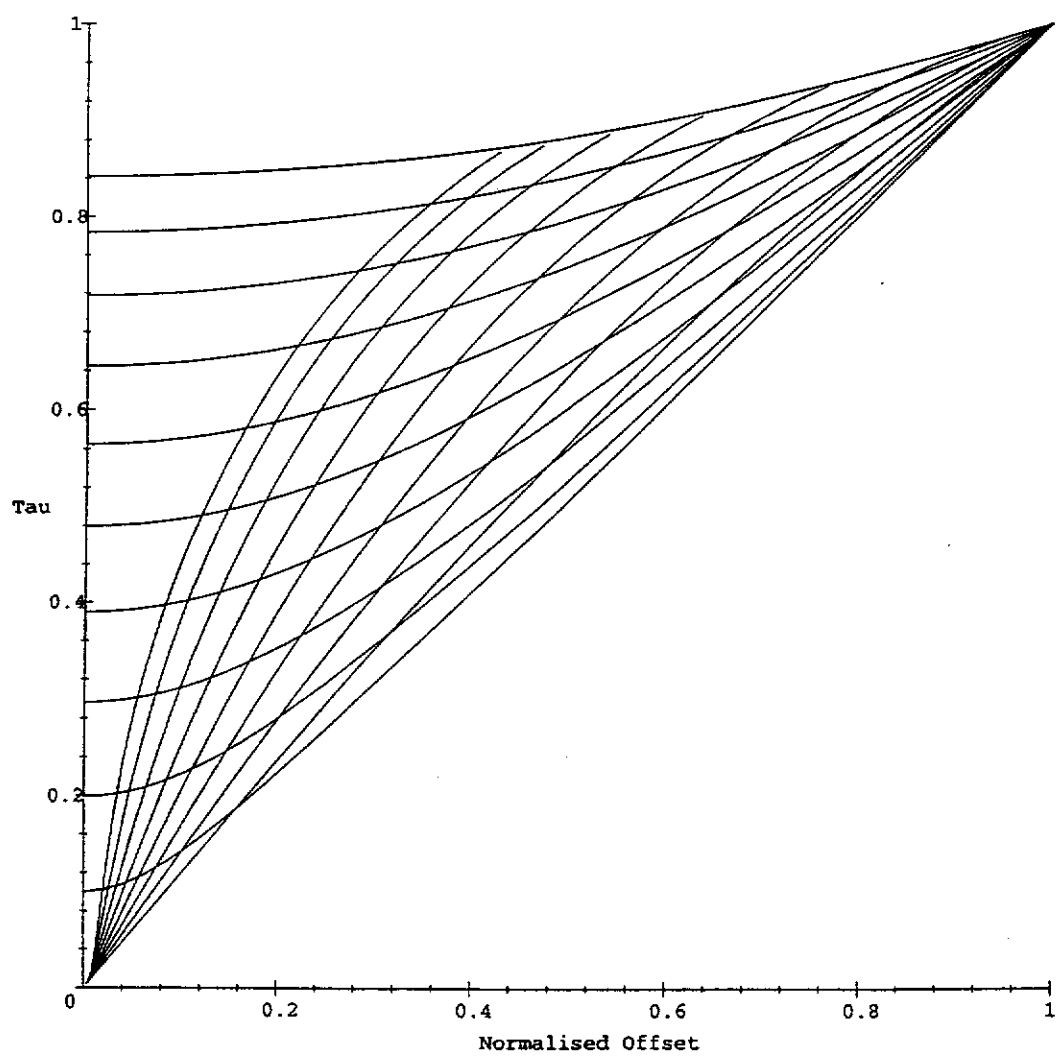Figure 10. Percentage Error in Shot Radials

Figure 11. Runge-Kutta Radials on CMP Hyperbolae

Figure 12. Runge-Kutta Radials on Shot Hyperbolae
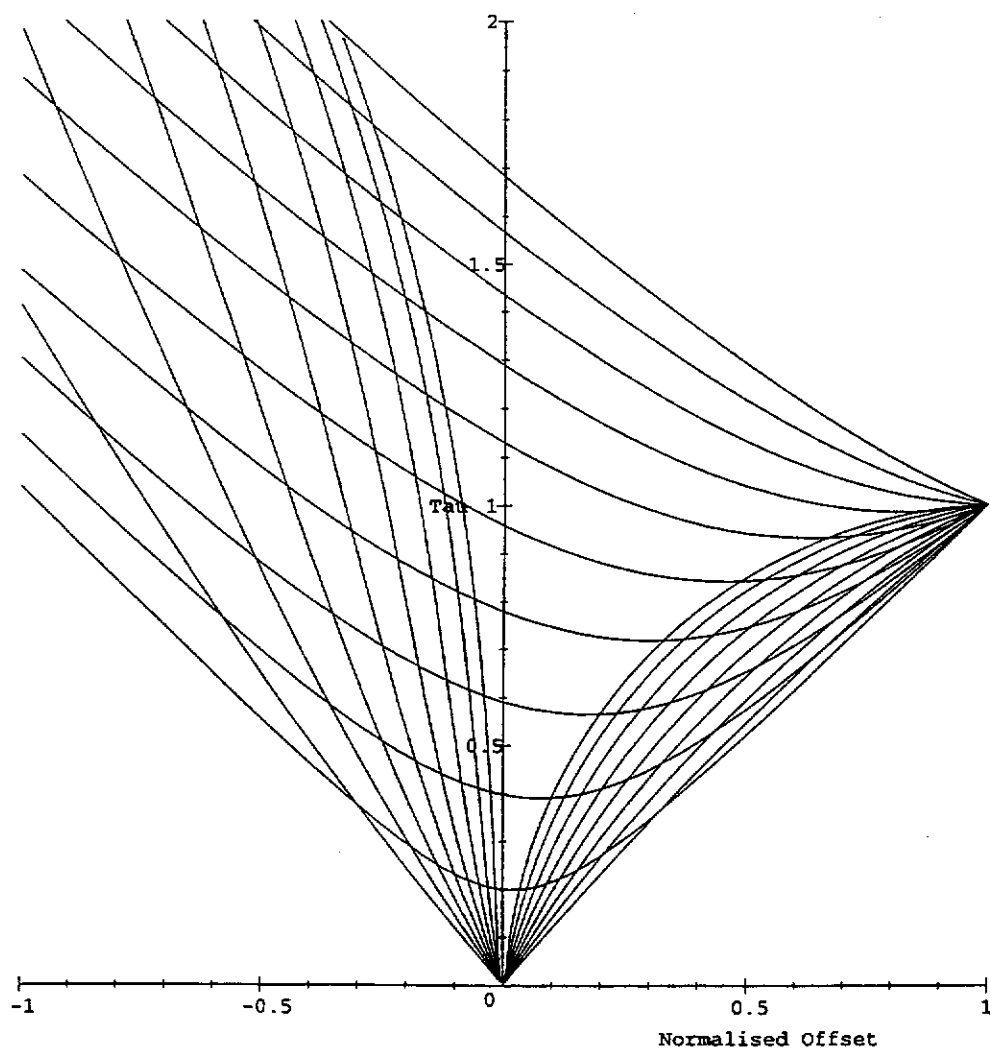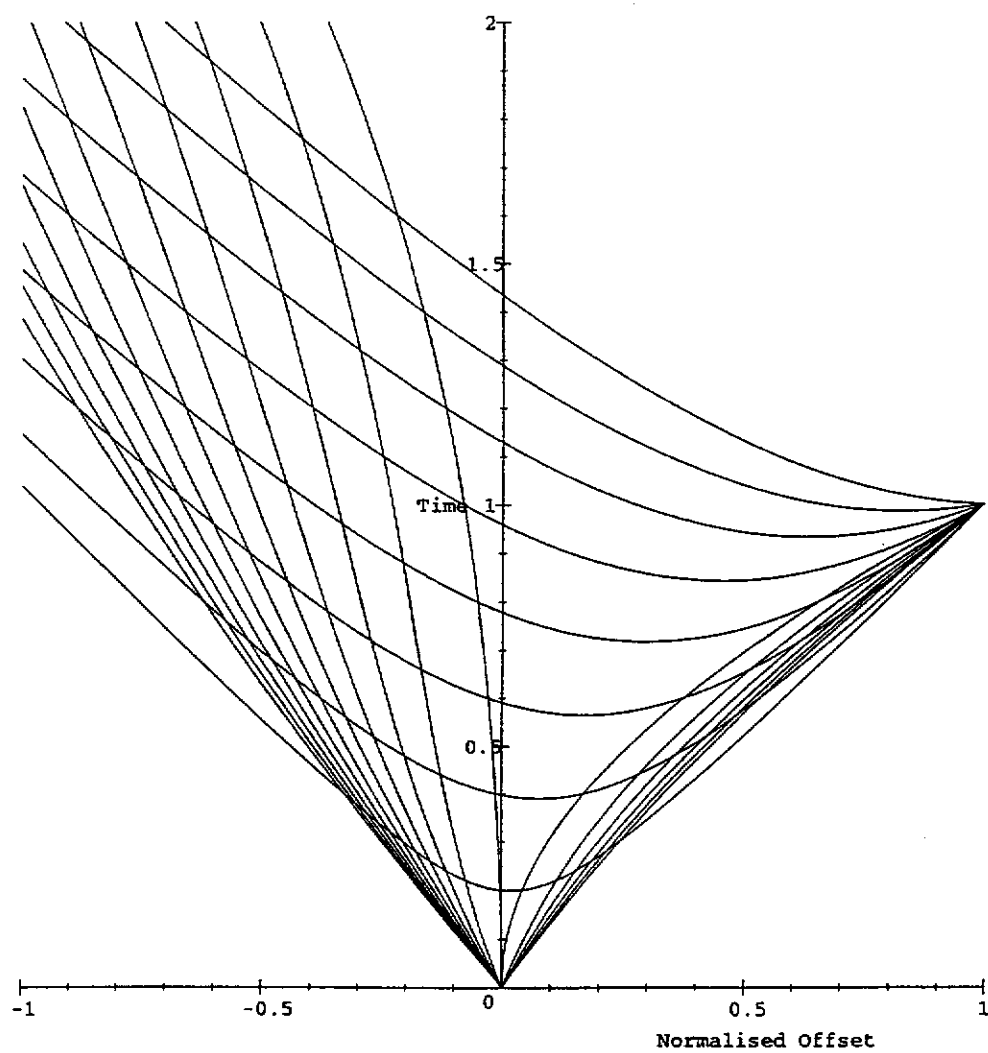
Figure13. Time Radials on Shot Hyperbolae

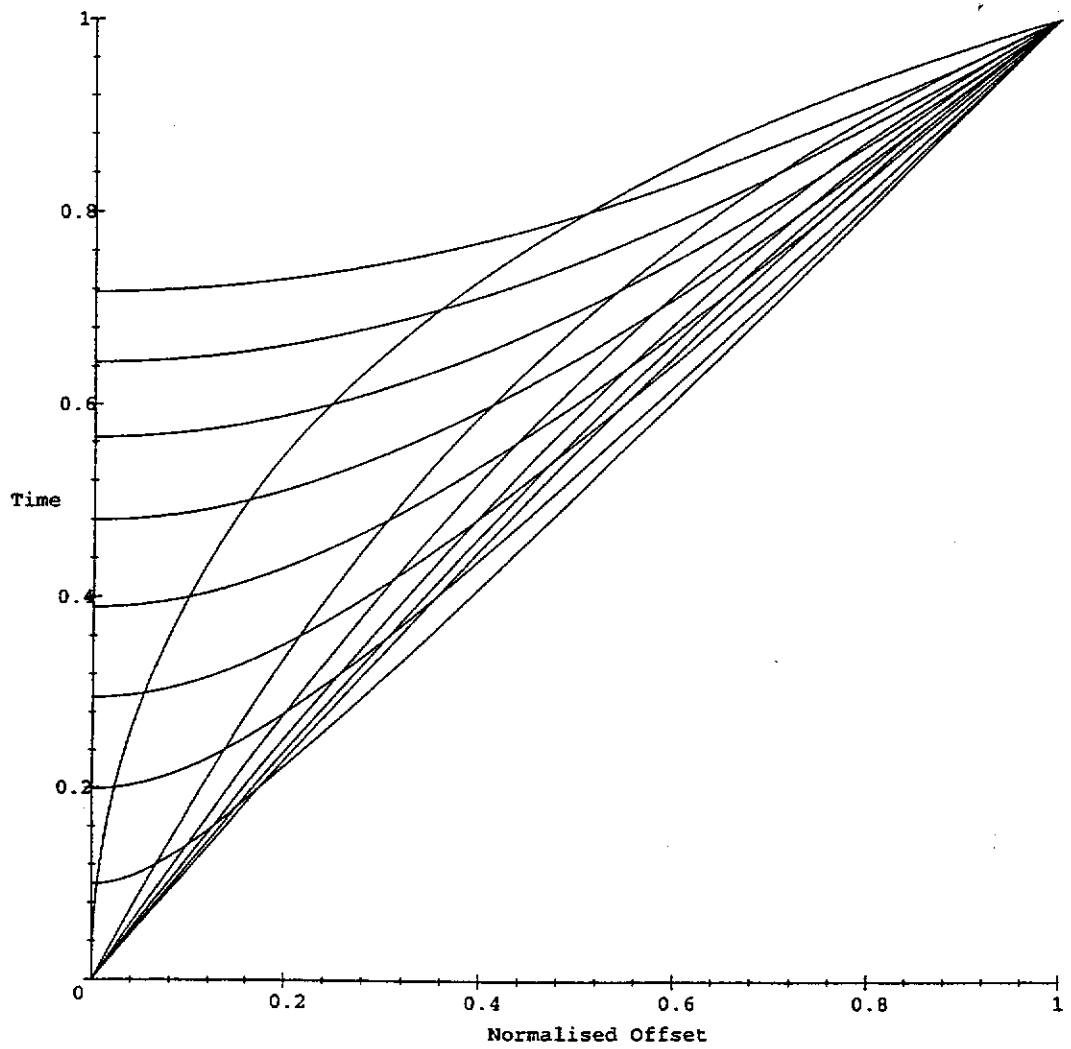Figure14. Time Radials on CMP Hyperbolae
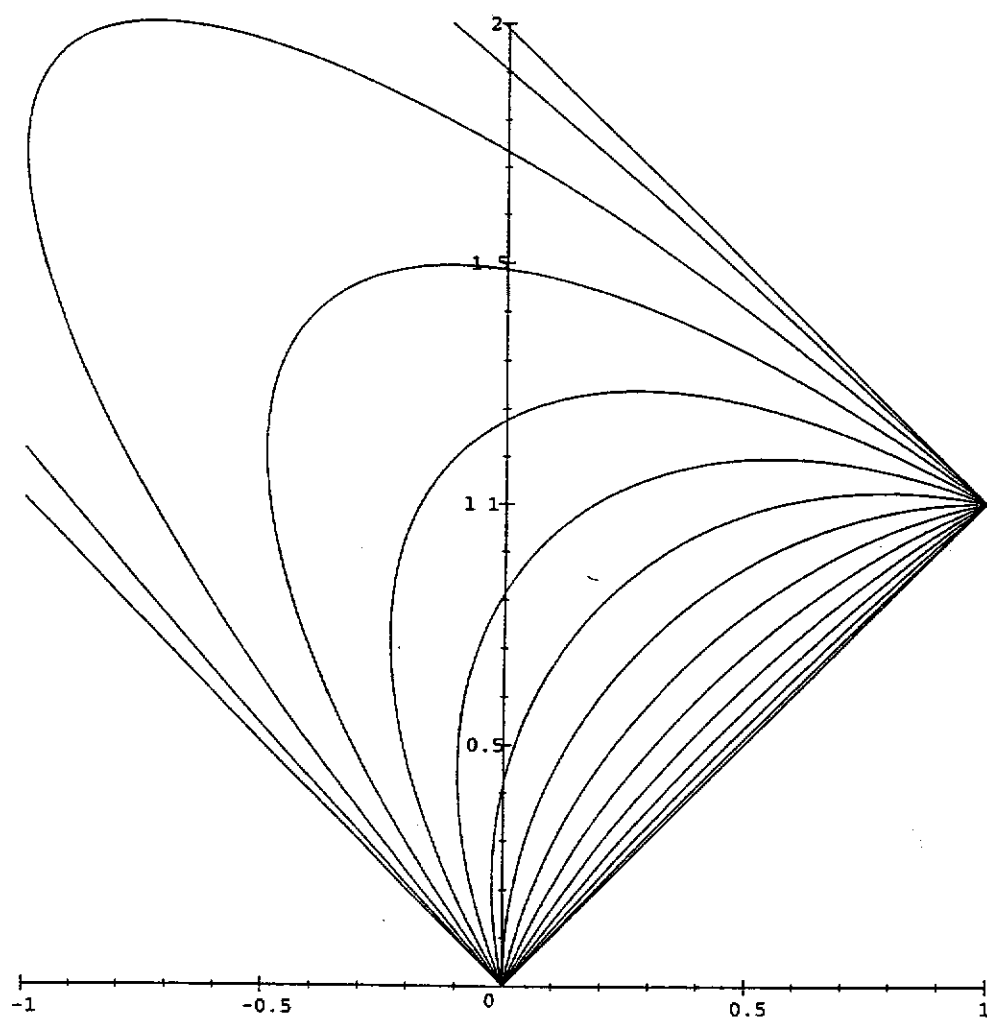

Time

Normalised Offset

Figure 15 Curves of Equal Arrival Angle at a Receiver

Figure 16 Isoangle Curves Following MMO